

Challenges and breakthroughs in alpha radiation detection, with a focus on the innovative RemoteAlpha project

I.R. Nikolényi , Z. Gémesi

(1) Institute of Mathematics and Basic Science, (2) Research teacher, MATE
Hungarian University of Agriculture and Life Sciences
Páter K. u. 1., Gödöllő, H-2100 Hungary
E-mail: Nikolenyi.Istvan.Robert@uni-mate.hu

**Experimental Learning Day for
Students on Radiology**

**November 27, 2023, Gödöllő,
Hungary**



HUNGARIAN UNIVERSITY OF
AGRICULTURE AND LIFE SCIENCES

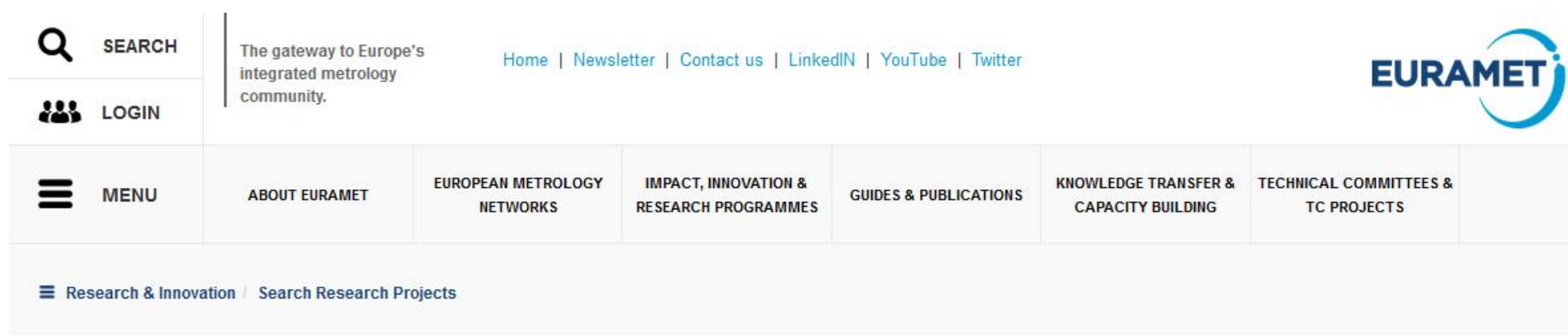
- **Horizon, EMPIR 2020 19ENV02 RemoteAlpha project, partners**
- **Need for novel-type detection system**
- **Objectives**
- **Alpha-radioluminescence phenomenon**
- **MATE's participation in project**
- **Educational benefits**
- **Conclusions**

Informations about Horizon, EMPIR 2020 19ENV02 RemoteAlpha project. Partners

<https://www.euramet.org/researchinnovation/search-research-projects/details/project/remote-and-real-timeoptical-detection-of-alpha-emitting-radionuclides-in-the-environment/>

<https://remotealpha.drmr.nipne.ro/partners.php>

Remote and real-time optical detection of alpha-emitting radionuclides in the environment

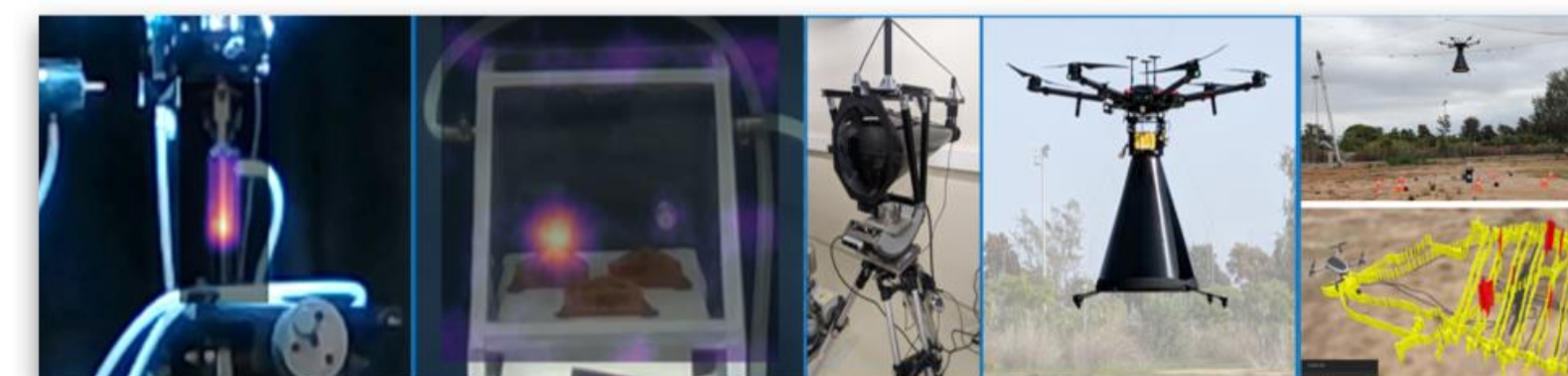


SEARCH LOGIN MENU

Home | Newsletter | Contact us | LinkedIn | YouTube | Twitter

ABOUT EURAMET EUROPEAN METROLOGY NETWORKS IMPACT, INNOVATION & RESEARCH PROGRAMMES GUIDES & PUBLICATIONS KNOWLEDGE TRANSFER & CAPACITY BUILDING TECHNICAL COMMITTEES & TC PROJECTS

Research & Innovation Search Research Projects



Home Project Information Members Area Blog Contact GDPR

Remote and real-time optical detection of alpha-emitting radionuclides in the environment

Short Name: RemoteALPHA, Project Number: 19ENV02



Man in protective workwear

COORDINATOR
Faton Krasniqi (PTB)

PARTICIPATING EURAMET NMIS AND DIS

BFKH (Hungary)

IFIN-HH (Romania)

PTB (Germany)

OTHER PARTICIPANTS

Alfa Rift Oy (Finland)
Gottfried Wilhelm Leibniz Universität Hannover (Germany)
Magyar Agrár- és Élettudományi Egyetem (Hungary)
Tampereen korkeakoulusäätiö sr (Finland)
Universitat Politècnica de Catalunya (Spain)

INFORMATION

PROGRAMME
EMPIR

FIELD
Environment

STATUS
in progress

CALL
2019

DURATION
2020-2023

OTHER PARTICIPANTS

Alfa Rift Oy (Finland)
Gottfried Wilhelm Leibniz Universität Hannover (Germany)
Magyar Agrár- és Élettudományi Egyetem (Hungary)
Tampereen korkeakoulusäätiö sr (Finland)
Universitat Politècnica de Catalunya (Spain)



Physikalisch-Technische Bundesanstalt



KORMÁNYHIVATALOK

Budapest Főváros Kormányhivatala



"Horia Hulubei" National Institute for R&D in Physics and Nuclear Engineering

Alfa Rift Oy

Alfa Rift Oy



Tampereen korkeakoulusäätiö sr



Gottfried Wilhelm Leibniz Universität Hannover



Universitat Politècnica de Catalunya



Szent István University



HUNGARIAN UNIVERSITY OF AGRICULTURE AND LIFE SCIENCES

This project 19ENV02 RemoteALPHA has received funding from the EMPIR programme co-financed by the Participating States and from the European Union's Horizon 2020 research and innovation programme.

Need for novel-type detection system for alpha emitters



- Attacks on nuclear power plants
- deployment of the dirty bomb (have a shocking effect on public opinion.)
- previous serious reactor accidents (Chernobyl, Fukushima)

„...Alpha particles represent the biggest risk to soft biological tissues compared to all nuclear decay products due to their high energy, large mass and high linear energy transfer. The amount of deposited energy is about 2 000 000 to 6 000 000 times higher than that of an ordinary chemical reaction (ordinary chemical energy used by the cells in the body), thus implying that a single alpha particle has the ability to severely damage or kill all cells within its range (typically, two to four cells). Therefore, the release of alpha emitting radionuclides in the environment, such as by nuclear terroristic attacks or transportation accidents, as well as by severe emergencies in nuclear installations, represents the greatest radiological threat for human beings if they enter the human body...”

„...Due to the short range of alpha particles, traditional detectors which require direct interaction with the alpha particles must be used in very close proximity to a contaminated surface, around 1 cm...”

„...A detection system to measure large-scale contamination of these radionuclides is currently not available...”

Crompton et al (2018), Sensors, 18, 1015; doi:10.3390/s18041015

(Publishable Summary for 19ENV02 RemoteAlpha)

The main objectives of the project: details and *results* of the project are in Publishable Summary

- „...New instrumentation for the optical detection of alpha particle emitters in the environment...” (Newsletter: October, 2023)
This is a passive method
- To develop and establish a calibration system for the novel-type radioluminescence detector systems.
- To extend the optical detection system to an imaging functionality for mapping of alpha contaminations in the environment using tripod and unmanned aerial vehicle (UAV)
- Feasibility study for an active, complementer method, namely laser-induced fluorescence (LIF) spectroscopic method for the detection of alpha emitters

https://www.euramet.org/research-innovation/search-research-projects/details?tx_eurametctp_project%5Bproject%5D=1687&cHash=c8e79ec377e929c4b2f6a6360dbc0968

•Publishable Summary [Publishable Summary Remote and real-time optical detection of alpha-emitting radionuclides in the environment \(19ENV02\), Call 2019](#) 0.22 MB

Alpha-radioluminescence phenomenon, its spectrum and measuring technique (Baschenko's results)

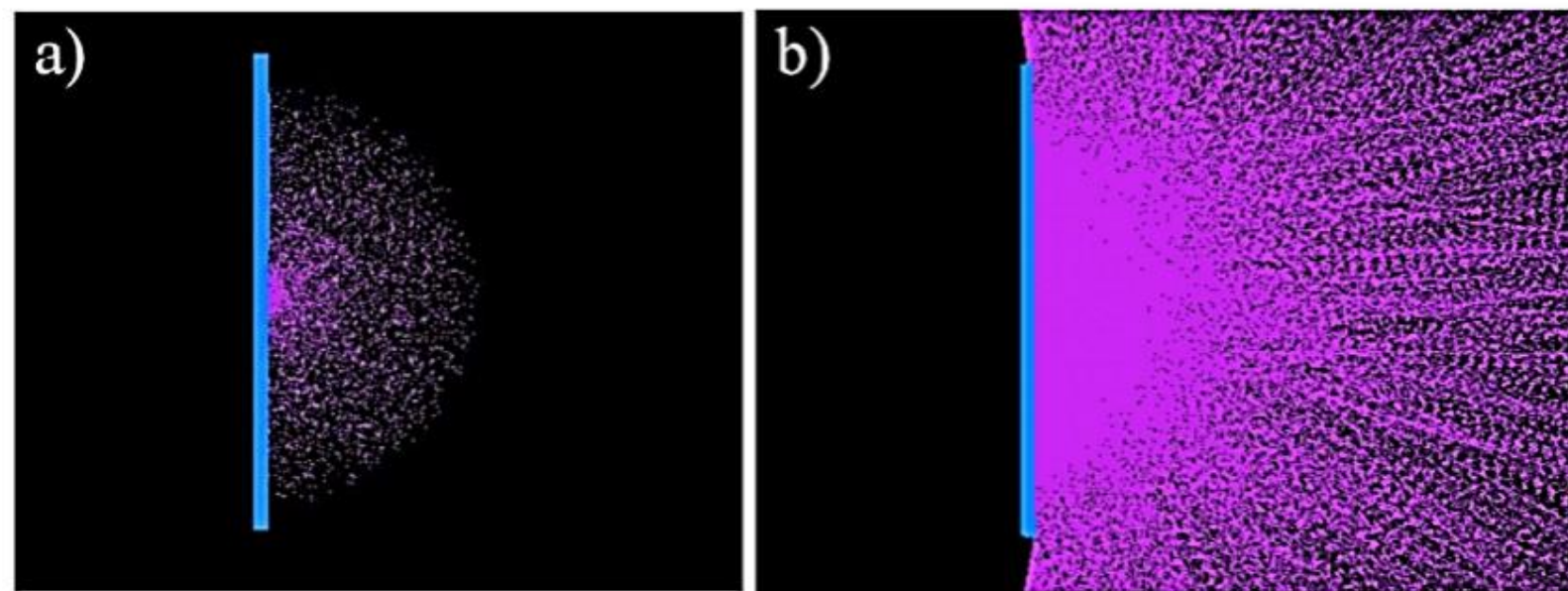


Figure 3. Model of: (a) Radioluminescence photons induced by alpha particles showing the hemisphere in which they are initially created by the alpha particles; (b) Showing the random directions in which the photons are emitted from the hemisphere in (a) and their longer path length—Using FRED Optical Engineering Software (Photon Engineering LLC) [11]. Reprinted with permission from the author.



Review

Alpha Particle Detection Using Alpha-Induced Air Radioluminescence: A Review and Future Prospects for Preliminary Radiological Characterisation for Nuclear Facilities Decommissioning

Anita J. Crompton^{1,*}, Kelum A. A. Gamage², Alex Jenkins³ and Charles James Taylor¹

Remote optical detection of alpha particle sources

77

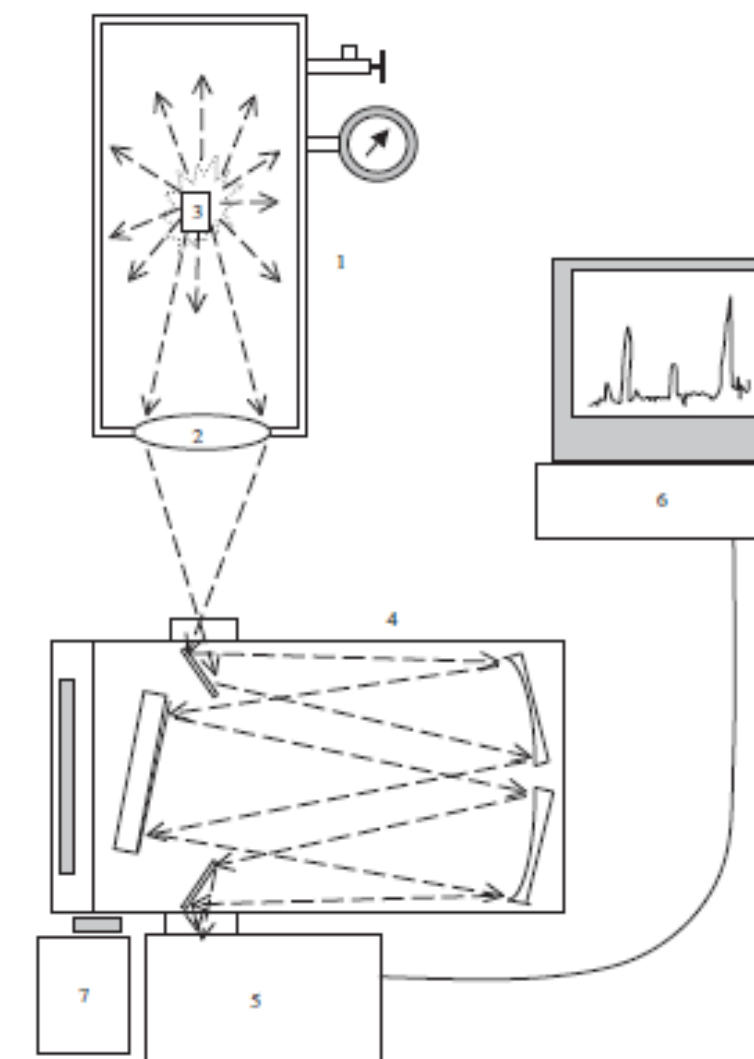


Figure 1. The scheme of the experimental set-up for the atmosphere alpha-radioluminescence phenomenon spectral investigation: 1—chamber diameter 400 × 1500 mm³; 2—window-lens diameter 200 mm, $F = 500$ mm; 3—alpha particle source; 4—monochromator; 5—photodetector; 6—PC; 7—stepping motor.

The main emitter is molecular nitrogen (and also nitrogen ion)

The air is a poor scintillator. Oxygen and water vapour quench the radioluminescence !!!

Remote optical detection of alpha particle sources

79

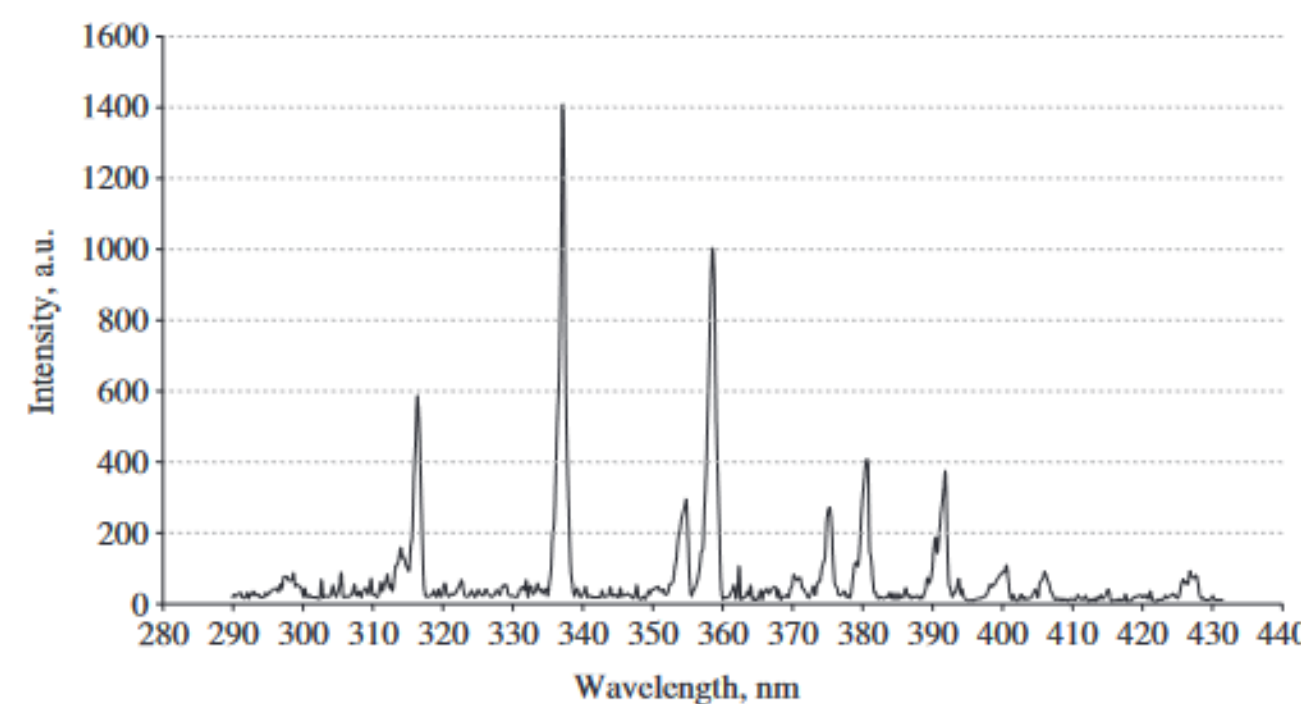
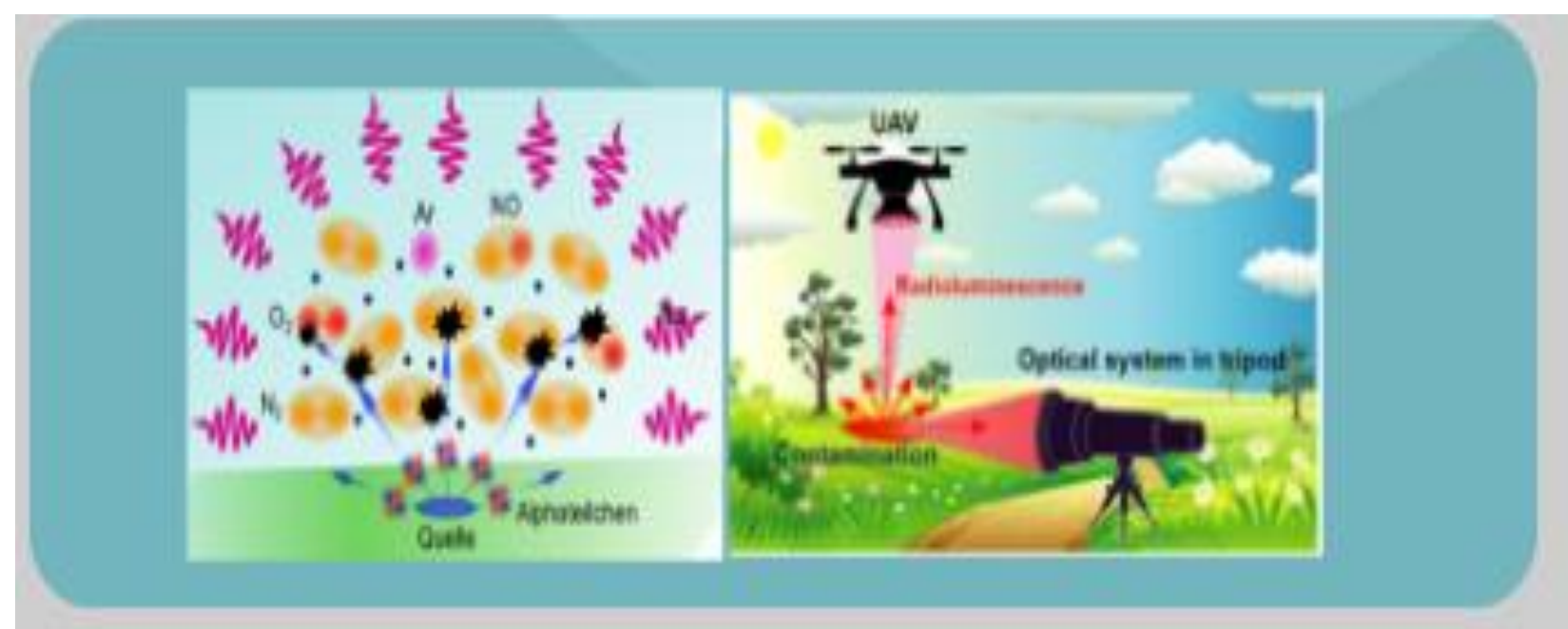


Figure 3. The optical spectrum of atmosphere alpha-radioluminescence under standard conditions.

Remote optical detection of alpha particle sources

Sergiy M Baschenko



Thomas Kerst's results (Academic Dissertation, 2017, Tampere University)

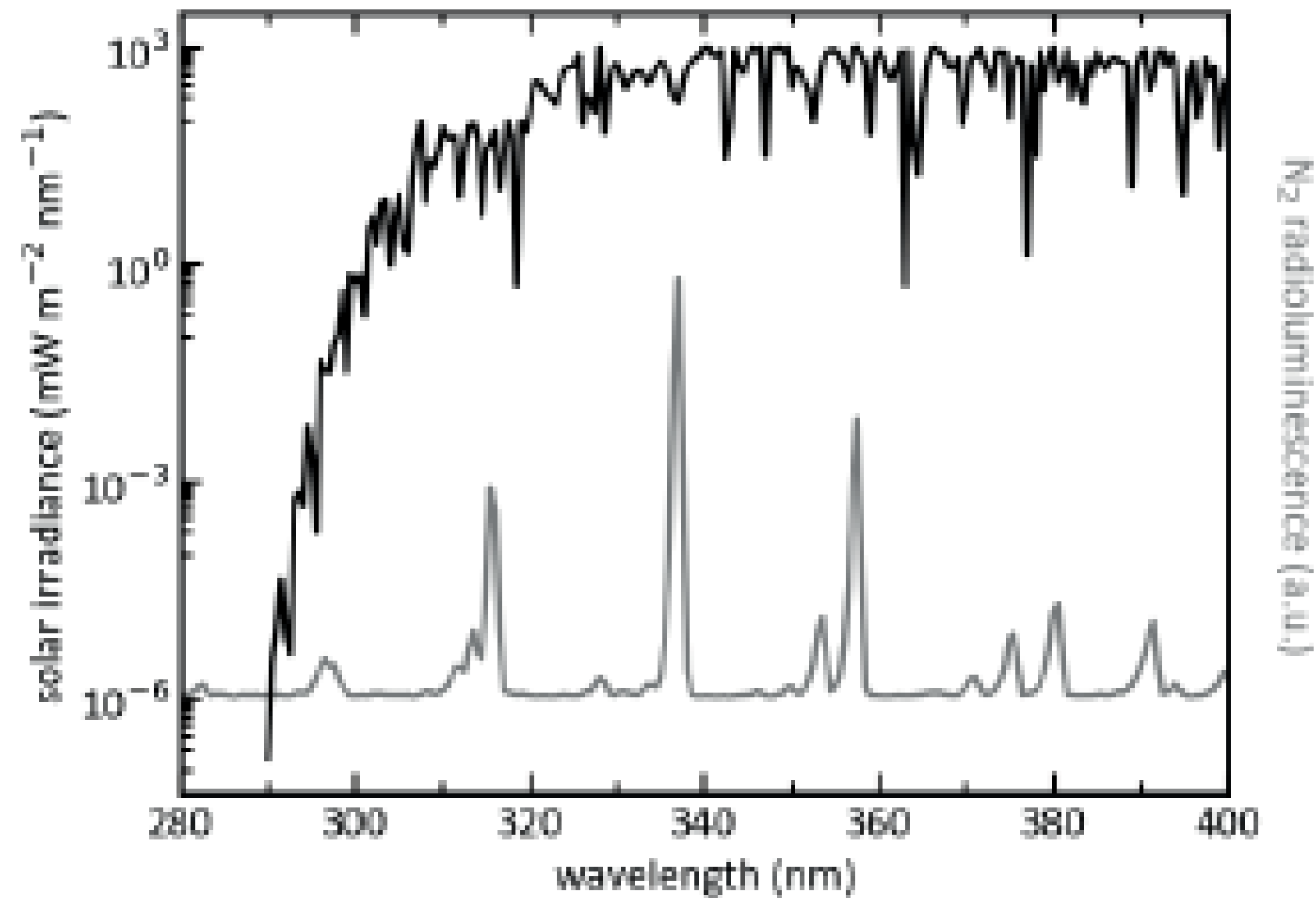


Fig. 1. Spectrum of sunlight reaching the earth's surface (black) contrasted with the radioluminescence of N_2 (gray) in the wavelength range 280 nm – 400 nm. The solar irradiance (AM1.5 Global tilt [11]) is displayed on a logarithmic scale, while the N_2 emissions are shown on a linear scale. At wavelengths longer than 290 nm the solar irradiance spectrally overlaps with the radioluminescence of N_2 .

„...Excitation of NO by excitation transfer via interaction with N_2 molecules appears to be able to explain our data. In this process, molecular nitrogen in the long-lived N_2 state excites ground state nitric oxide to the NO state, while the N_2 molecule loses its excitation and decays to the ground state...”

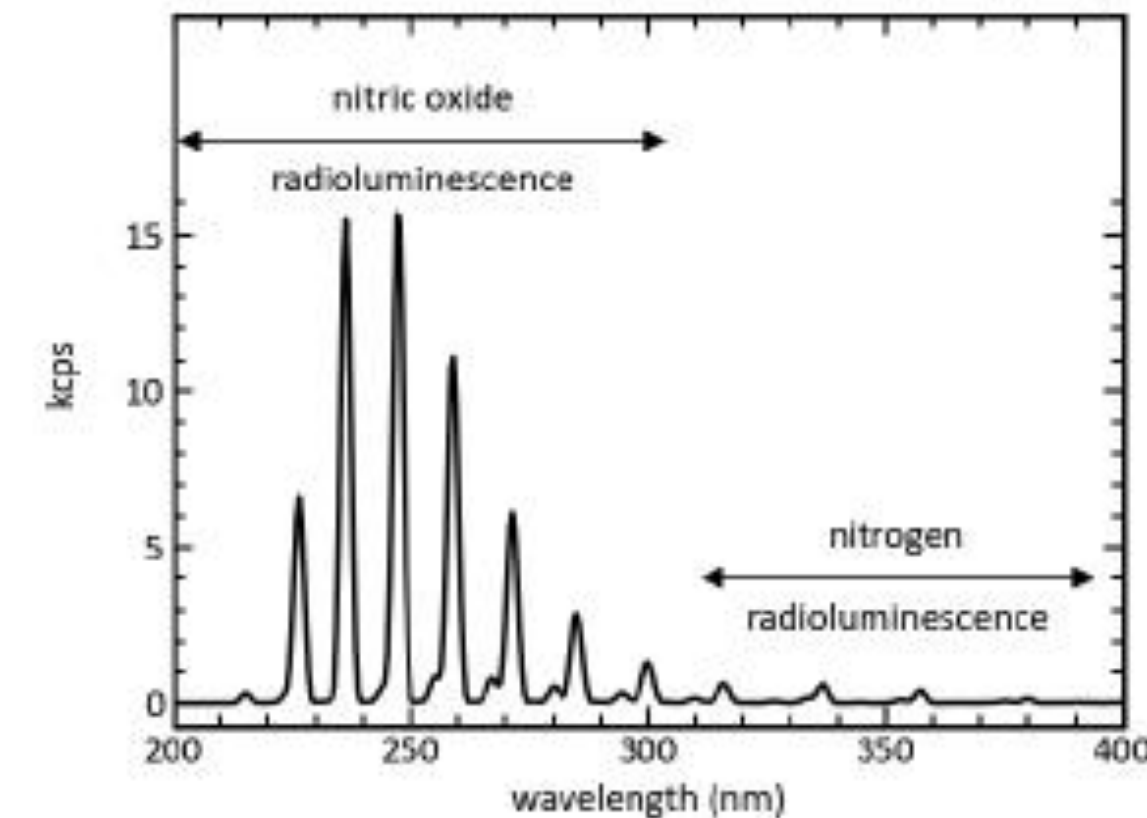
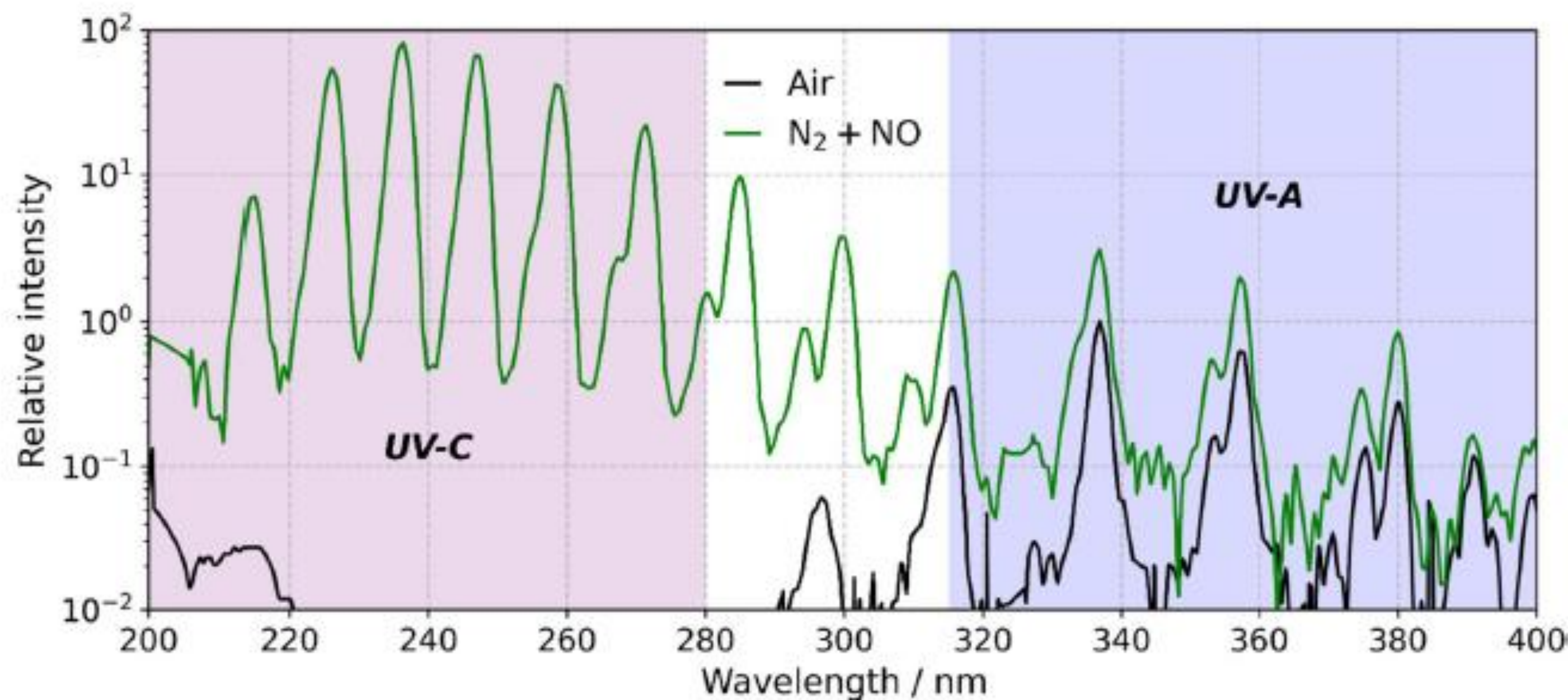


Fig. 4. Radioluminescence spectrum of gas a gas mixture containing 50 ppm of NO diluted in N_2 . The nitric oxide emission is about 25 times stronger than N_2 emission and most of the NO emission lines are located in the solar blind spectral region.

Table 1. The intensity of radioluminescence between 200 nm – 400 nm for three different gas environments. The intensity is expressed in relation to the intensity found in normal air, highlighting the improvement in photon yield by changing gases. The energy conversion efficiency shows how much of the energy deposited in air by an alpha particle is emitted as light.

Gas environment	Radioluminescence intensity	Energy conversion Efficiency	Reference
Air	1	$1 \cdot 10^{-4}$	Ref. 8
Nitrogen	6	$6 \cdot 10^{-4}$	Ref. 8
50 ppm of NO/ N_2	150	$2 \cdot 10^{-2}$	This work

Demonstration of an order-of-magnitude enhancement of scintillation using a gas mixture of N₂ +NO in UV-C solar blind range



Journal of Radioanalytical and Nuclear Chemistry
<https://doi.org/10.1007/s10967-023-09235-2>



Radioluminescence mapping of ²⁴¹Am-doped environmental samples and nuclear materials

Maksym Luchkov¹ · Claudia Olaru² · Ioana Lalau^{2,4} · Mastaneh Zadehraf² · István Róbert Nikolényi³ · Zoltán Gémesi³ · Mihail-Razvan Ioan² · Faton Krasniqi¹

Received: 31 July 2023 / Accepted: 22 October 2023
© The Author(s) 2023

Fig. 1 Typical alpha radioluminescence spectrum measured in dry air at normal temperature and pressure (NTP) and N₂+NO gas atmosphere with 2 ppm NO. In air, more than 95% of the total intensity is contained in the UV-A and UV-B spectral region (within 310 nm to 400 nm), while the intensity of UV-C radioluminescence (below 280 nm) is very low (<5%). The radioluminescence signal in the

UV-C spectral region can be enhanced by more than three orders of magnitude by purging the space around the alpha source with N₂+NO gas mixture. The spectra are measured with a CAS140D spectroradiometer at the PTB Ion Acceleration Facility (PIAF) with a narrowly collimated beam of 5 MeV alpha particles. The intensities are normalized to the 337 nm spectral line of air radioluminescence

The first laboratory CCD camera-based results on UV-C imaging and scannings

Krasniqi et al , 2021: Nuclear Inst. and Methods in Physics Research, A 987 (2021) 164821

- (a wide field-of-view (FOV) imaging system in conjunction with an intensified CCD camera (hereafter, CCD-based imaging system)
- a narrow FOV Galilean-type telescope combined with a cesium-telluride photocathode photomultiplier (hereafter, scanning PMT system).

Nuclear Inst. and Methods in Physics Research, A 987 (2021) 164821

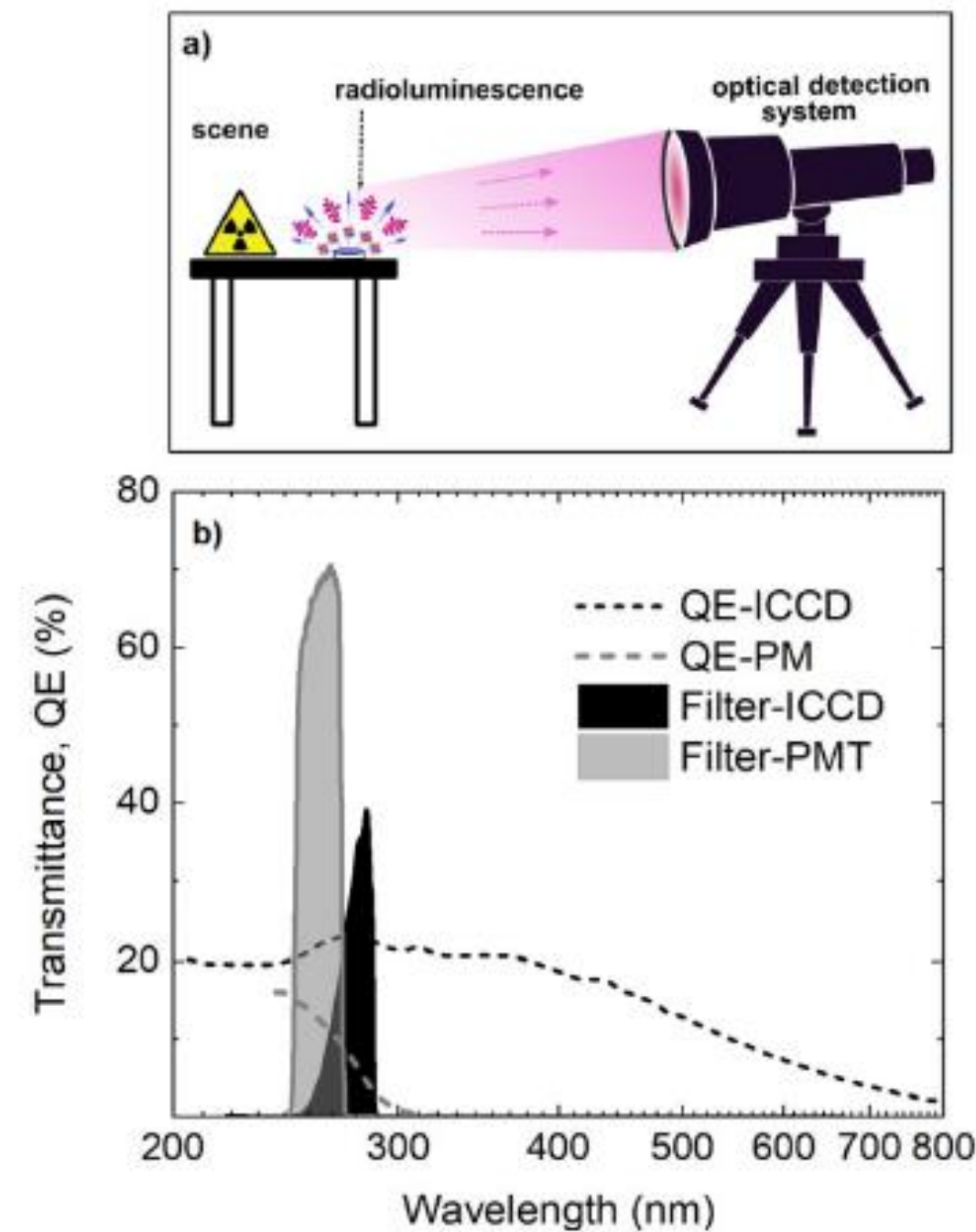


Fig. 1. (color online) (a) Schematic of the UV-C imaging setup. Radioactive material is placed either on the table or inside a steel chamber. The detection system is placed between 0.4 to 0.53 m away from the sample. (b) Quantum efficiency curves of the used detectors (ICCD camera and cesium-telluride photocathode photomultiplier tube) and transmission of the UV-C filters.

F.S. Krasniqi, T. Kerst, M. Leino et al.

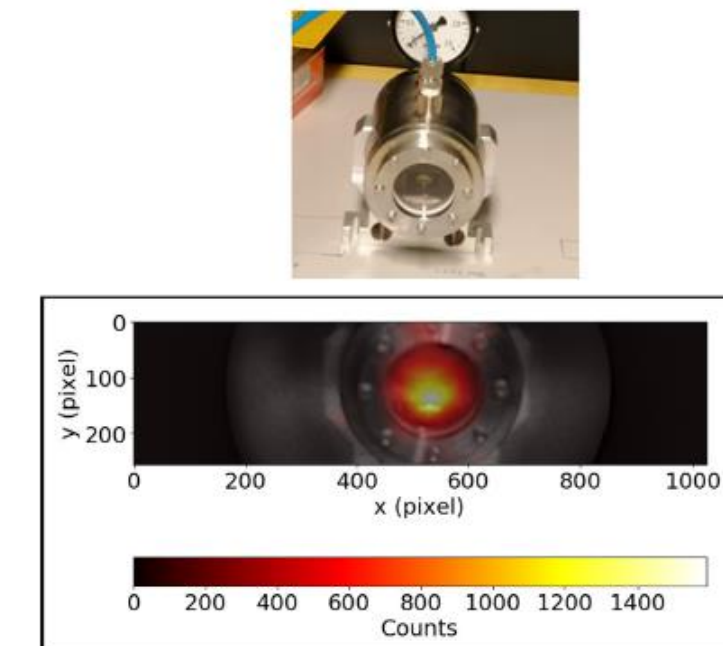


Fig. 3. (color online) UV-C radioluminescence imaging of 3.7 MBq source (lower panel) and a photograph of the sample in the experimental chamber (upper part). The alpha source was placed on a steel chamber with a quartz window, flushed with N_2 (6.0 purity) at a rate of 5 L/min. The NO concentration was 50 ppb.

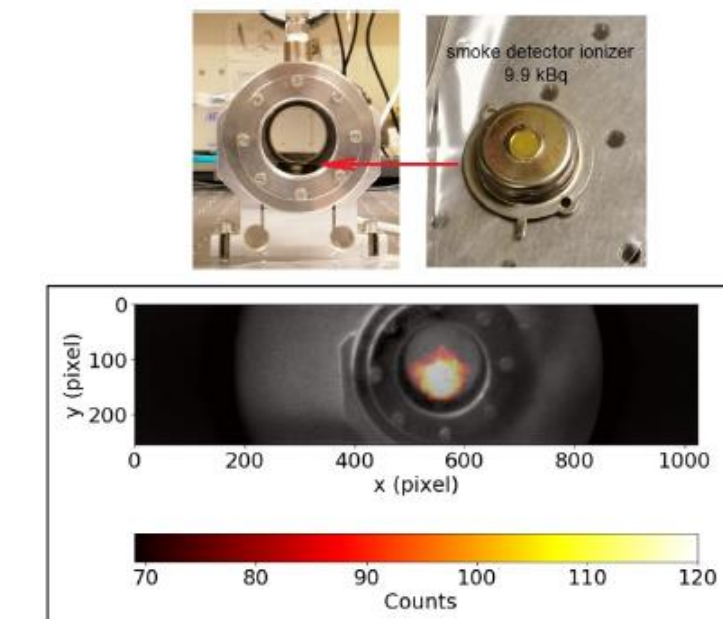


Fig. 4. (color online) UV-C radioluminescence image of a 9.9 kBq smoke detector ionizer. The concentration of NO at the N_2 atmosphere was about 3 ppm.

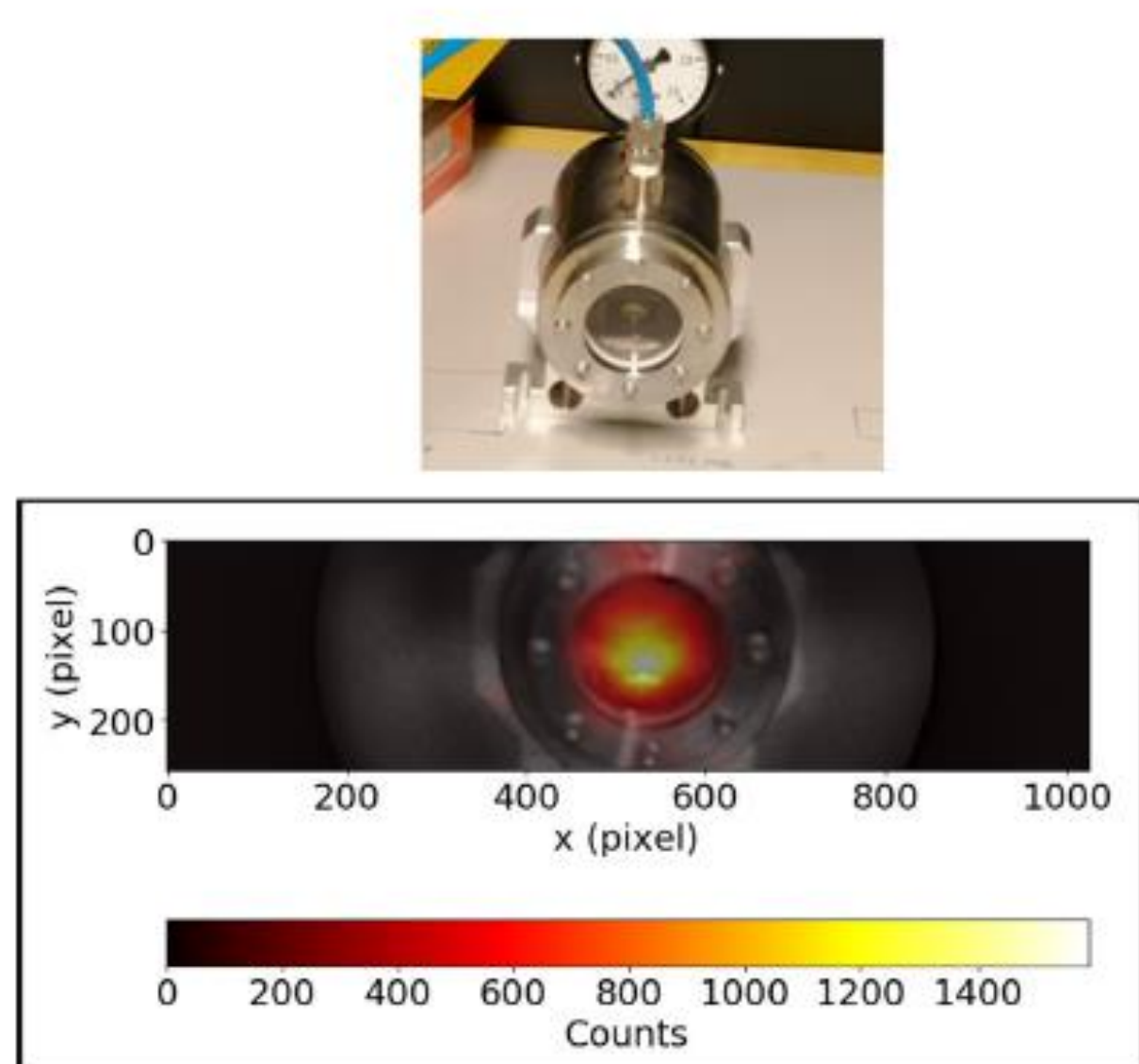


Fig. 3. (color online) UV-C radioluminescence imaging of 3.7 MBq source (lower panel) and a photograph of the sample in the experimental chamber (upper part). The alpha source was placed on a steel chamber with a quartz window, flushed with N_2 (6.0 purity) at a rate of 5 L/min. The NO concentration was 50 ppb.

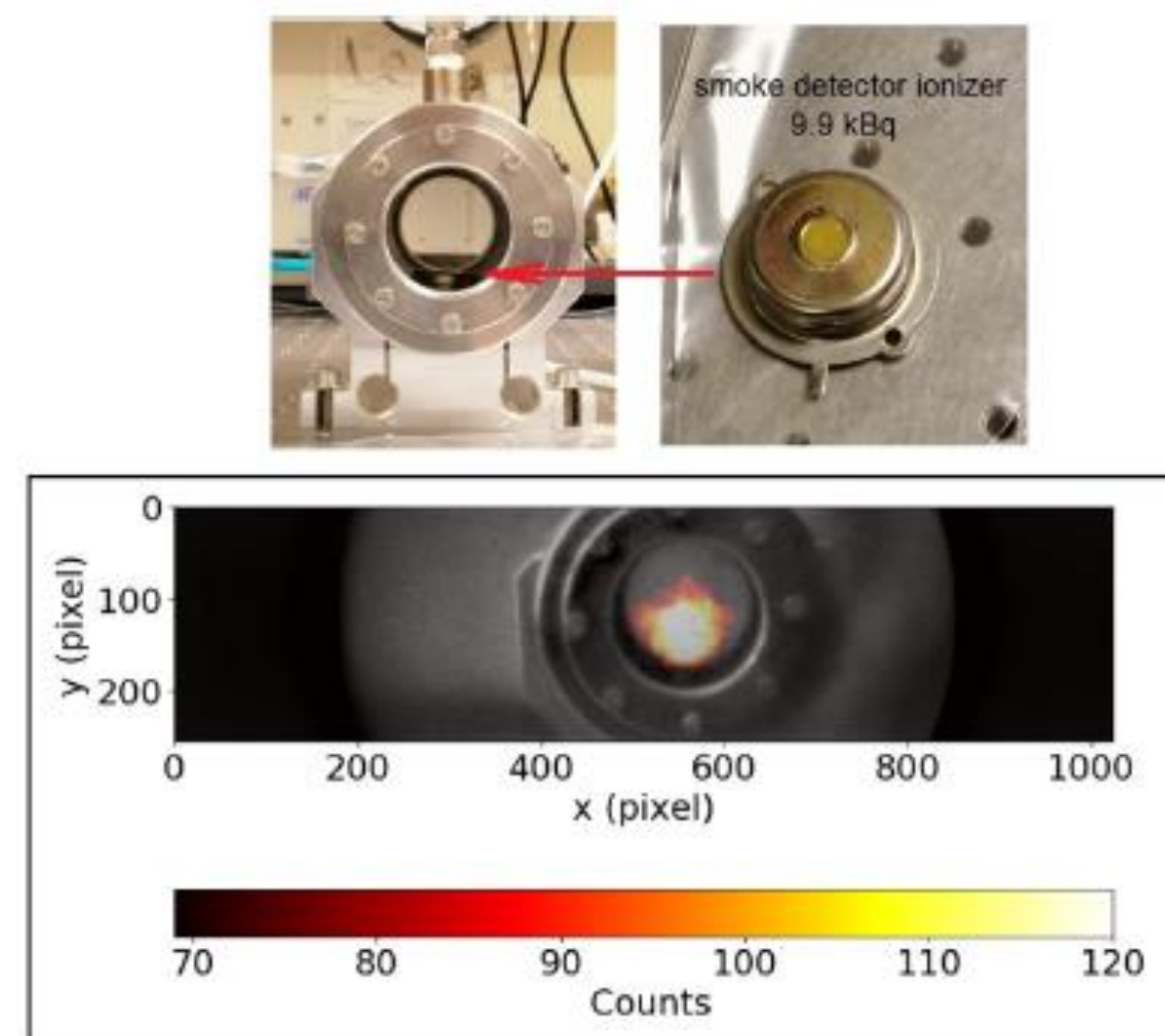


Fig. 4. (color online) UV-C radioluminescence image of a 9.9 kBq smoke detector ionizer. The concentration of NO at the N_2 atmosphere was about 3 ppm.

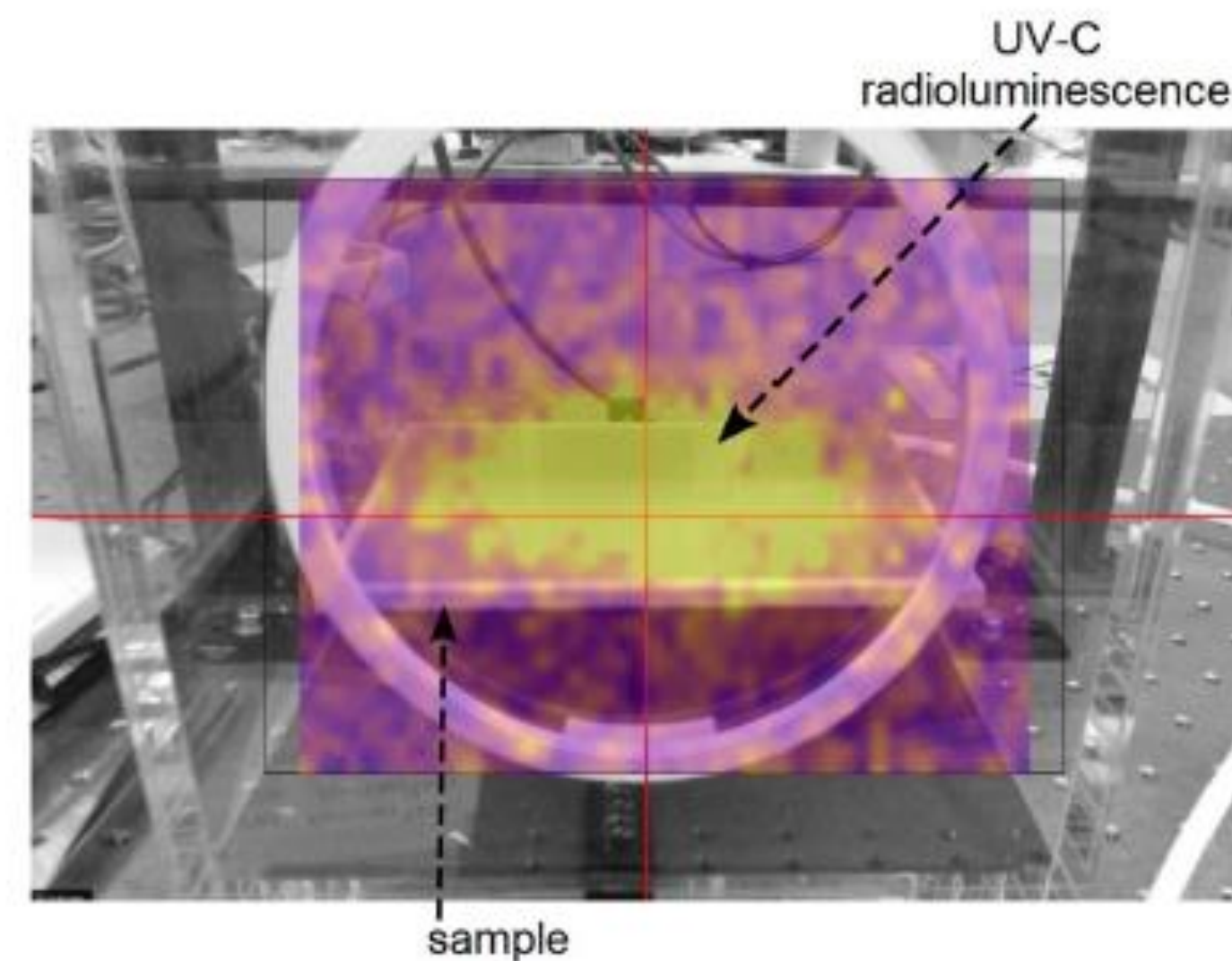


Fig. 6. (color online) Image of a wide area reference alpha-emitting source composed of the uranium isotopes U-234, U-235 and U-238, with a total activity of 330 Bq over an active area of $19.1 \times 11.9 \text{ cm}^2$. The concentration of NO at the N_2 atmosphere was about 3 ppm. The scene was scanned using scanning PMT system at about 0.4 m distance with a resolution of 1 deg and 30 s integration per point.

F.S. Krasniqi, T. Kerst, M. Leino et al.

an average signal level of about 75 cps and a noise level of about 31 cps. To the best of our knowledge, this is the lowest activity imaged using UV-C radioluminescence to date. The present results indicate that optimizing such imaging techniques can push the detection limit even further down and such techniques might also be used for determination of legal limits in the future.

„...the feasibility of detecting low activity in environmental samples by measuring their radioluminescence with the optical detection system ...”

A. Klose et al 2022: Journal of Radioanalytical and Nuclear Chemistry (2022) 331:5401–5410

- As calibration standard, pitchblende minerals were prepared
- alpha-track-detection was used for analysing the homogeneity of the alpha-emitter distribution on the pitchblende samples
- alpha-spectroscopy was performed using a grid ionisation chamber (GIC). with *P10*, a gas mixture of 90% argon and 10% methane, at a pressure of 1.025 bar.

Preparation

Pitchblende bearing ores from different locations with a comparatively high uranium content were cut into 5 mm thick slices with a micro-waterjet. The resulting surface is flat but not polished. The shape of the samples is irregular and their surface sizes range from about one to 15 cm².

2+




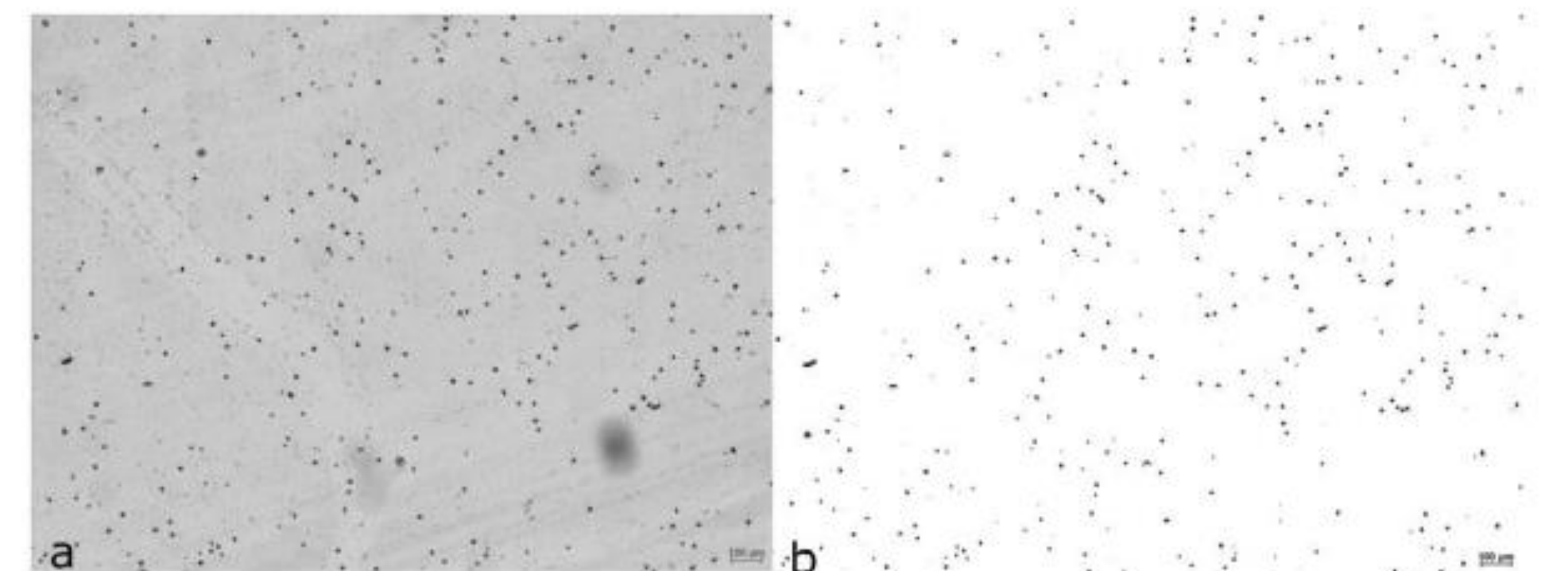
Sample	Origin	Size [cm ²]	Mass [g]	Picture
J	Wölsendorf	13.1	16.4	
K	Wölsendorf	14.5	38.61	
L	Puy de Dôme	6.6	5.69	

Fig. 3 Alpha-track of sample L after 1 min exposure
Raw data shown in (a). Adjusting the threshold generates a black-white-image (b). The tracks are highlighted and can be further analysed. For this example, the number of tracks was counted. It is 548 on a total area of 2.49 mm by 1.87 mm.



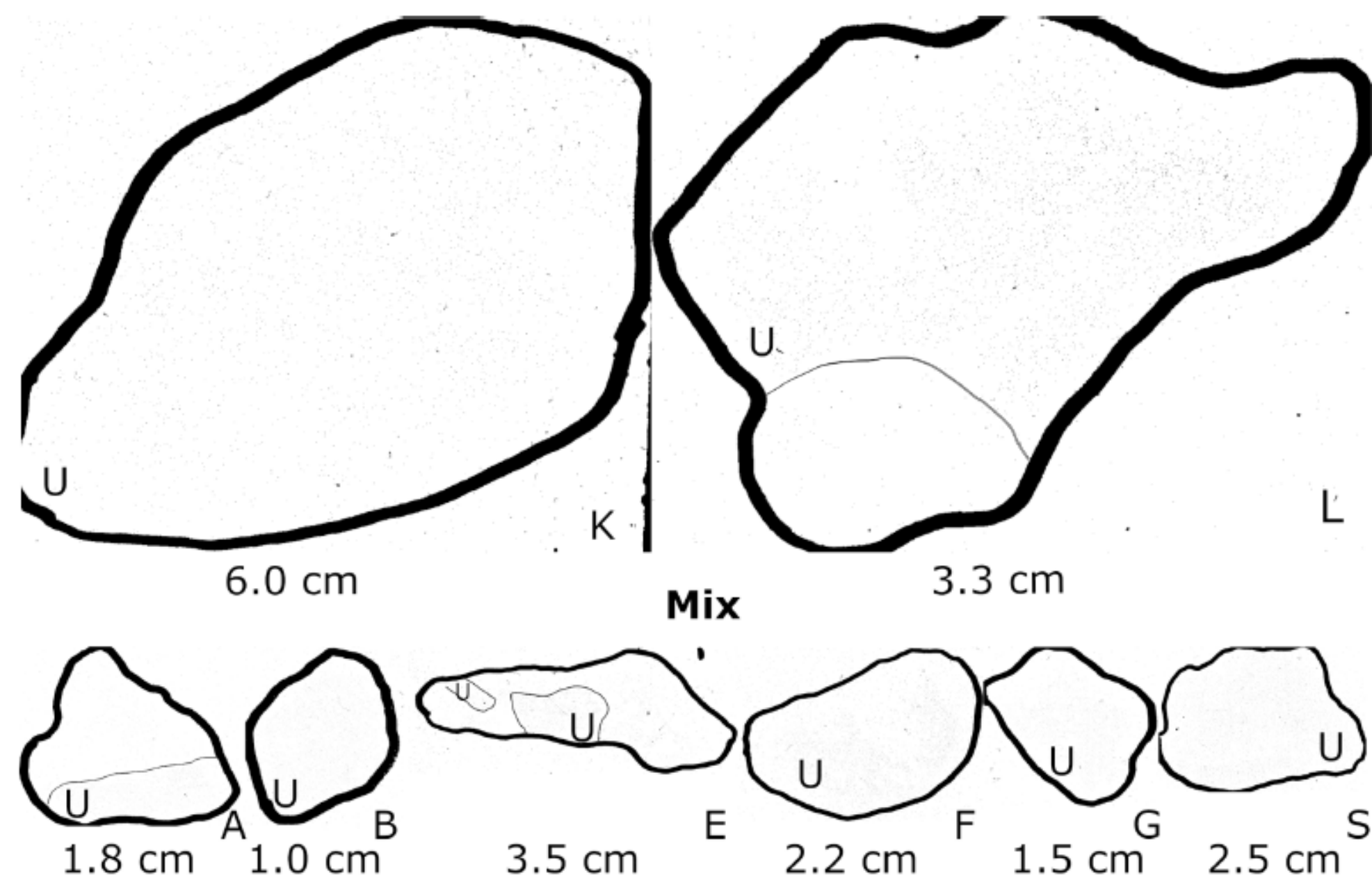


Fig. 4 Alpha-Track-Images of three different samples
Except for A and E from sample Mix, the alpha-emitters are

homogeneously distributed over the entire surface area. Areas containing much uranium and its daughters are labelled with “U”

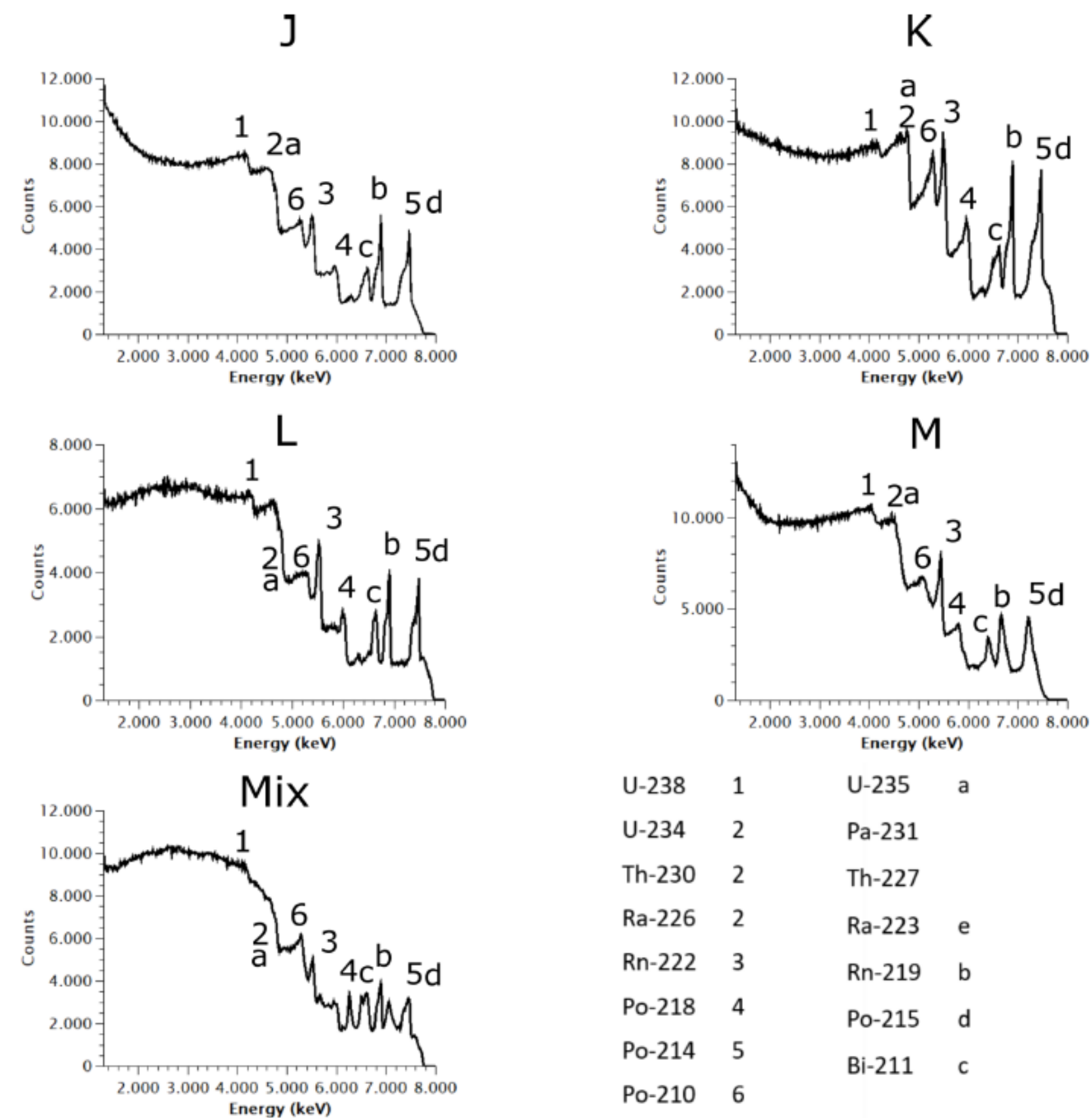


Fig. 5 GIC-Spectra of pitchblende samples J, K, L, M and Mix
The measurement time was normalized to 3000 s for each spectrum.

They show a large amount of low energy alpha particles due to self-absorption. Numbers identify nuclides of the ²³⁸U decay chain whereas letters identify nuclides of the ²³⁵U decay chain

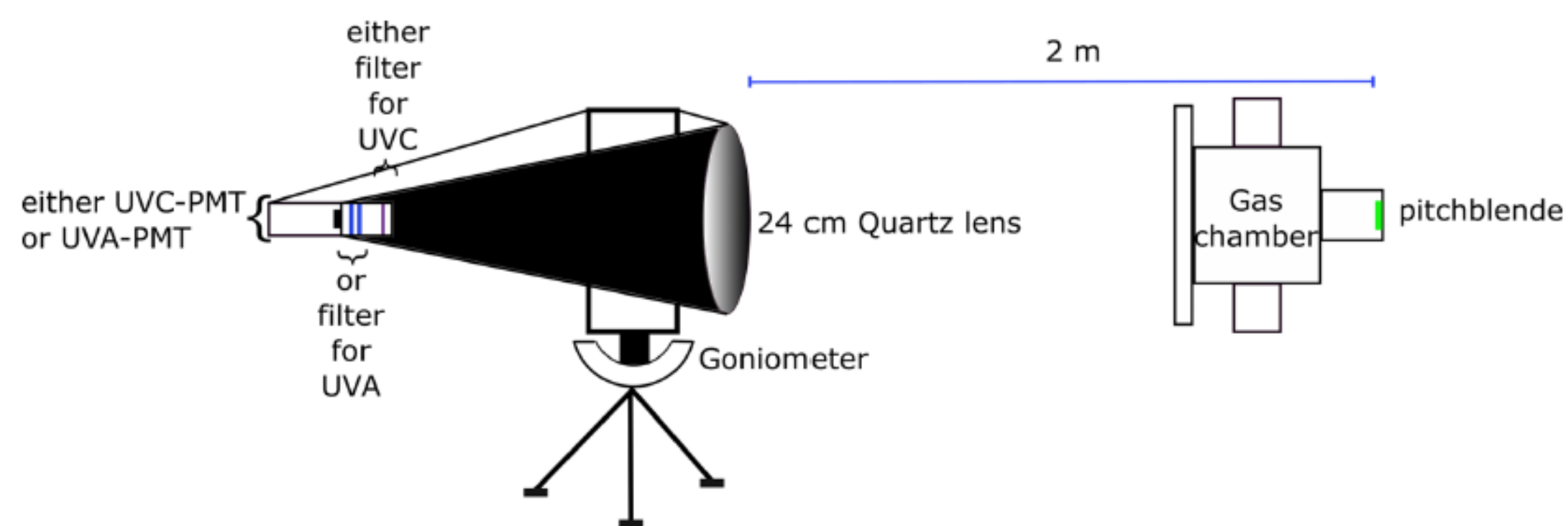


Fig. 1 The optical scanning system
The optical system is mounted at a distance of 2 m away from the sample. Depending on the kind of measurement, the gas chamber can

be filled with air or different gas mixtures like N_2 and 10 ppm NO. The PMT and corresponding set of filters is changed for measurements in UVA and or UVC

Fig. 7 Arrangement of different pitchblende samples and UVA-Scan in air for 64 h

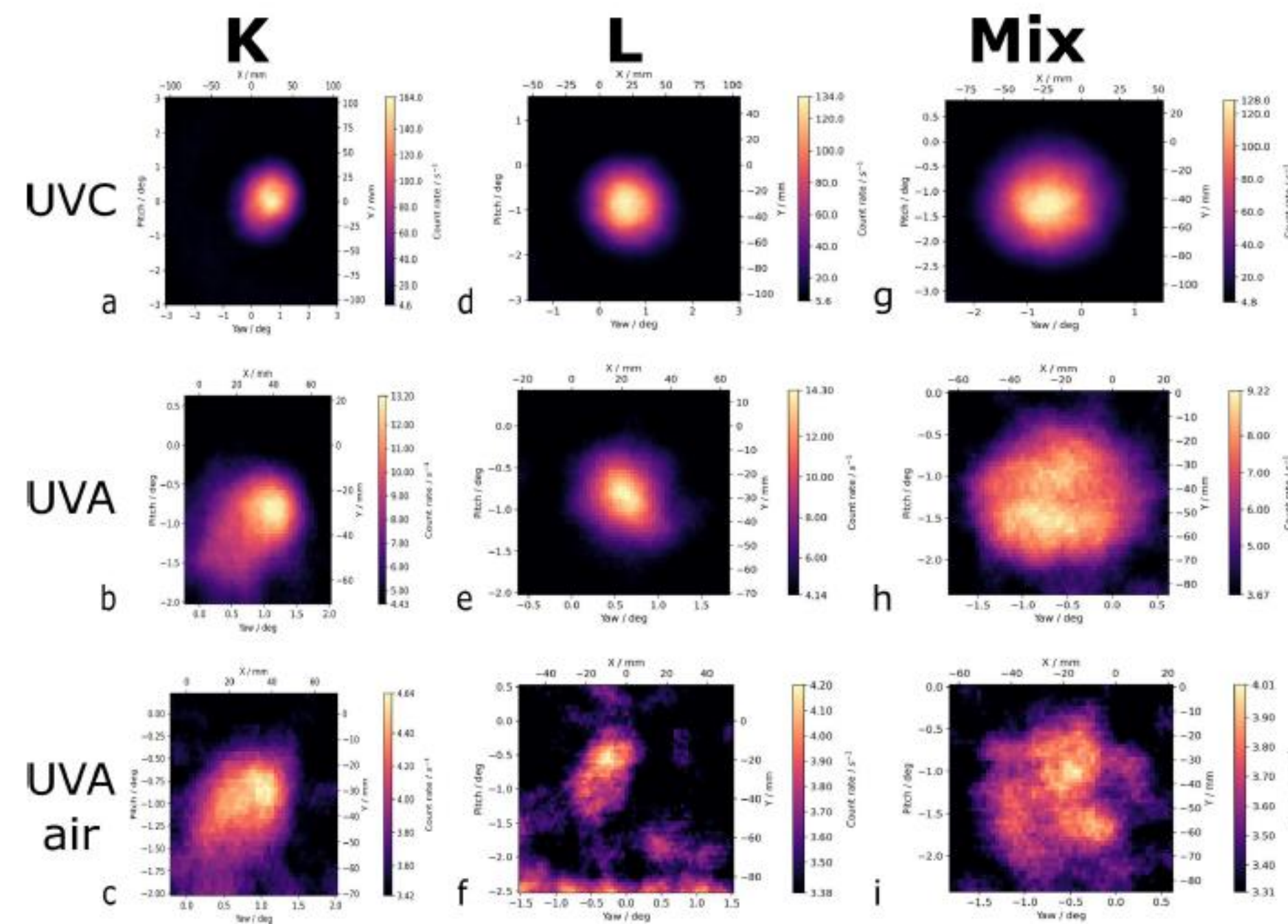
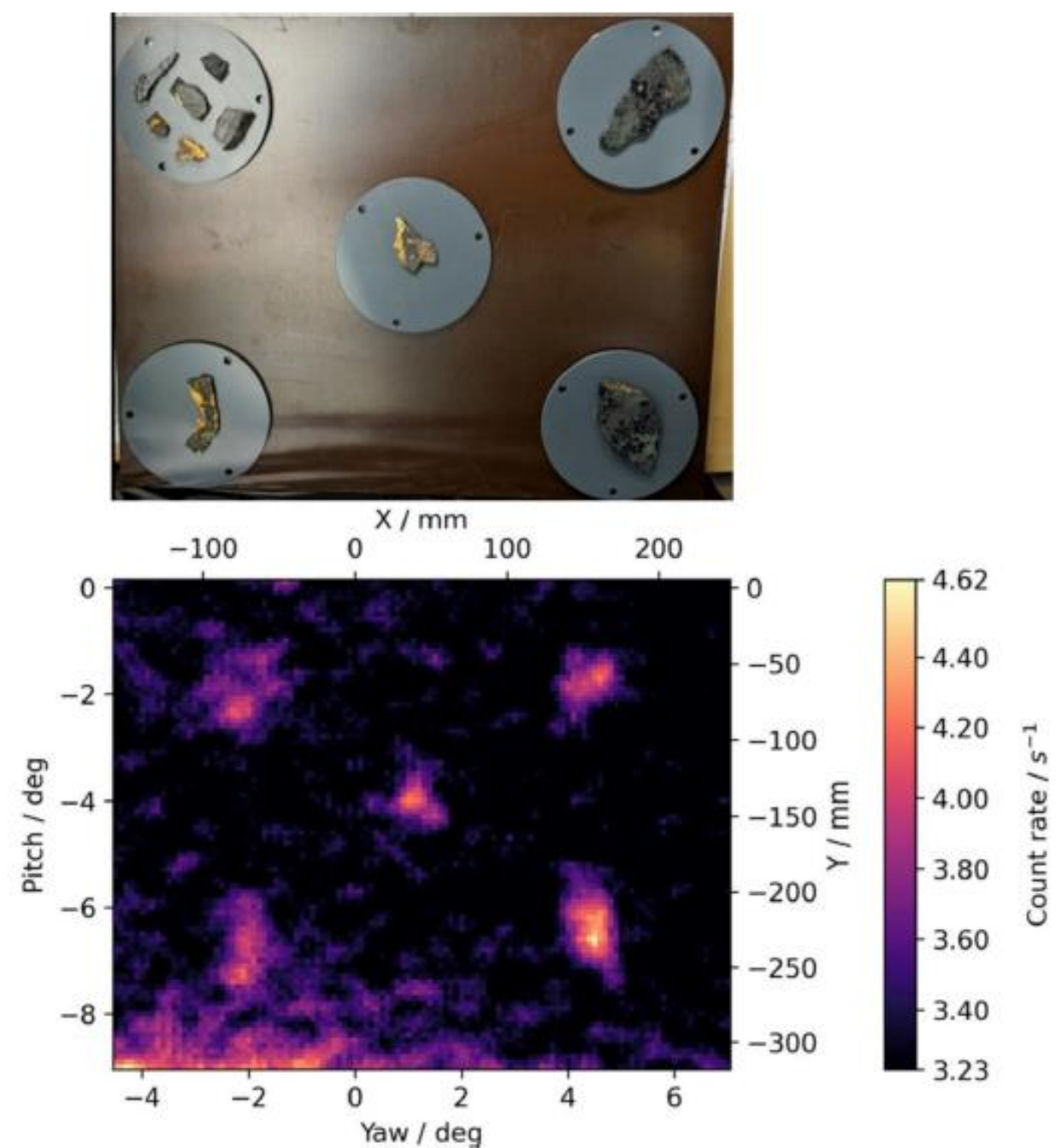


Fig. 6 Radioluminescence scans
The measurement in UVC yields the highest intensity for all samples (upper row) and the biggest radioluminescence glow. Both measurements in UVA have a smaller glow due to the smaller field of view. The background rate is higher as for measurements in UVC. Using the artificial atmosphere (middle row) leads to a three times higher signal than measuring in air (lower row). All samples have a similar surface activity and a similar photon count rate.

Table 5 Comparison of surface alpha count rate with photon count rates of the radioluminescence measurements

Sample	GIC (CPS)	UVC (CPS)	UVA (CPS)	UVA air (CPS)
K	1520(39)	1E6	3E3	6E1
L	1023(32)	2E5	3E3	1E2
Mix	1493(39)	4E5	4E3	5E1

The two optical ranges and the developed lens-filter-PMT based measuring systems, M.Luchkov et al, 2022: Nuclear Inst. and Methods in Phys. Research, A

For all measurements in the UV-C spectral region, the Hamamatsu PMT with CsTe photocathode (H11870-09) was used with bandpass interference filters having a bandwidth of 16 nm and center wavelength of 260 nm (FF01-260/16-25, Semrock Inc.).

In the UV-A spectral range, Hamamatsu PMT with ultra-alkali photocathode (H10682-210) was used with interference filters centered at 337 nm with a bandwidth of 10 nm (# 65-128, Edmund Optics). Both PMTs were selected for a very low dark rate, i.e. the UV-C PMT has a dark count rate of less than 1 s^{-1} , while the UV-A has less than 10 s^{-1} .

- high-quality UV fused silica (UVFS) lens, for tripod
- and the other two were
- PMMA (Poly(methyl 2methylpropenoate) Fresnel lenses for UAV

M. Luchkov, V. Dargendorf, U. Giesen et al.

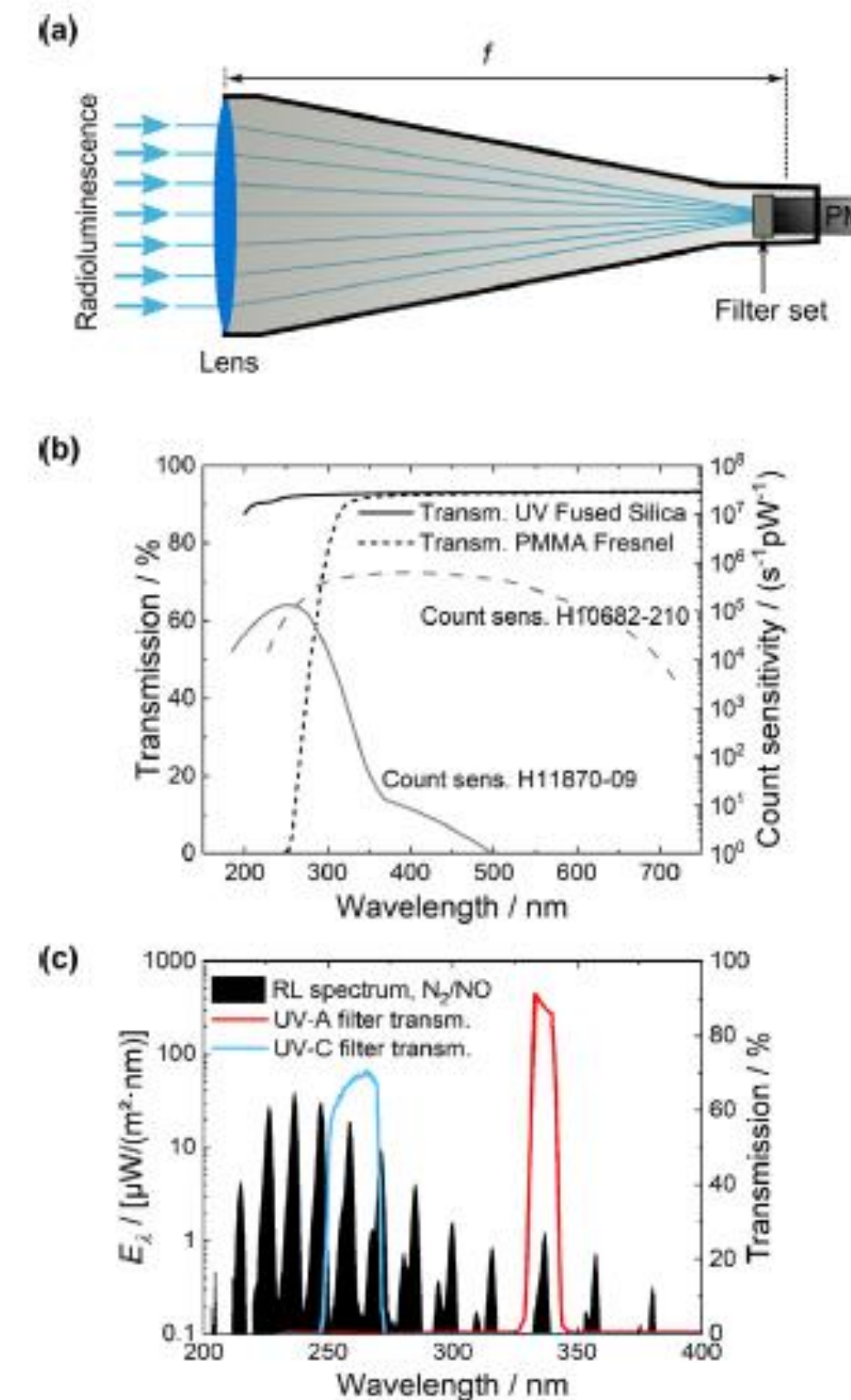


Fig. 2. (a) Schematic drawing of optical systems developed in the framework RemoteALPHA project. Both, the UVFS- and PMMA Fresnel-lens systems share the same configuration: they utilize large receiving optics to maximize the geometric factor, and the focal lengths have been chosen such that the radioluminescence image is not blurred substantially by the overlapping FOVs between adjacent scanning points. (b) Transmittance spectra of UVFS [22] and PMMA [23] together with the PM count sensitivity [24,25] specified by the manufacturer. (c) Radioluminescence emission spectrum of NO measured at the PIAF at a nominal alpha particle rate of about $30 \times 10^6 \text{ s}^{-1}$ with a PTB-calibrated array spectroradiometer with UV-C and UV-A filter transmission [26,27]. The flow rate of $\text{N}_2 + \text{NO}$ was set at $2400 \text{ mL} \cdot \text{min}^{-1}$ with a concentration of $5 \mu\text{L} \cdot \text{L}^{-1}$.

Nuclear Inst. and Methods in Physics Research, A 1047 (2023) 167895

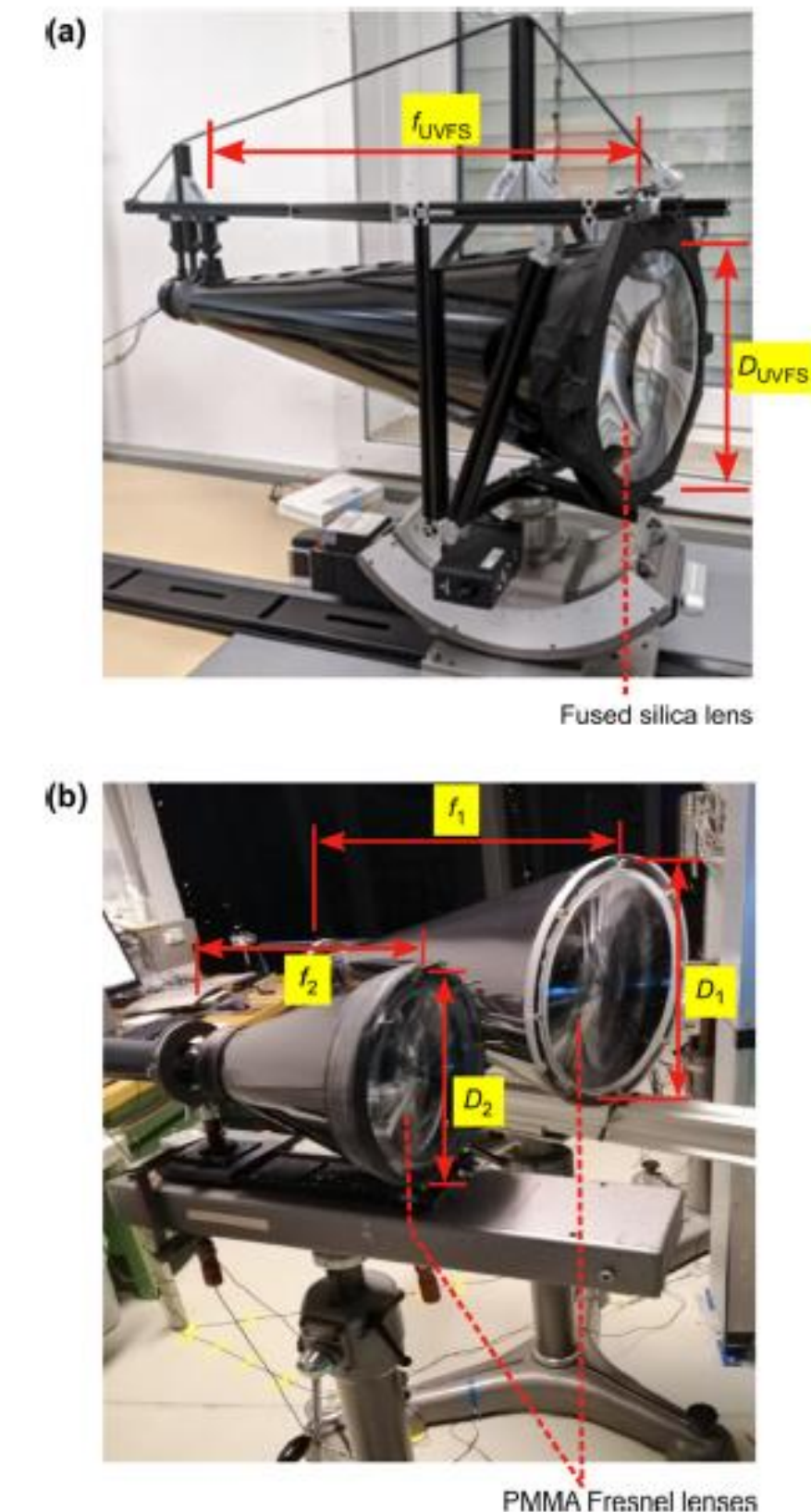


Fig. 3. Lens-based radioluminescence detection setups. (a) Fused silica lens (Abet Technologies) system mounted on a goniometer and rotation stage (Newport M-BGM160PE and RVS80CC) with $D_{\text{UVFS}} = 240 \text{ mm}$ and f_{UVFS} between 572 mm to 599 mm in a wavelength range from 236 nm to 285 nm, respectively. (b) PMMA Fresnel lens systems with lenses (Orafol Fresnel Optics) having diameters $D_1 = 452.9 \text{ mm}$ (SC 2045) and $D_2 = 257.6 \text{ mm}$ (SC 210), and nominal focal lengths $f_1 = 391.5 \text{ mm}$ and $f_2 = 225.5 \text{ mm}$ at 546 nm. All lens systems can be coupled to Hamamatsu PMTs (H10682-210 for UV-A spectral range and H11870-09 for UV-C spectral range) and UV-C filters (FF01-260/16-25, Semrock Inc.) or UV-A filters (337 nm, 10 nm band-pass filters from Edmund Optics).

Test and demonstration of the radioluminescence mapping capability

The radioluminescence mapping capability is demonstrated with the UVFS telescope which has been used to obtain the radioluminescence image of (a) deceleration of alpha particles at the exit port of the PIAF microbeam, (b) dedicated Am-241 sample designed to simulate an extended alpha source, and (c) low activity pitchblende minerals with surface activity between 80 Bq cm^{-2} and 105 Bq cm^{-2} .

- The detection efficiency of all systems has been measured at the PTB Ion Accelerator Facility (PIAF) where alpha particles with a rate from $5 \times 10^4 \text{ s}^{-1}$ to about $4.5 \times 10^7 \text{ s}^{-1}$, collimated to a beam size of $100 \mu\text{m} \times 100 \mu\text{m}$, have been accelerated to energies up to 8.3 MeV.
- The relationship between radioluminescence photons and alpha activity is calibrated with a dedicated ^{210}Po activity

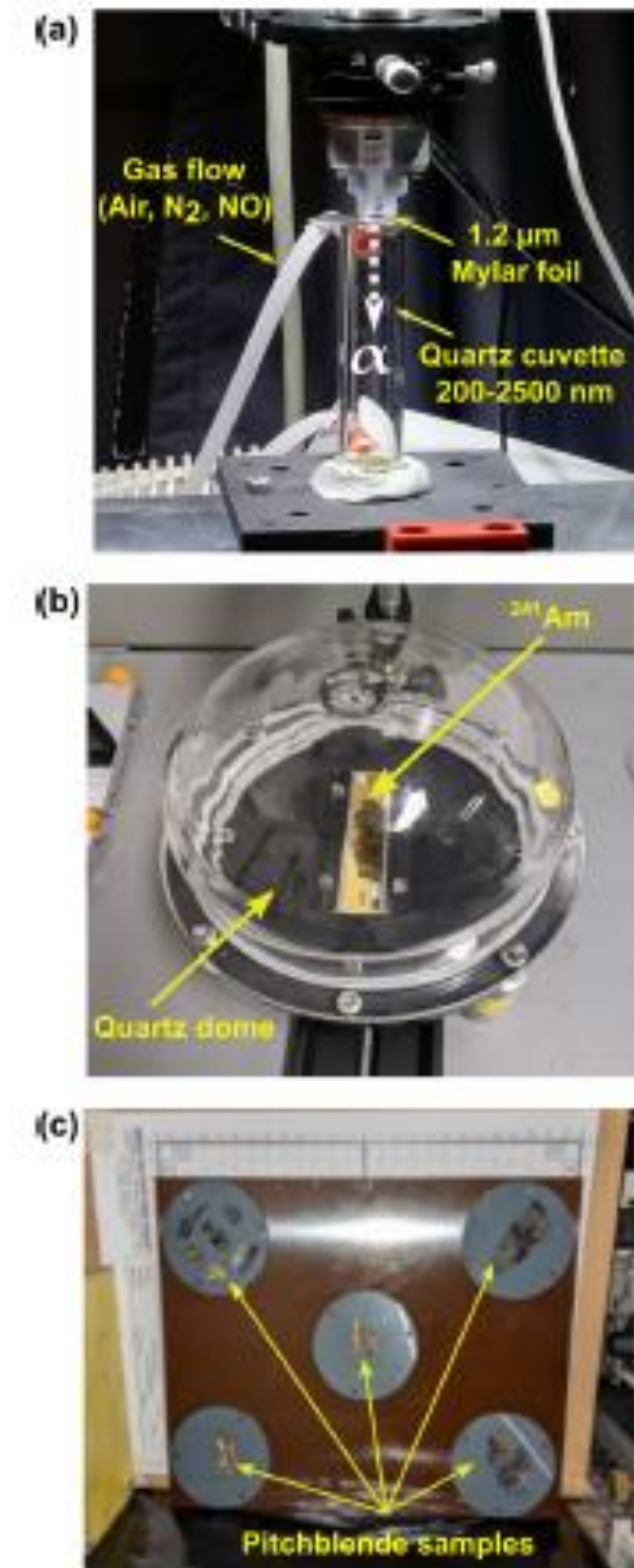


Fig. 4. (a) Photo of the alpha particle interaction region at the PIAF. The PIAF microbeam was focused into a quartz cuvette (Hellma Analytica, cylindrical quartz cuvette with two tubes, wavelength range 200 nm–2500 nm, 100 mm path length) which could be filled with different gases (air, N_2 , N_2 -NO mixture). (b) Photograph of the Am-241 source (Eckert & Ziegler Gase) inside a quartz dome. (c) Arrangement of pitchblende mineral samples. The samples were cut from pitchblende-bearing ores with a micro water jet into slices with flat unpolished surfaces (for details, see [29]).

In all cases, the radioluminescence count rate is linearly proportional to the alpha particle rate. At a reference distance of 2 m between the radioluminescence source (i.e., the cuvette in which the alpha particles are stopped) and the receiving optics, both lens systems capture a part of the alpha particle path length around the Bragg peak (i.e., the last 3 cm of their path). Since the energy loss curves around the Bragg peak are similar for energies between 5 MeV and 8.3 MeV used in these experiments, the sensitivity of both systems is relatively independent of the alpha particle energy. This observation can be seen in Fig. 6, where the radioluminescence count rates measured with

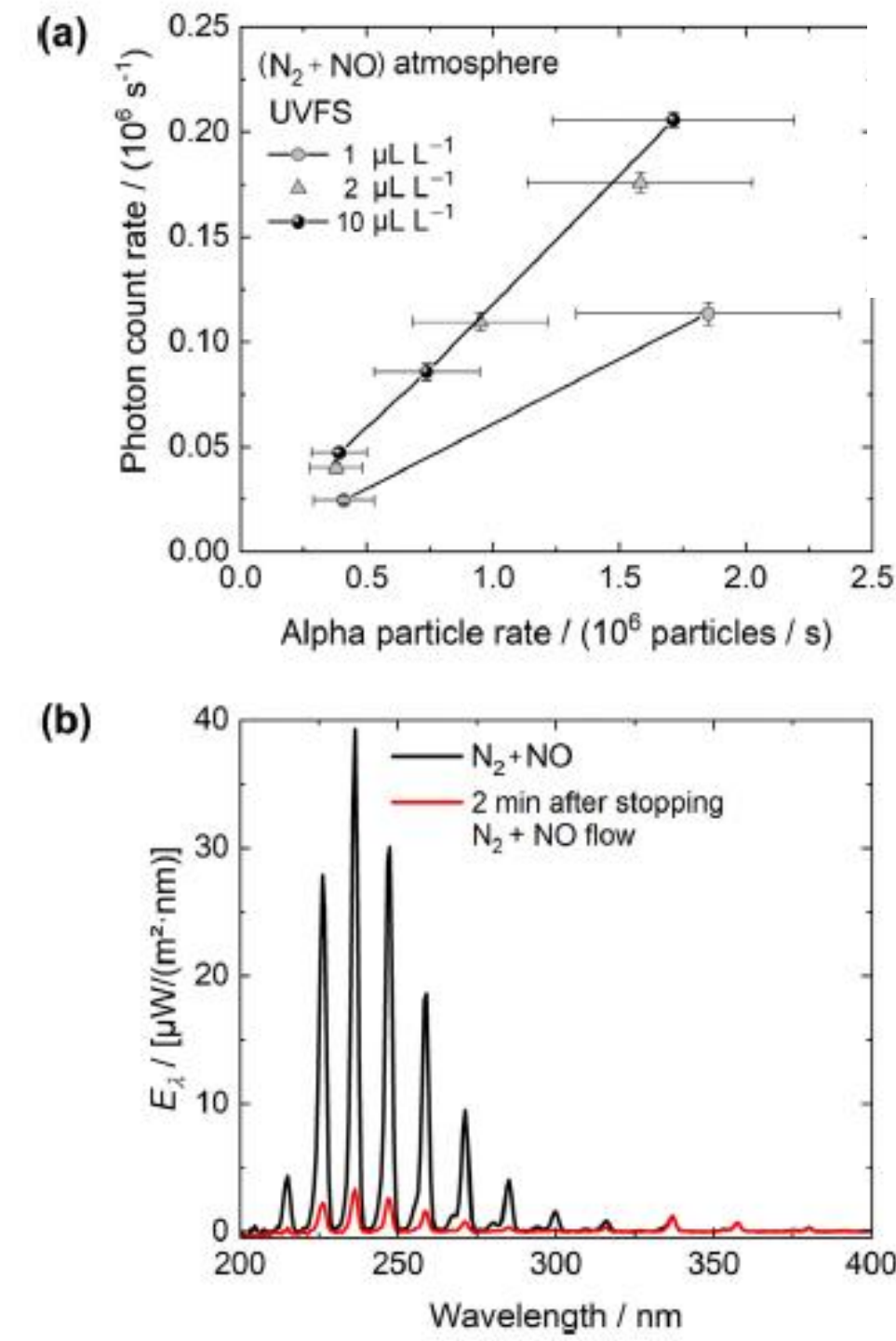
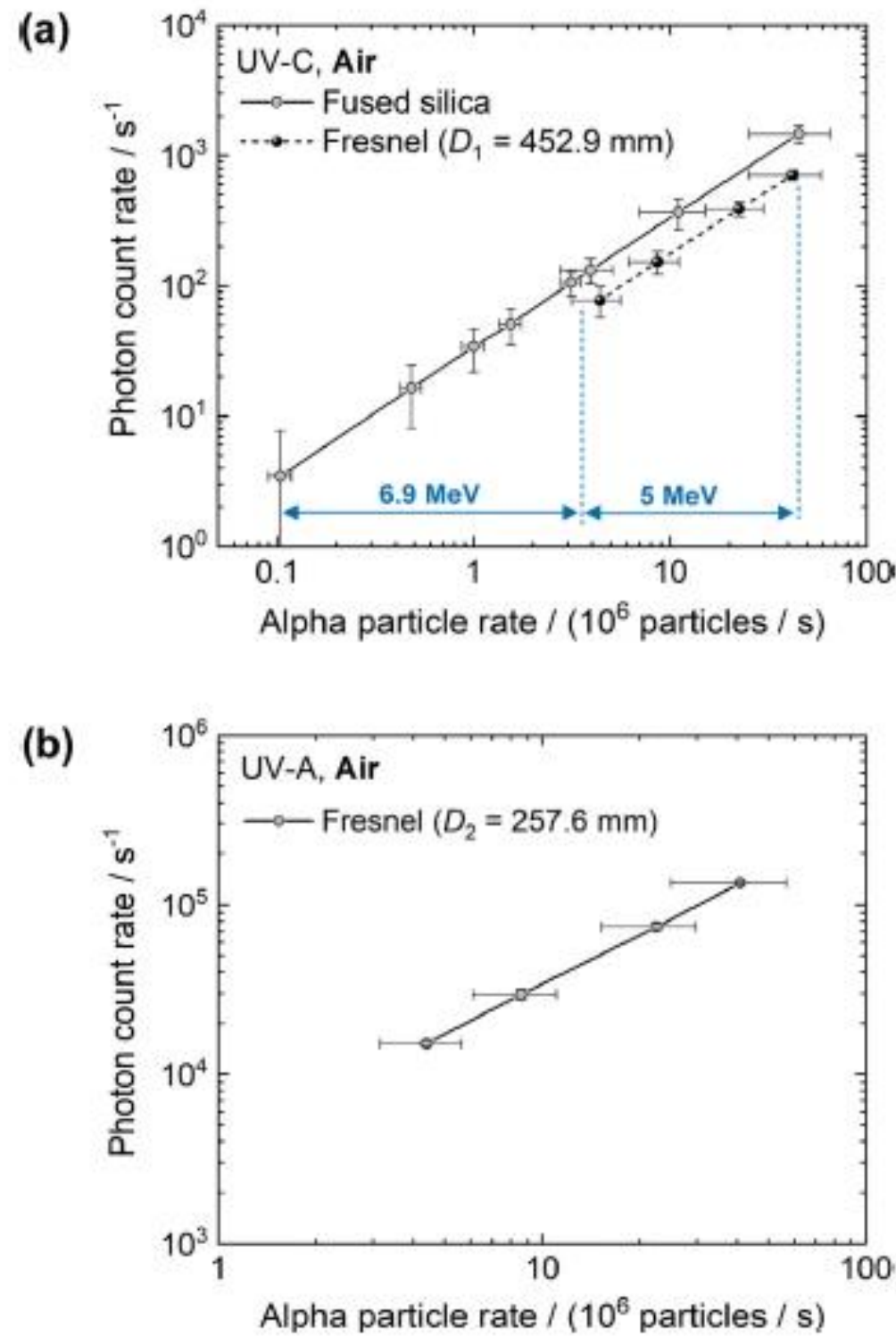


Fig. 6. (a) Comparison of UV-C radioluminescence sensitivities in air measured at the PIAF at a reference distance of 2 m between the radioluminescence source and lens. The slopes of linear fits are $34(6)s^{-1}MBq^{-1}$ for the UVFS and $17(3)s^{-1}MBq^{-1}$ for the Fresnel 1 ($D_1 = 452.9$ mm) lens systems at a background rate of $0.7(27)s^{-1}MBq^{-1}$ for both systems. Due to the finite FOV of both systems, the sensitivities for alpha particle energies of 5 MeV and 6.9 MeV are similar. (b) UV-A radioluminescence count rate generated by 5 MeV, measured with the Fresnel 2 lens system ($D_2 = 257.6$ mm). The signal slope is $3400(500)s^{-1}MBq^{-1}$.

Fig. 7. (a) UV-C radioluminescence count rate generated by 5 MeV alpha particles, measured at the PIAF at a reference distance of 2 m between the radioluminescence source and the UVFS lens. The UV-C counting rate can be increased by more than three orders of magnitude by purging the cuvette with a N_2+NO gas mixture at a NO concentration above $2 \mu L L^{-1}$. The UV-C sensitivity at $2 \mu L L^{-1}$ is $1.3 \times 10^5 s^{-1}MBq^{-1}$. At NO concentrations above $2 \mu L L^{-1}$, the UV-C signal saturates. A similar trend is observed also with the Fresnel lens system. (b) Radioluminescence emission spectrum of NO measured at the PIAF at a nominal alpha particle rate of about $30 \times 10^6 s^{-1}$ with a PTB-calibrated array spectroradiometer. Two minutes after stopping the flow of NO and N_2 , the UV-C radioluminescence signal drops by a factor of 10 relative to the one measured with N_2+NO purging.

Table 1
Comparison between calculated sensitivities using Eq. (1) and those measured with the three lens-based radioluminescence detection systems.

Detection system	Lens material	Filters	PMT	Calculated sensitivity ($s^{-1}MBq^{-1}$)	Measured sensitivity ($s^{-1}MBq^{-1}$)
UVFS in UV-C	UV fused silica	2 filters (FF01-260/16-25, Semrock Inc.)	Hamamtsu H11870-09	36	34 ± 6
UVFS in UV-A	UV fused silica	2 filters (65-128, Edmund Optics)	Hamamtsu H10682-210	3810	Not measured
Fresnel 1 in UV-C	PMMA	2 filters (FF01-260/16-25, Semrock Inc.)	Hamamtsu H11870-09	18	17 ± 3
Fresnel 2 in UV-A	PMMA	2 filters (65-128, Edmund Optics)	Hamamtsu H10682-210	4500	3400 ± 500

$$s = \frac{\Omega}{4\pi} \cdot \int Y(\lambda) \cdot T_{src}(\lambda) \cdot T_{lens}(\lambda) \cdot T_{filt}(\lambda) \cdot QE(\lambda) \cdot d\lambda \quad (1)$$

where Ω is the solid angle in steradians, $Y(\lambda)$ photon yield expressed in photons per alpha particle [5], $T_{src}(\lambda)$ is the transmission of the source enclosure (quartz cuvette for the beam), $T_{lens}(\lambda)$ is the lens transmission, $T_{filt}(\lambda)$ is the filter assembly transmission, and $QE(\lambda)$ is the quantum efficiency of the PMT in counts per photon. Filter transmission and quantum efficiencies of PMTs can be found on the

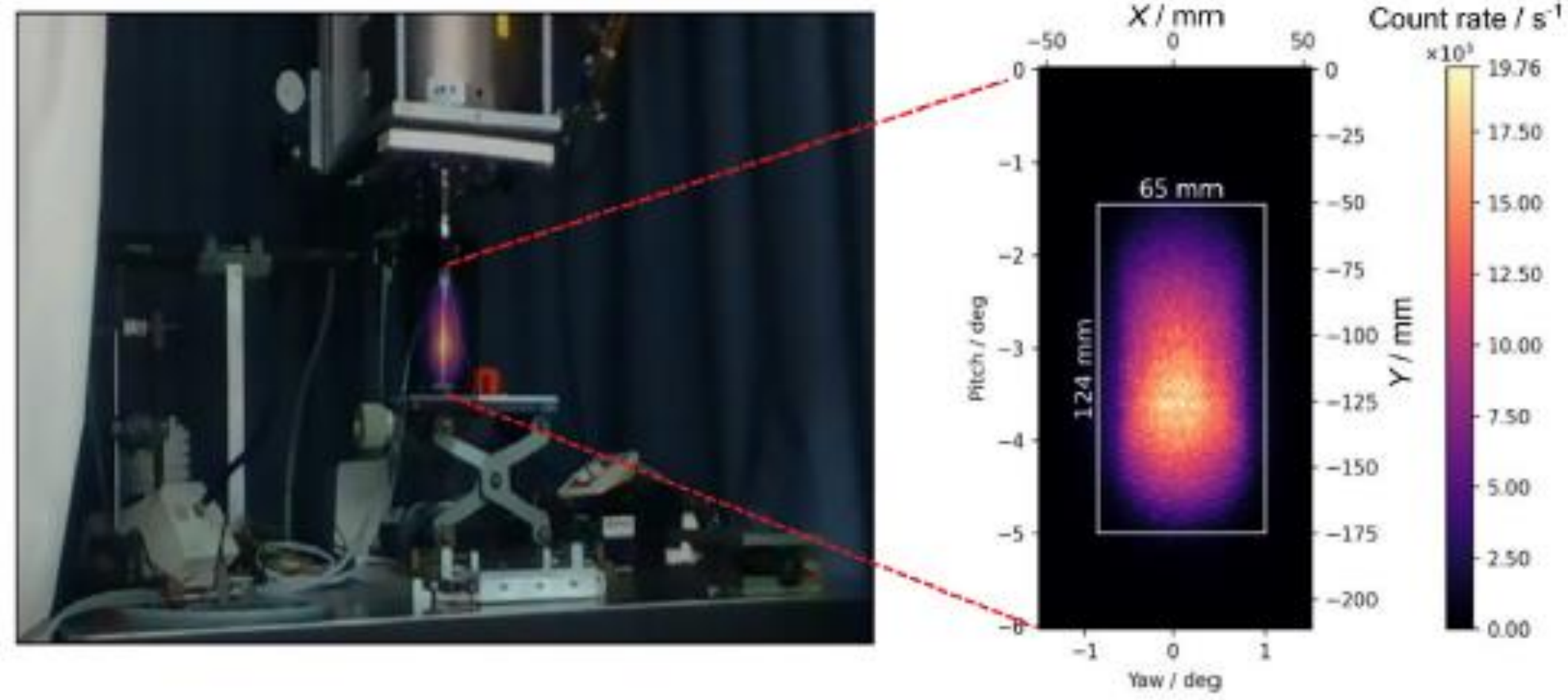


Fig. 8. UV-C radioluminescence image of 8.3 MeV alpha particles exiting the PIAF and stopping in the nitrogen filled quartz cuvette. This image is shown for illustrative purposes to demonstrate the mapping capability of the UVFS lens system shown in Fig. 3(a) and has been measured at an alpha particle rate higher than $5 \times 10^7 \text{ s}^{-1}$, which is above the counting capacity of the online microbeam monitoring system. The area around the quartz cuvette where the accelerated alpha particles were stopped has been scanned with the UVFS system from a distance of 2 m. The radioluminescence image has been superimposed on a conventional photograph, with the coordinates of both images correlated by ray tracing.

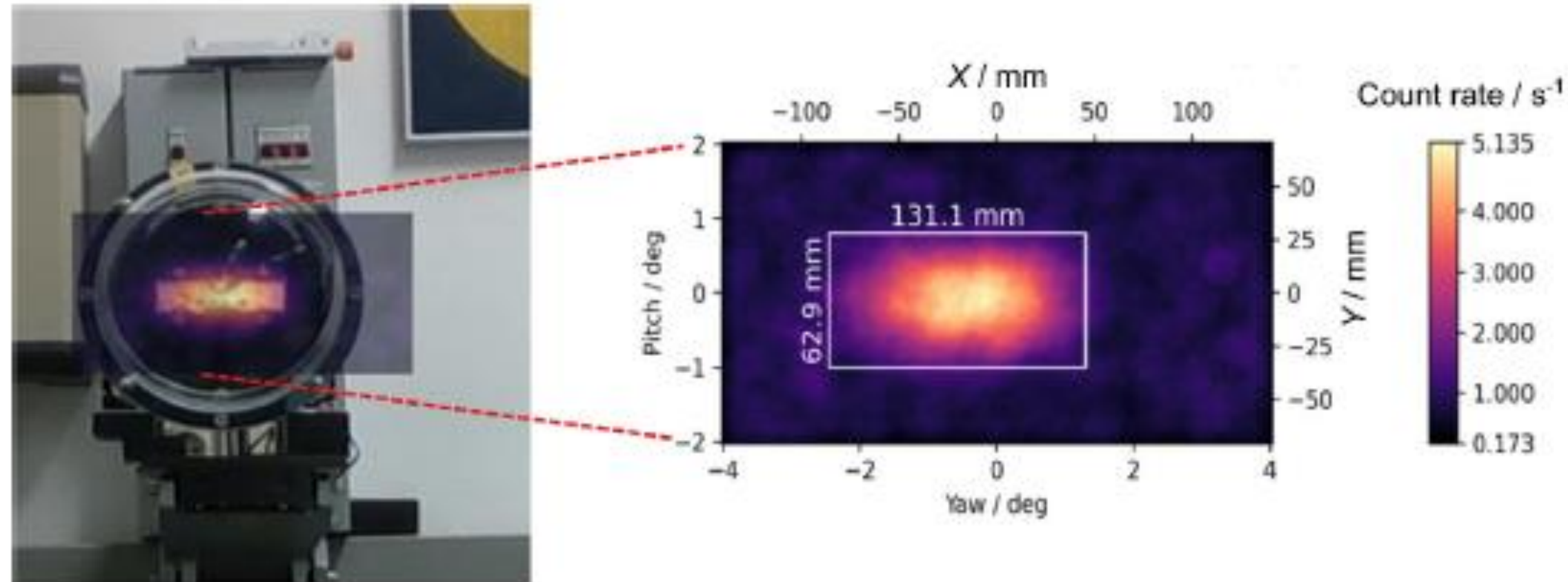


Fig. 9. UV-C radioluminescence image of the ^{241}Am source [cf. Fig. 4(b)]. The radioluminescence image has been obtained by scanning the area around the sample with the UVFS system from a distance of 2 m with a 2 s counting time per scan pixel. The radioluminescence image has been superimposed on a conventional photograph, with the coordinates of both images correlated by ray tracing.

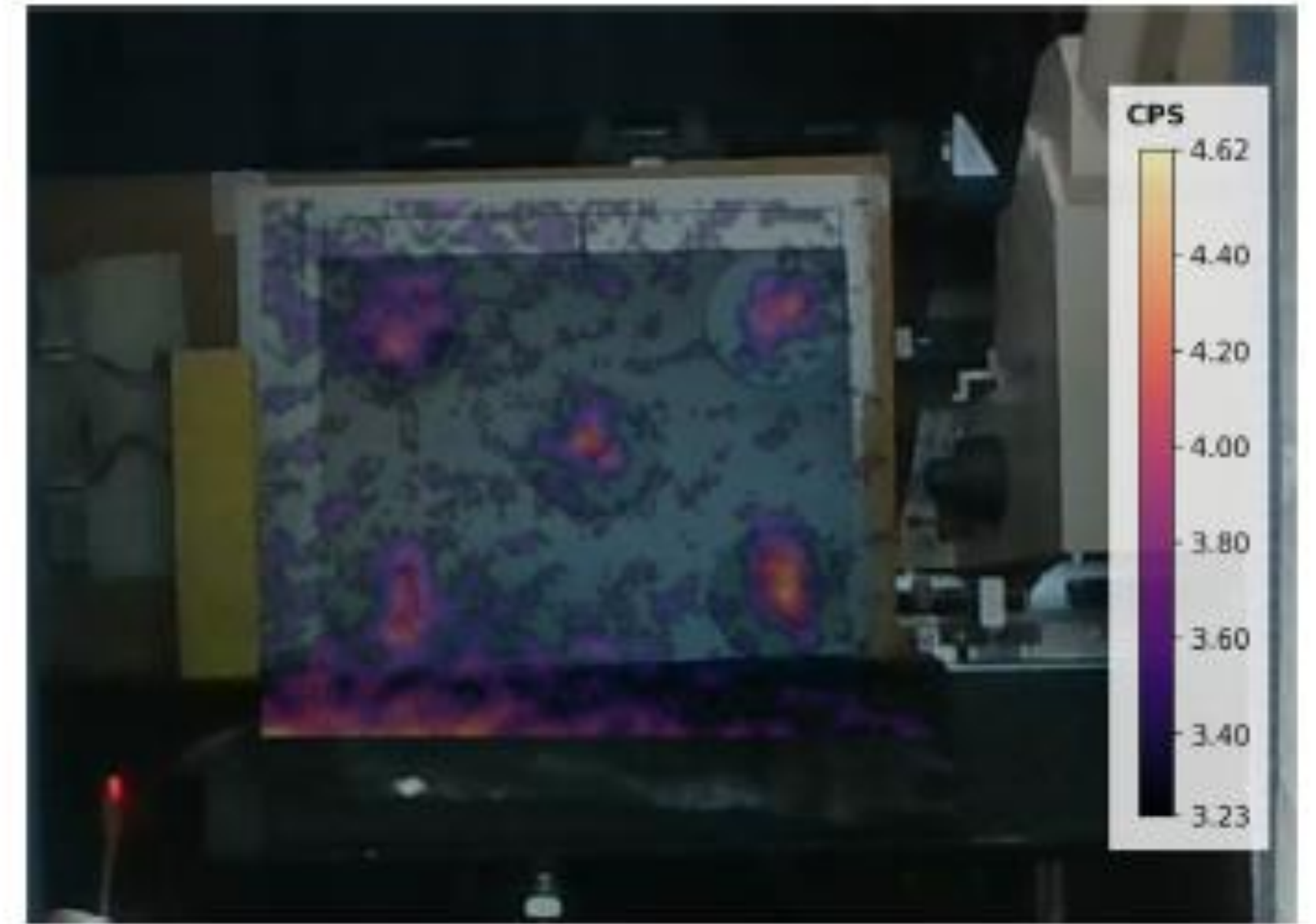


Fig. 10. UV-A radioluminescence image of the pitchblende mineral samples shown in Fig. 4(c) overlaid with the conventional image. The image has been obtained by scanning the area around the source panel with a UVFS system from 2 m.

Steps of the calibration procedure of the radioluminescence detectors: determination of the sensitivity of the measuring system (240 mm UV fused silica lens-based) with standard ^{210}Po and ^{239}Pu alpha sources

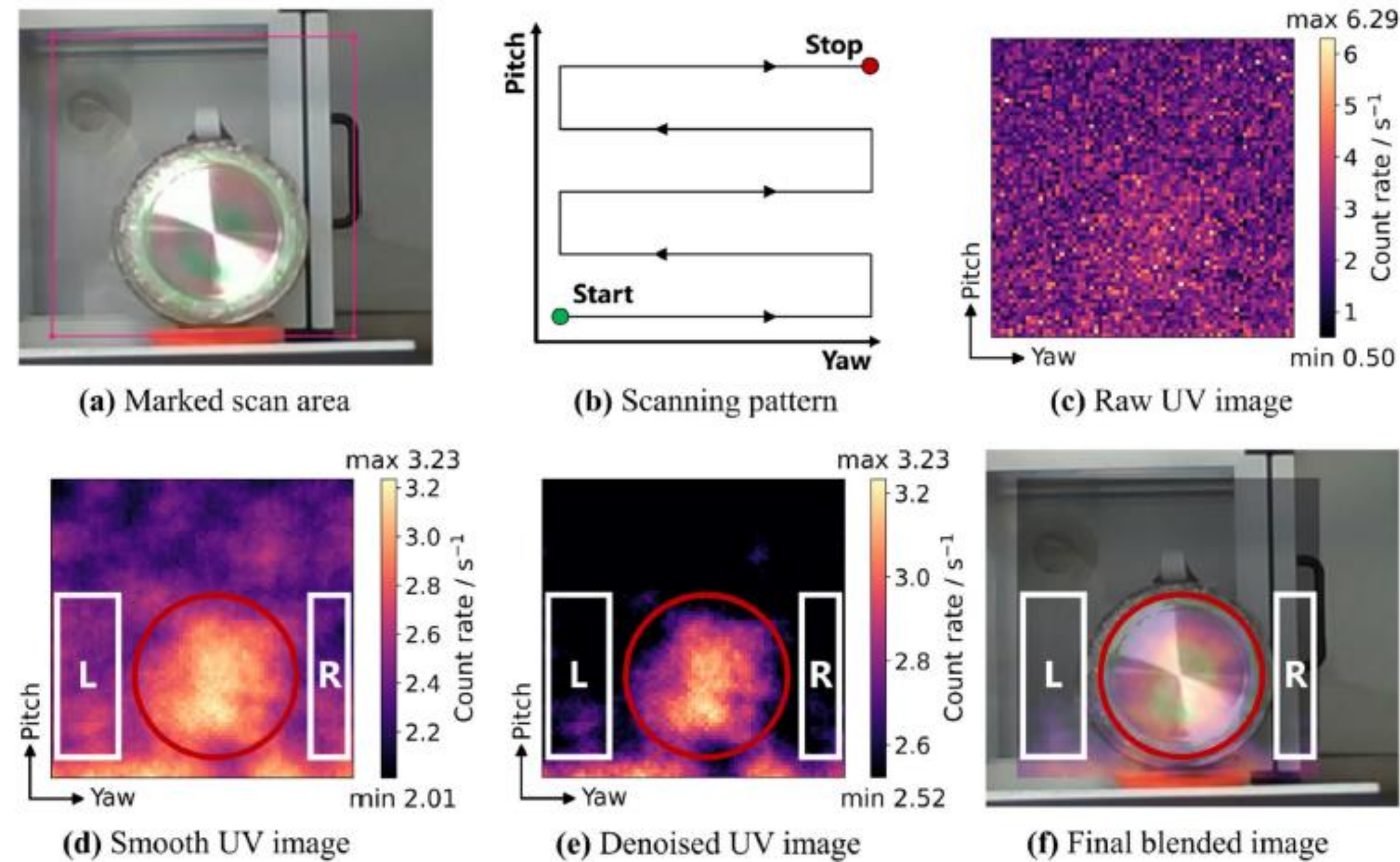


Fig. 4 The radioluminescence mapping procedure of the 4.9 kBq ^{239}Pu source measured in air from a distance of 2 m. The depth camera RGBD image **a** is used to select the scanning extent in pitch and yaw axes. The raw UV image **c** is smoothed using an averaging filter with a kernel size of 11 pixels. The smooth image **d** is then used to establish the signal and background domains: the source is outlined in

red, and the background area (white) is selected according to the scan pattern **b** of the detector. The smooth data is further denoised through thresholding determined by the background signal, and the processed image **e** is superimposed onto the color image **a** to produce the final radioluminescence image **f**

Table 2 Sensitivity coefficients for the used radioluminescence imaging system configurations derived with reference sources of ^{210}Po and ^{239}Pu

Detector configuration	Sensitivity ($\text{s}^{-1}\text{MBq}^{-1}$)	
	^{210}Po (vacuum chamber)	^{239}Pu (airtight chamber)
UV-A, air	660 ± 80	760 ± 100
UV-C, $\text{N}_2 + \text{NO}$ (saturated)	$123,000 \pm 14,000$	$63,000 \pm 7000$

The sensitivities are specified for a distance of 2 m between the source and the detector (lens)

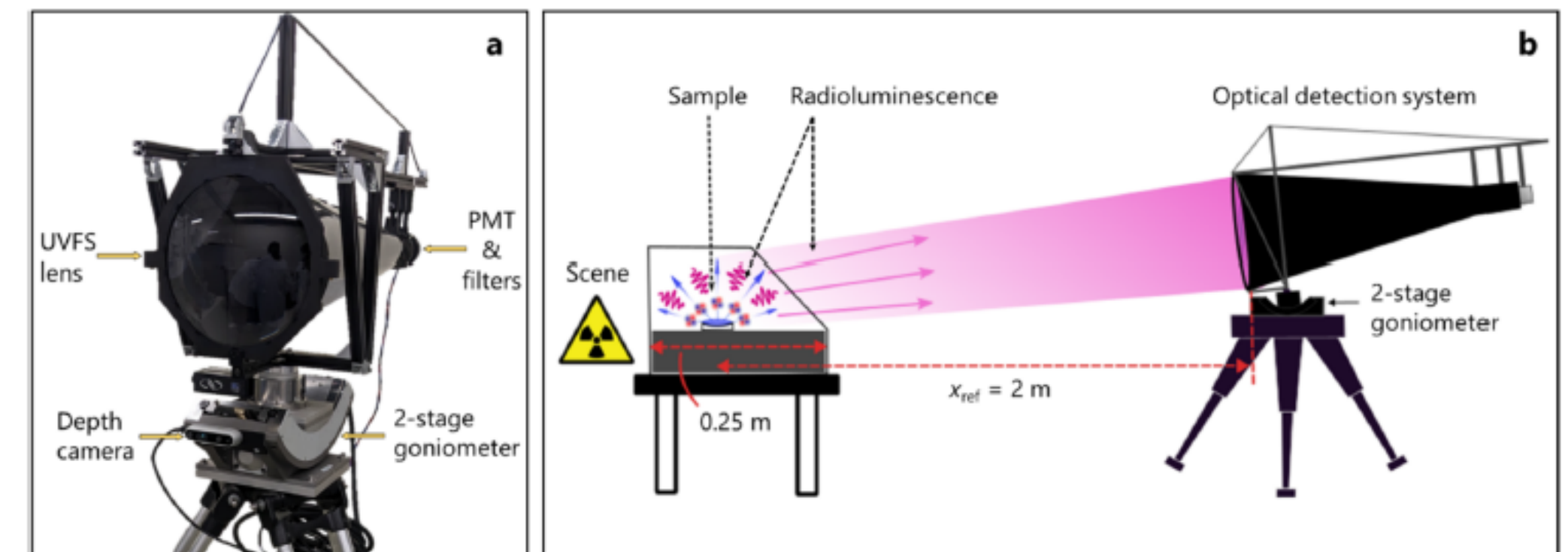


Fig. 2 **a** Radioluminescence imaging system built around a 240 mm diameter lens telescope. The system is mounted on a two-stage goniometer (Newport MBGM160PE and RVS80CC) and has an Intel RealSense D435 depth camera that captures an RGB color image of the scene. **b** Schematic diagram of radioluminescence mapping. The

samples placed in the airtight enclosure are scanned by the optical system located 2 m away from the sample. The 2D image of the scene is obtained by scanning the optical system with the two-stage goniometer in pitch and yaw directions

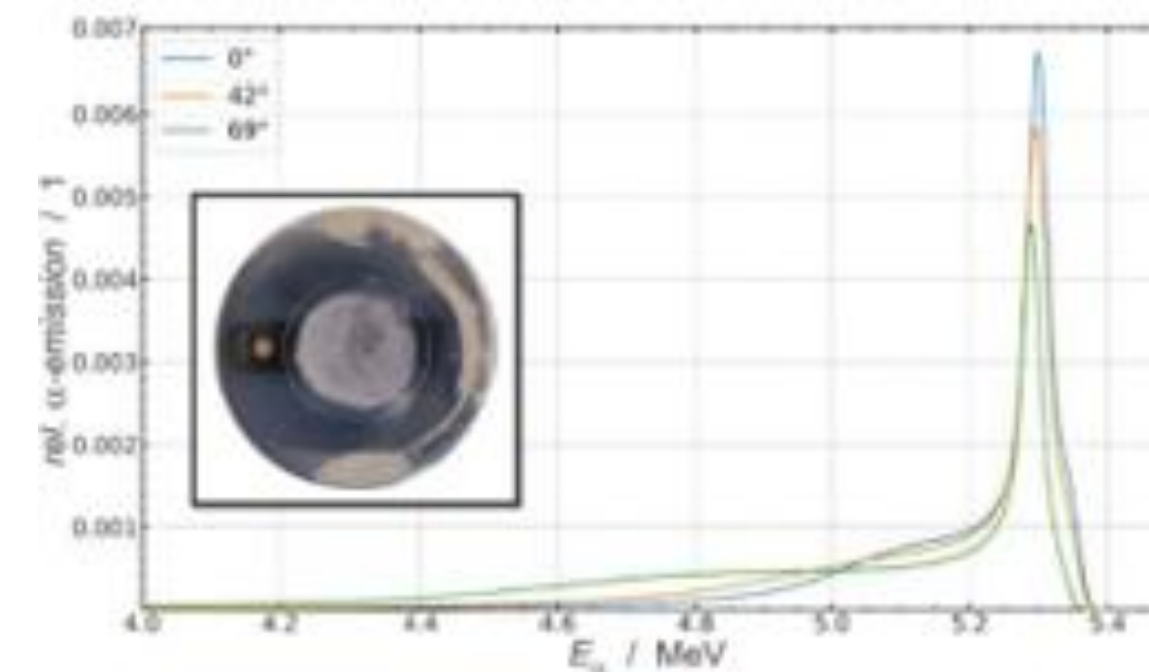


Fig. 3 Relative alpha emission of ^{210}Po activity standard measured with a 25 mm^2 silicon surface barrier detector behind a 3.2 mm aperture and a distance from the source surface of 15 mm. The spectra have been measured at 0° , 42° and 69° relative to the surface normal. The inset shows the ^{210}Po sample with a diameter of 12 mm (central part) deposited on the silver substrate.

The next step in the calibration procedure: preparation and characterisation environmental samples of urban and rural areas

A review of the triple-to-double coincidence ratio (TDCR) method for standardizing radionuclides

R. Broda*

Radioisotope Centre POLATOM, 05-400 Otwock-Świerk, Poland

Received 16 January 2003

Gravimetric injection of standard Am-241 solution into 2 each of sand, soil and leaves samples from 600 Bq to 11500 Bq activity environmental samples

The equilateral triangle design fits well with the 3-PMT design of the triple to-double coincidence ratio TDCR method. With this, the project defined surface activity.

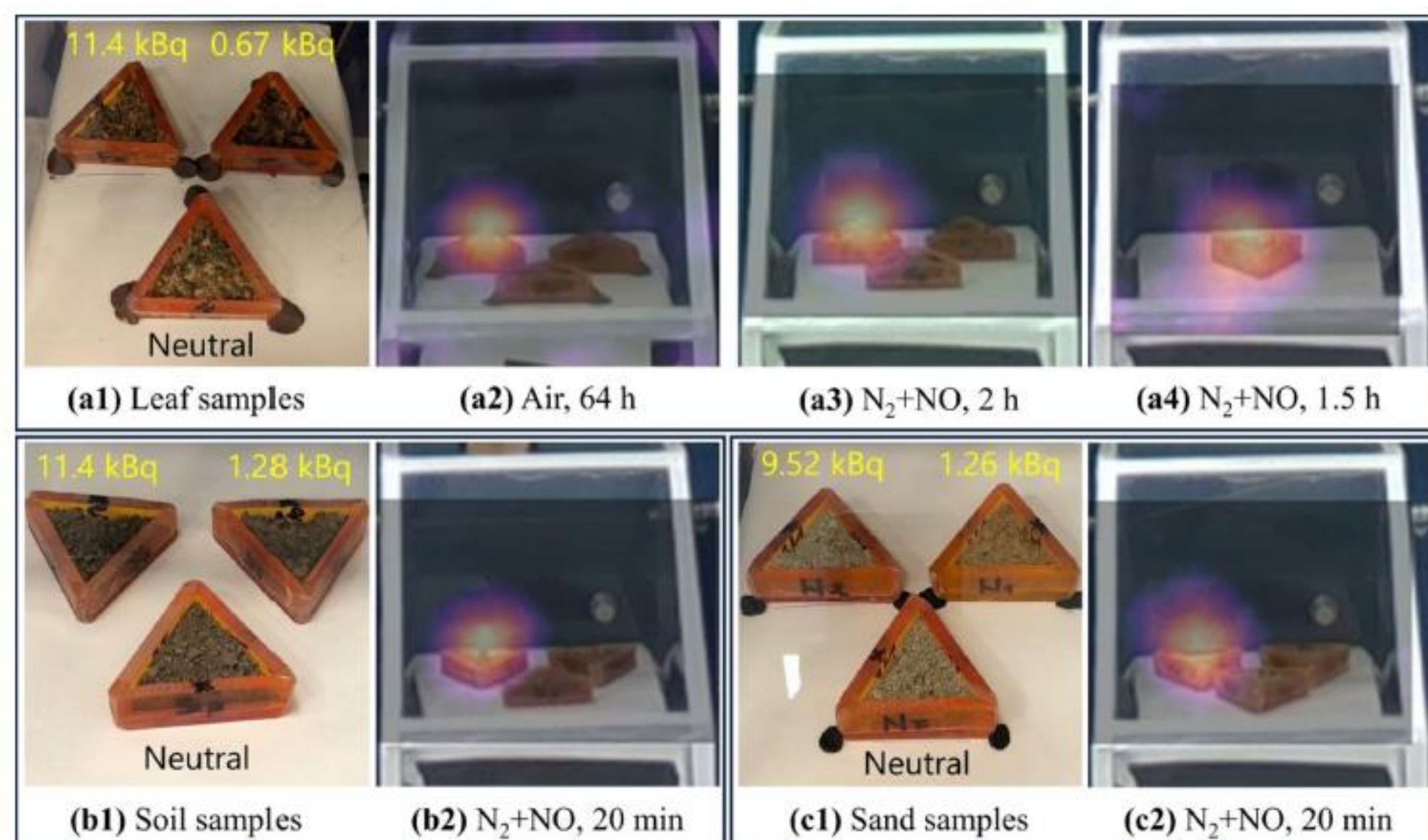


Fig. 5 Processed radioluminescence images of environmental samples of sand, soil, and leaves measured in an airtight chamber. Raw UV images are smoothed and denoised through thresholding before

overlapping with the corresponding color images. Image (a4) shows a separate scan of the lower activity leaf sample (0.67 kBq)

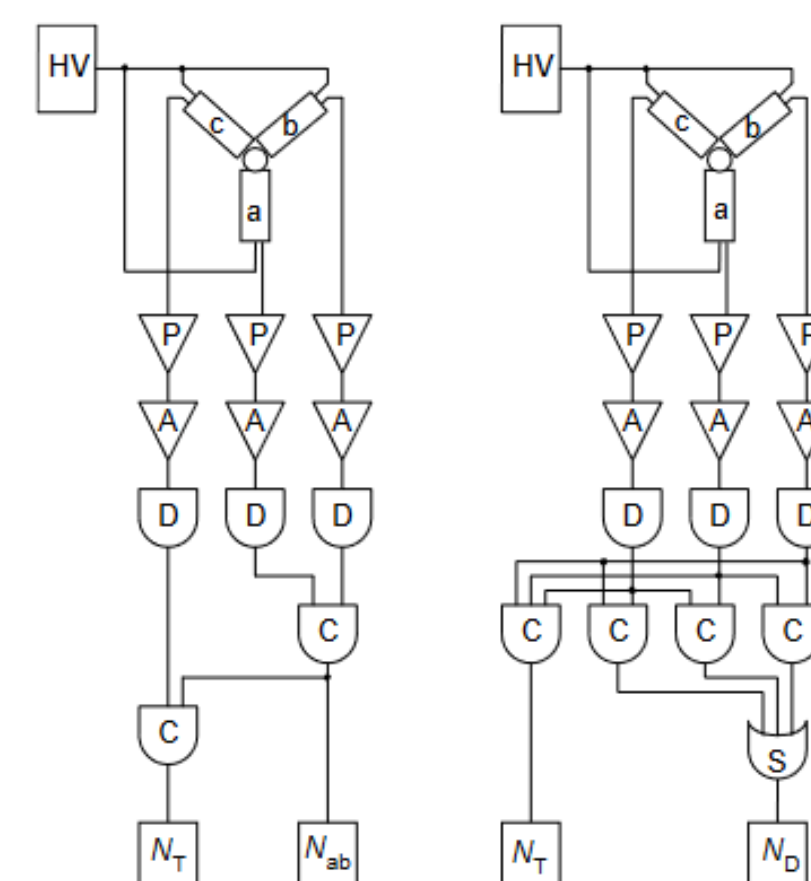


Fig. 1. A simplified block-diagram of the TDCR system with three-PMT detector. (a) Schwerdtel's device, (b) Pochwalski's device. HV—high voltage, P—preamplifier, A—amplifier, D—discriminator, C—coincidence gate (AND), S—summing gate (OR), N—counter.

In Pochwalski's system (Fig. 1b), the summing of the outputs of three double coincidence gates (N_T) and the counting of the sum of double coincidences (N_D) (including the triple coincidences) were the primary differences from Schwerdtel's system. The experimentally determined TDCR parameter, denoted by K

$$K = N_T / N_D$$

will always fall within an interval $0 \leq K \leq 1$, since the triple coincidence-counting rate, N_T , is always lower than the double coincidence-counting rate, N_D .

As the counting efficiency approaches unity

$$\phi \rightarrow 1,$$

the double- and triple- coincidence-counting rates will approach the disintegration rate of the source

$$N_T \rightarrow N_0,$$

$$N_D \rightarrow N_0$$

and the ratio K will also approach unity

$$K \rightarrow 1.$$

By extrapolating to $K = 1$, the values of the disintegration rate, N_0 , with counting efficiency $\phi = 1$ can be calculated. Thus the ratio K was found to be a very convenient experimental indicator of the counting efficiency, or quenching, of a given sample.

Table 3 Activities of environmental samples measured gravimetrically (deposited activity), and using TDCR and imaging techniques

Method	Sample activity (Bq)					
	Leaves 1	Soil 1	Sand 1	Leaves 2	Soil 2	Sand 2
Gravimetric	11,370 (110)	11,370 (110)	9510 (100)	669 (7)	1284 (13)	1258 (13)
TDCR (air)	1309 (13)	294 (3)	164.3 (18)	48 (3)	7.4 (4)	8.2 (6)
Imaging (air)	1390 (210)	290 (90)	—	—	—	—
Imaging (N ₂ + NO)	980 (110)	174 (25)	186 (26)	51 (7)	—	—

Optical techniques report the total surface activity

The second calibration: developing the low-photon flux radiance standards

Varying the slit width from 0.01 mm to 7.5 mm (fully open)

the alpha source activity can be simulated from $5.8 \cdot 10^4$ Bq to $8.3 \cdot 10^8$ Bq with the 340 nm UV-A radiance standard

and

from $2.9 \cdot 10^5$ Bq to $5.7 \cdot 10^9$ Bq with the 260 nm UV-C

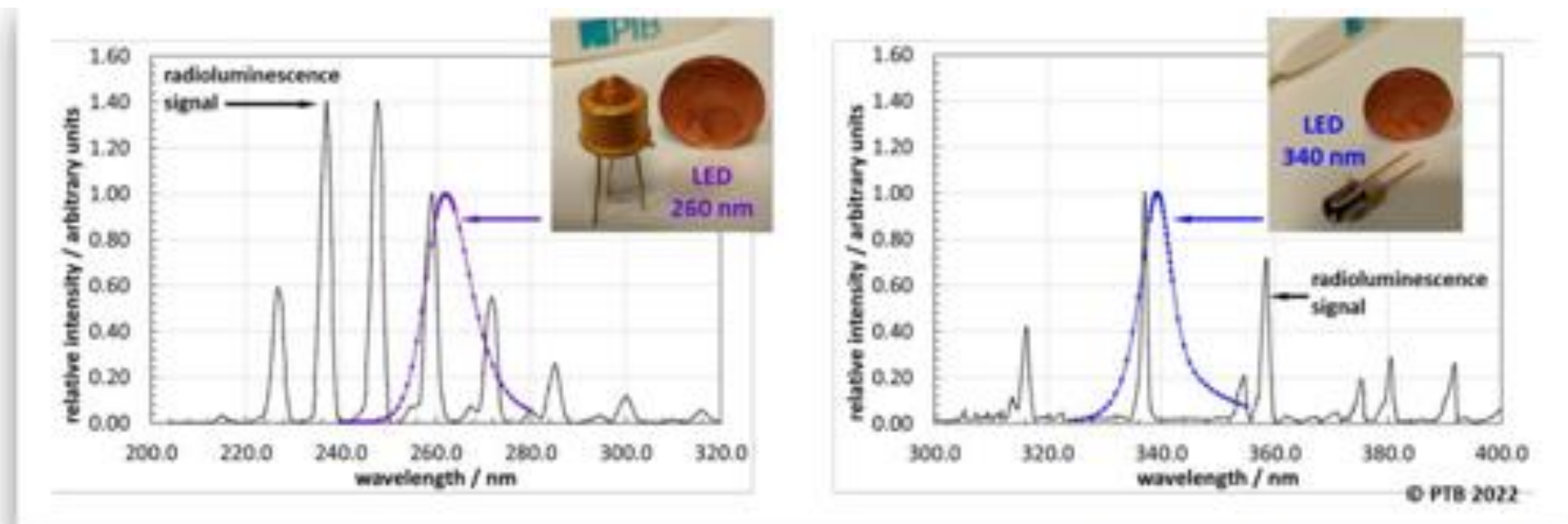


Figure 1: Radioluminescence optical radiation spectrum in the ultraviolet (UV) wavelength spectral range induced in the air by alpha-particles together with the emitted optical radiation by selected UV-LED radiation sources.

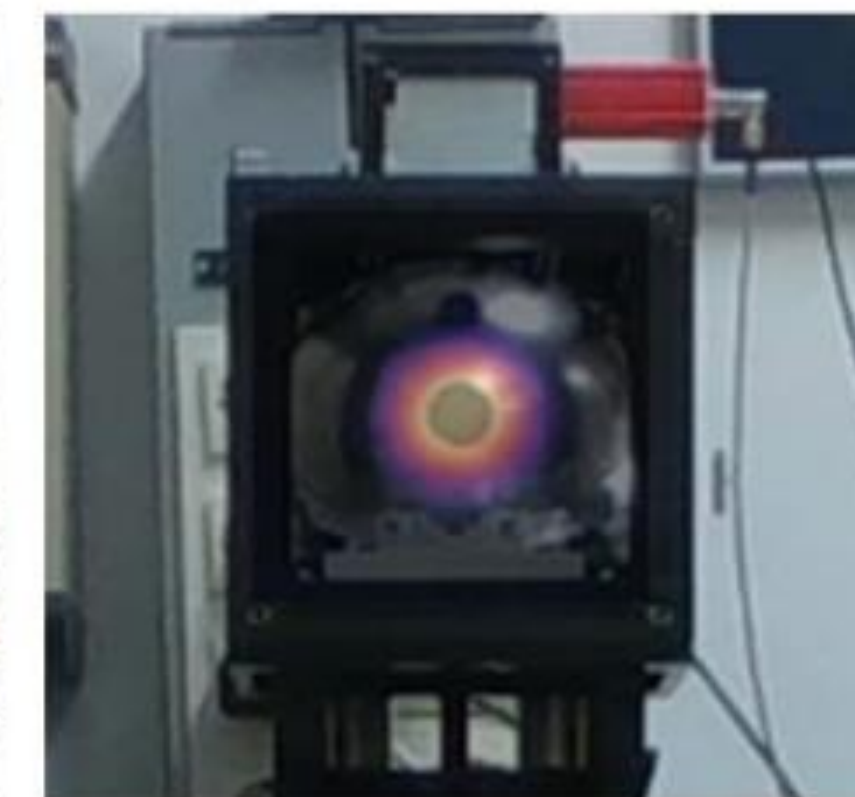
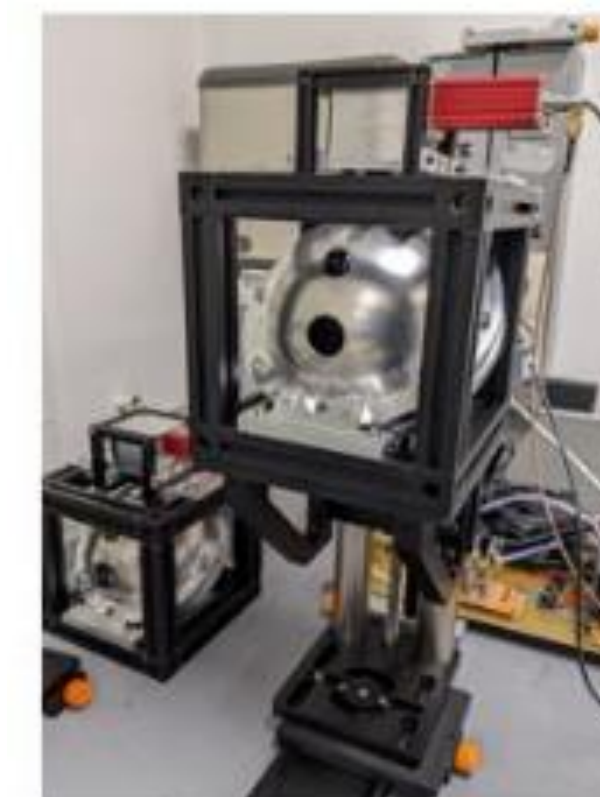
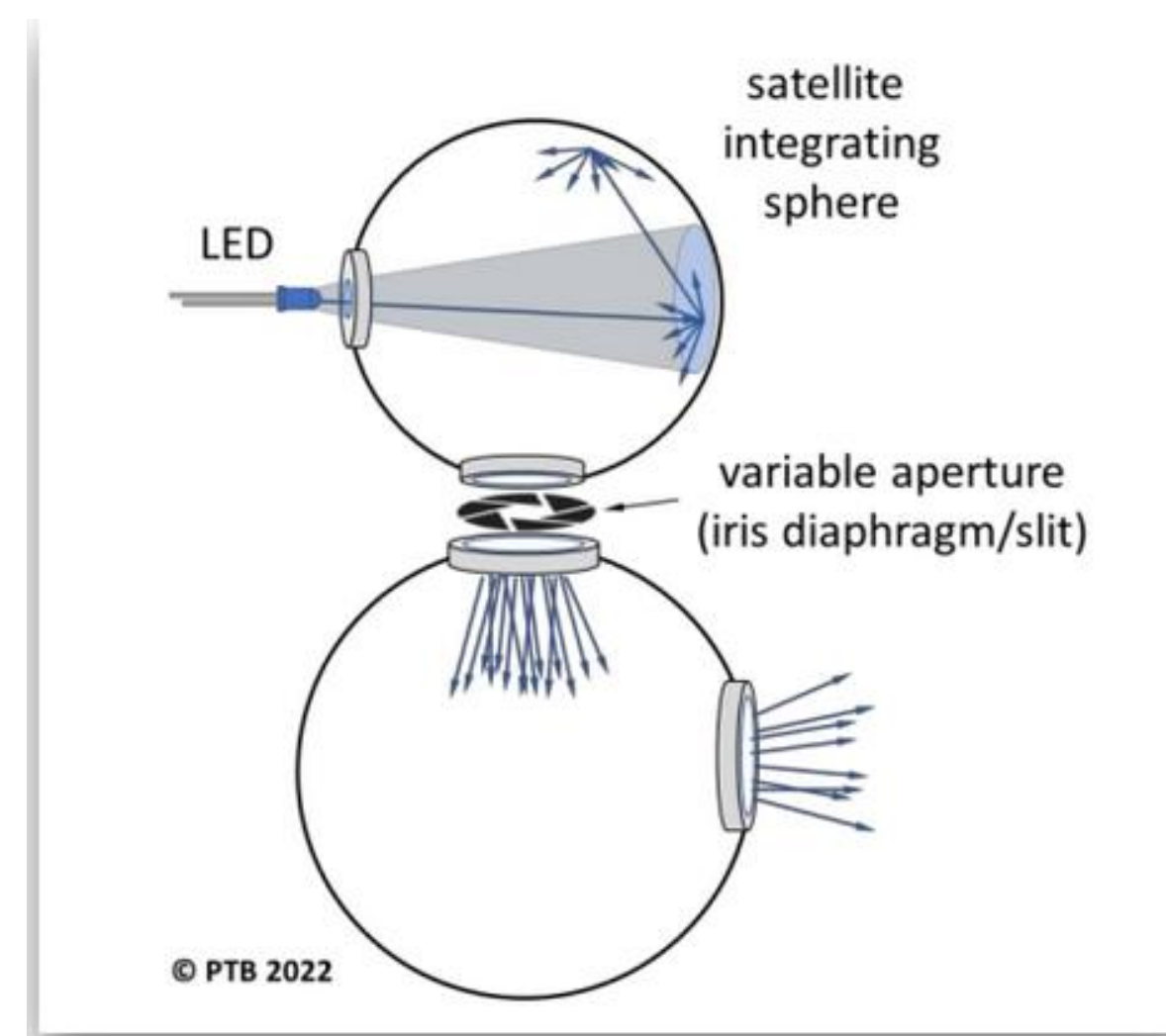
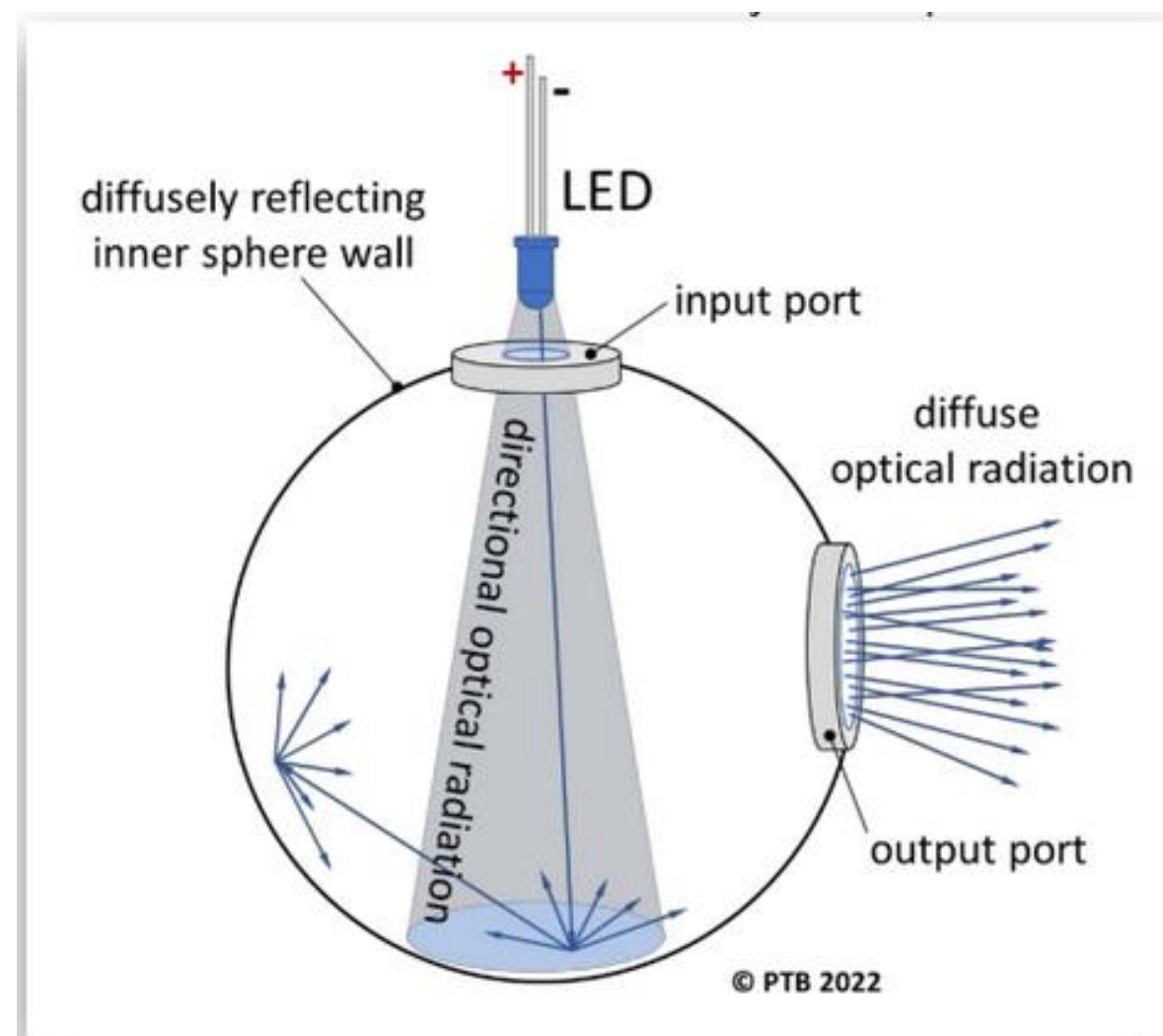


Fig. 7 (Left) Radiance standards based on integrating spheres, designed and developed by PTB with the help of BFKH. (Right) Mapping of simulated radioluminescence by the low-photon flux radiance standard at 260 nm measured by the UVFS detection system.

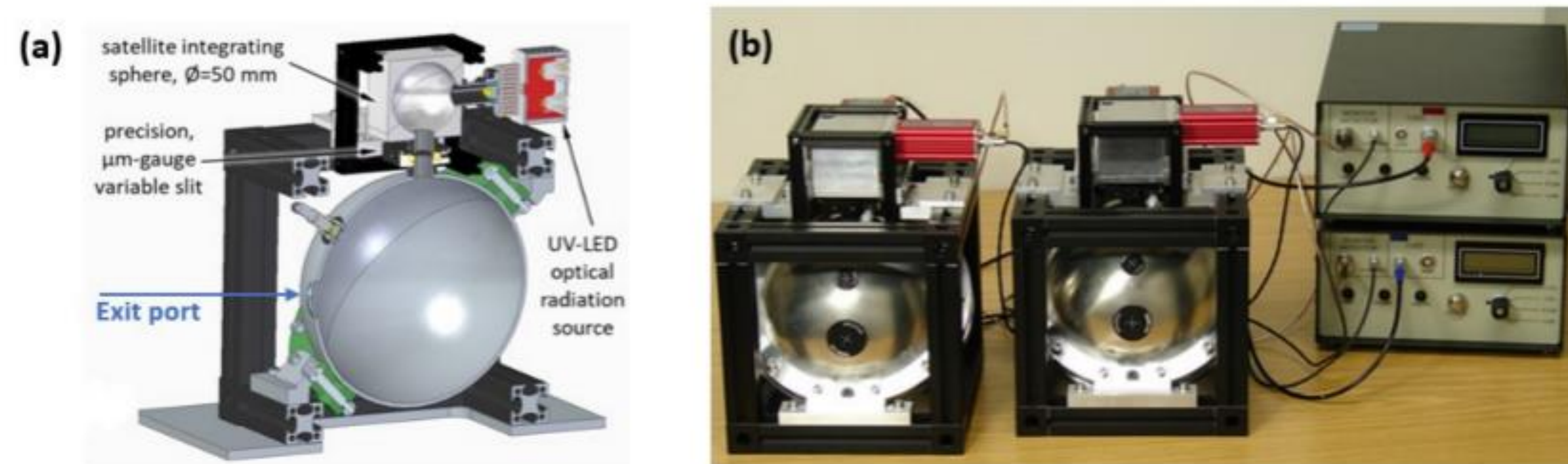


Figure 2: (a) Sectional schematic representation of the variable radiance, satellite integrating sphere-based configuration of the low photon flux UV radiance standard. (b) Realized prototypes of the variable low-photon flux UV-C (260 nm; left) and UV-A (340 nm; right) spectral range radiance standards for the calibration of the radioluminescence detector systems.

<https://oar.ptb.de/resources/show/10.7795/EMPIR.19ENV02.PA.20231027>

Krasniqi et al: A calibration methodology for the novel radioluminescence detector systems

Mapping of alpha contaminations in the environment using UAVs (Newsletter and Royo et al 2023.)

Royo, P.; Vargas, A.; Colls, T.G.; Saiz, D.; Pichel Carrera, J.; Rabago, D.; Duch, M.A.; Grossi, C.; Luchkov, M.; Dangendorf, V.; Krasniqi, F. Mapping of Alpha-Emitting Radionuclides in the Environment Using an Unmanned Aircraft System. Preprints 2023, 2023101698. <https://doi.org/10.20944/preprints202310.1698.v1>

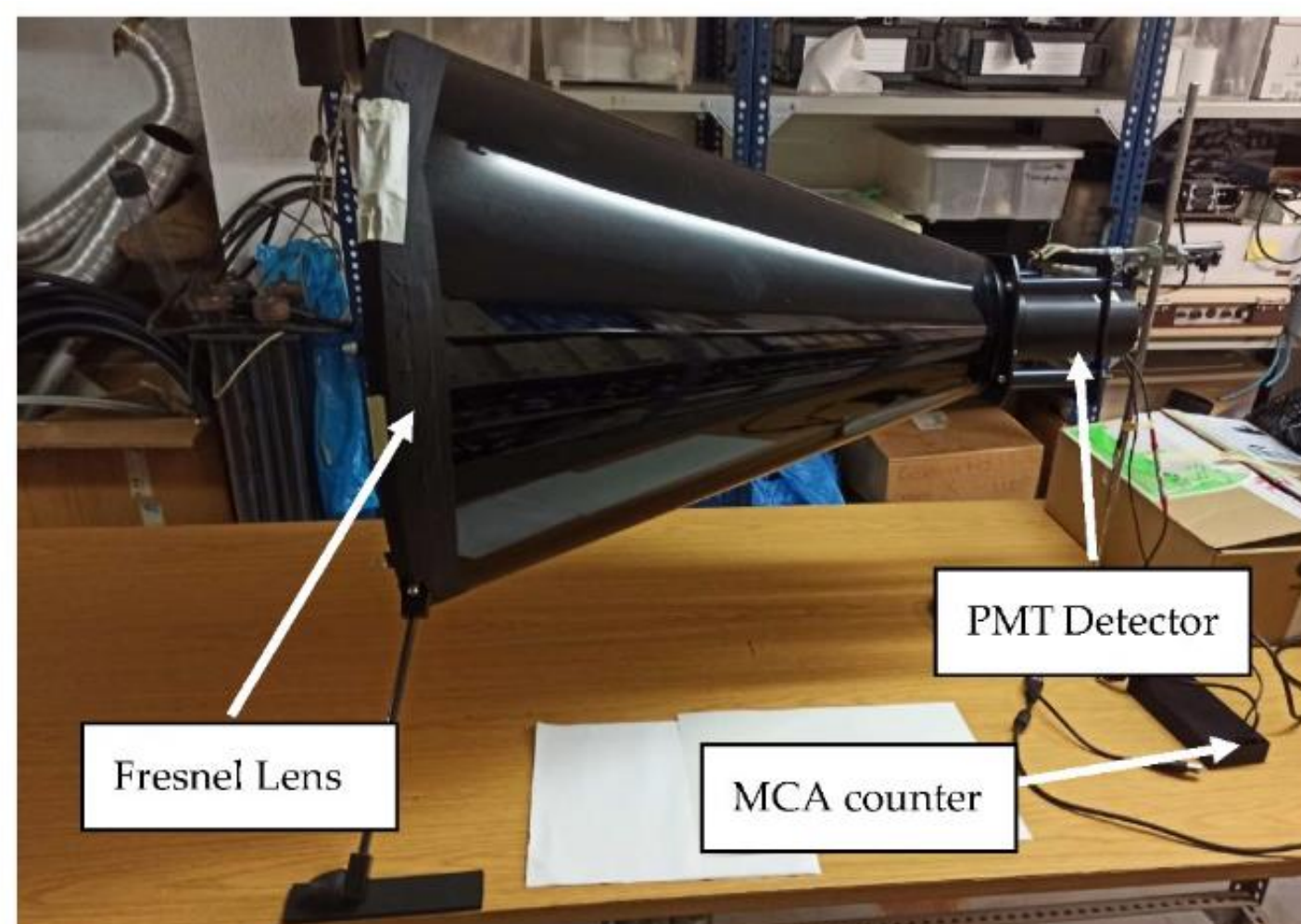


Figure 1. Fresnel lens optical system detector optimized for use with unmanned aircraft systems.

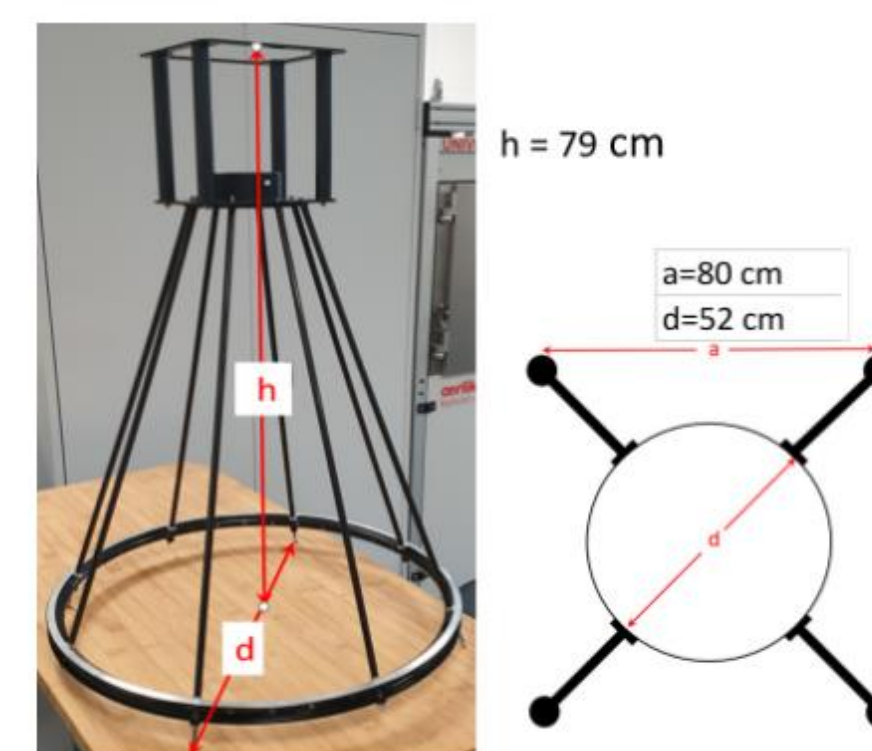


Figure 4. The Fresnel lens detector structure (left) and the landing legs add-on scheme (right).

Table 1 displays a summary of the weight of each UAS payload element and the sum of all components.

Table 1. Weight estimation of each component of the UAS payload.

Components	Weight (grams)
Detector Structure and Landing Gear	2591
PMT detector	408
GBS MCA527OEM + onboard computer + air-ground communications and wires	468
TOTAL	3467



Figure 5. Unmanned Aircraft System candidates for mounting the alpha detector system.



Figure 7. Radioluminescence detection system integrated with the DJI Matrice 600 Pro and ready to fly.

The LEDs and the 100 MBq ^{241}Am source purged with N_2+NO gas mixture have been used for the test flights with the Fresnel lens detector performed in the Drone Research Laboratory (DroneLab). The left side of Figure 10 shows the way the gas was administered to the americium source, and the right side of the figure shows how the count rate increases when the source is purged.

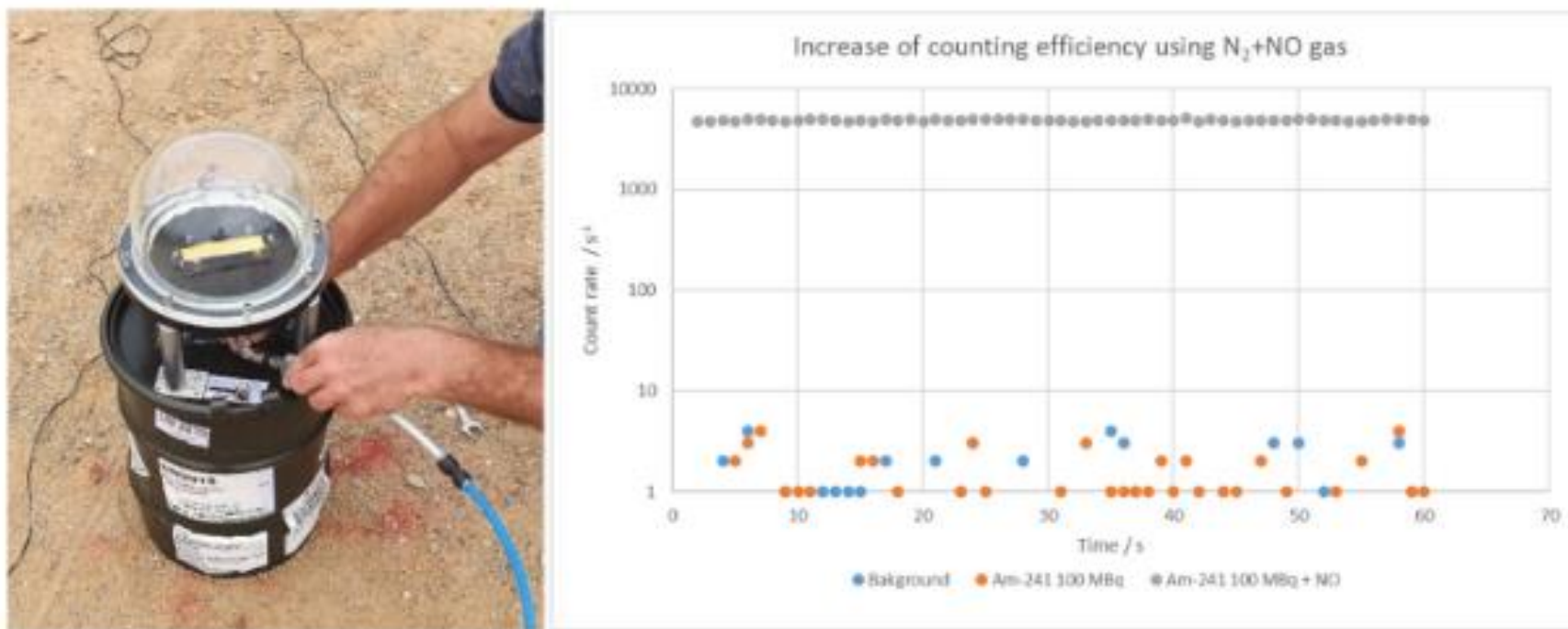


Figure 10. The N_2+NO (50 ppm) gas administration to the 100 MBq ^{241}Am source (left panel) and the corresponding increase in the detector's count rate (right panel).

„...Although alpha sources were used during the final flights, in many preliminary tests they were replaced by LED sources that simulate the UV emitted by the air Radioluminescence...”

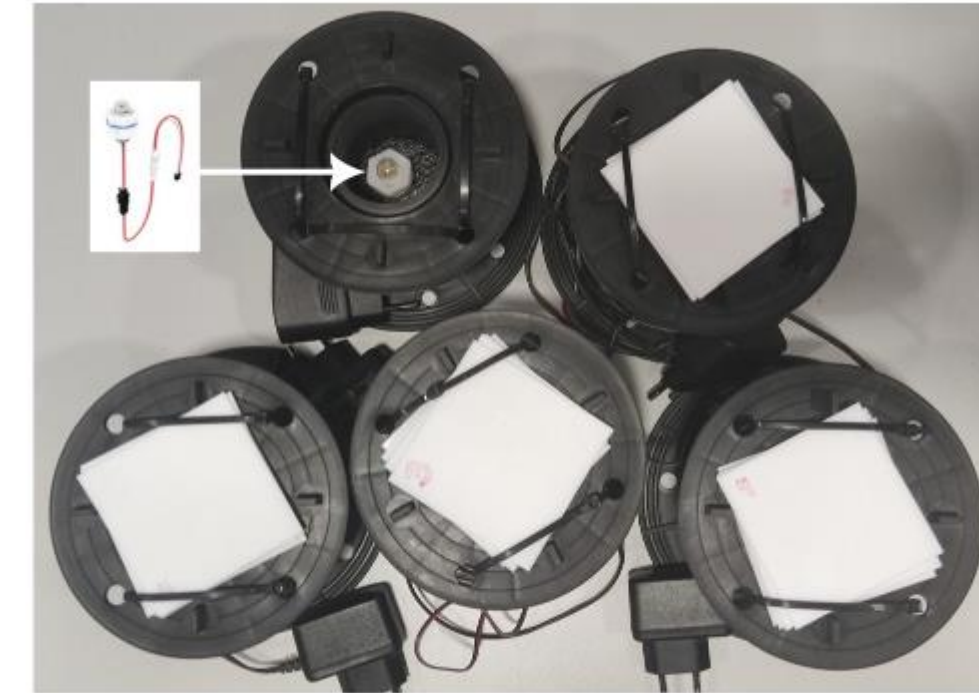
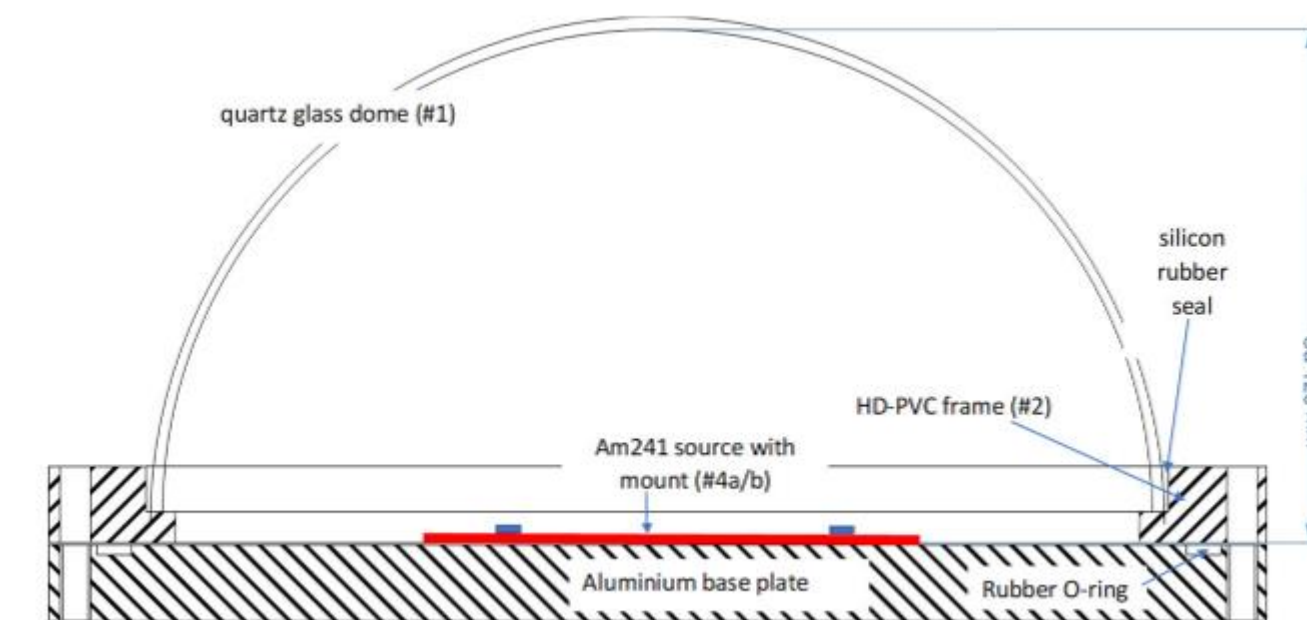


Figure 8. Five UV-C LEDs fabricated to simulate alpha sources with Teflon sheets on top.



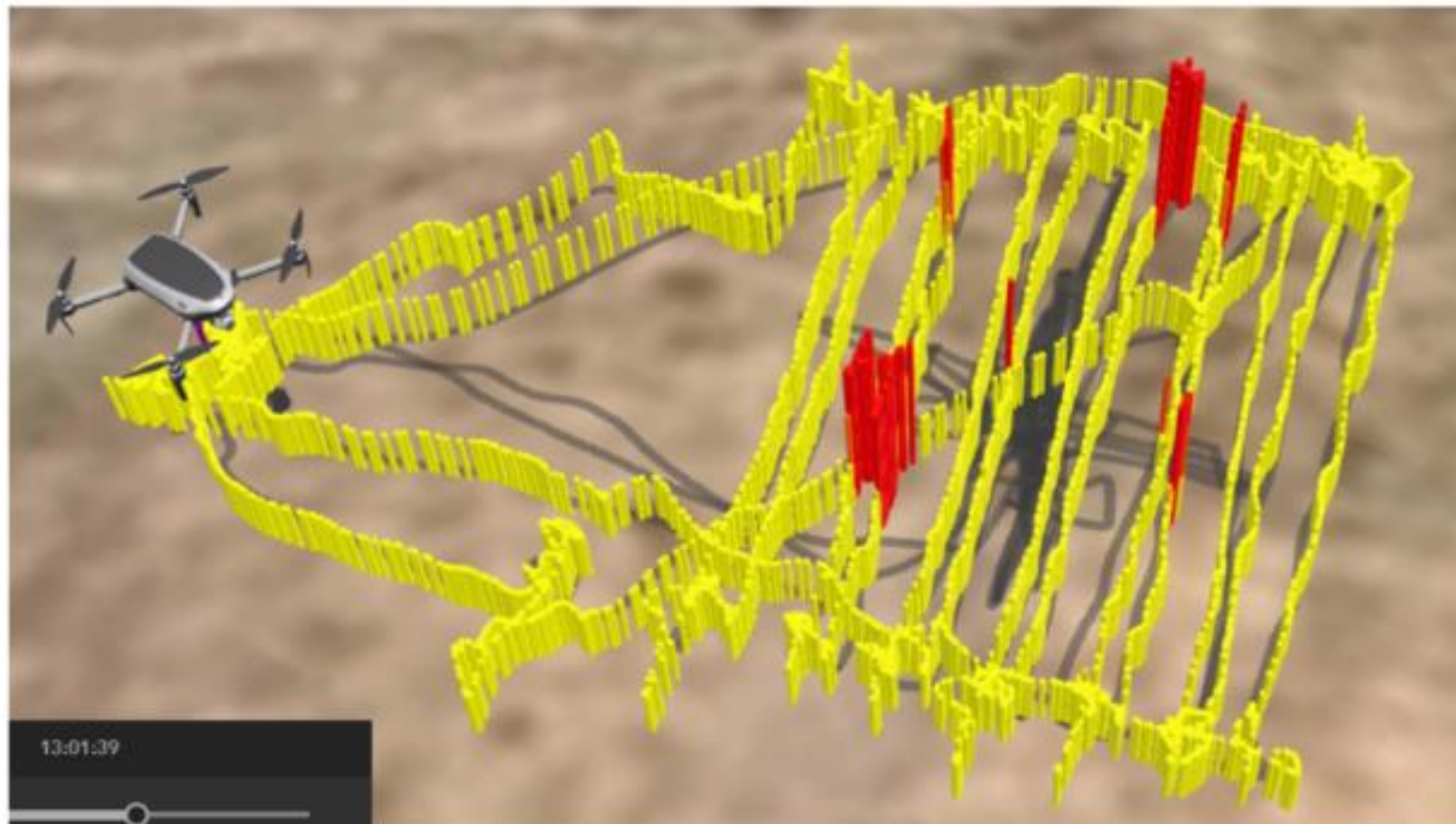


Figure 22. Flight performed with 5 LEDs and an americium source.

4. Conclusions

The main conclusion from the results presented in this manuscript is that alpha particles can be detected remotely from an unmanned aircraft system (UAS) by using optical detectors. To the extent of the authors' knowledge, this manifests the first time that alpha particles have been remotely detected from a UAS. The described prototype system, with certain operational improvements, can be used to assess contaminated areas without the need to put first responders at risk.

MATE's participation in the project



As a consortium partner MATE with collaboration IDEAS Science Ltd. (managing director Dr. Györgyi Bela)

- is currently developing on-line curriculum which can be used in BSc and MSc level university education,
- this curriculum can also be integrated into the training system of CBRN specialists, persons responsible for nuclear medicine technologies, radiation safety officers, environmental protection and waste management officers too.
- the topic of the project was simultaneously introduced into the MATE education system, and the educational experiences gained in teaching the related subject will also be taken into account in the development of the above-mentioned on-line course material.

(extracting from slide of 28th WORKSHOP ON ENERGY AND ENVIRONMENT, December 8-9, 2022, Gödöllő, Hungary)

-Partecipation in measuring campaign: Bucharest, IFIN-HH (Horia Hulubei National Institute, Romania, 2023. februar) with collaboration Crydet Ltd. (managing director Zoltán Csiki)

- dissemination at leader hungarian institutes: Wigner Research Center for Physics, ELI-ALPS Reseach Institute



High-quality technological solutions and consulting services for environmental and security problems.



Manufacture of scintillation crystals and detectors



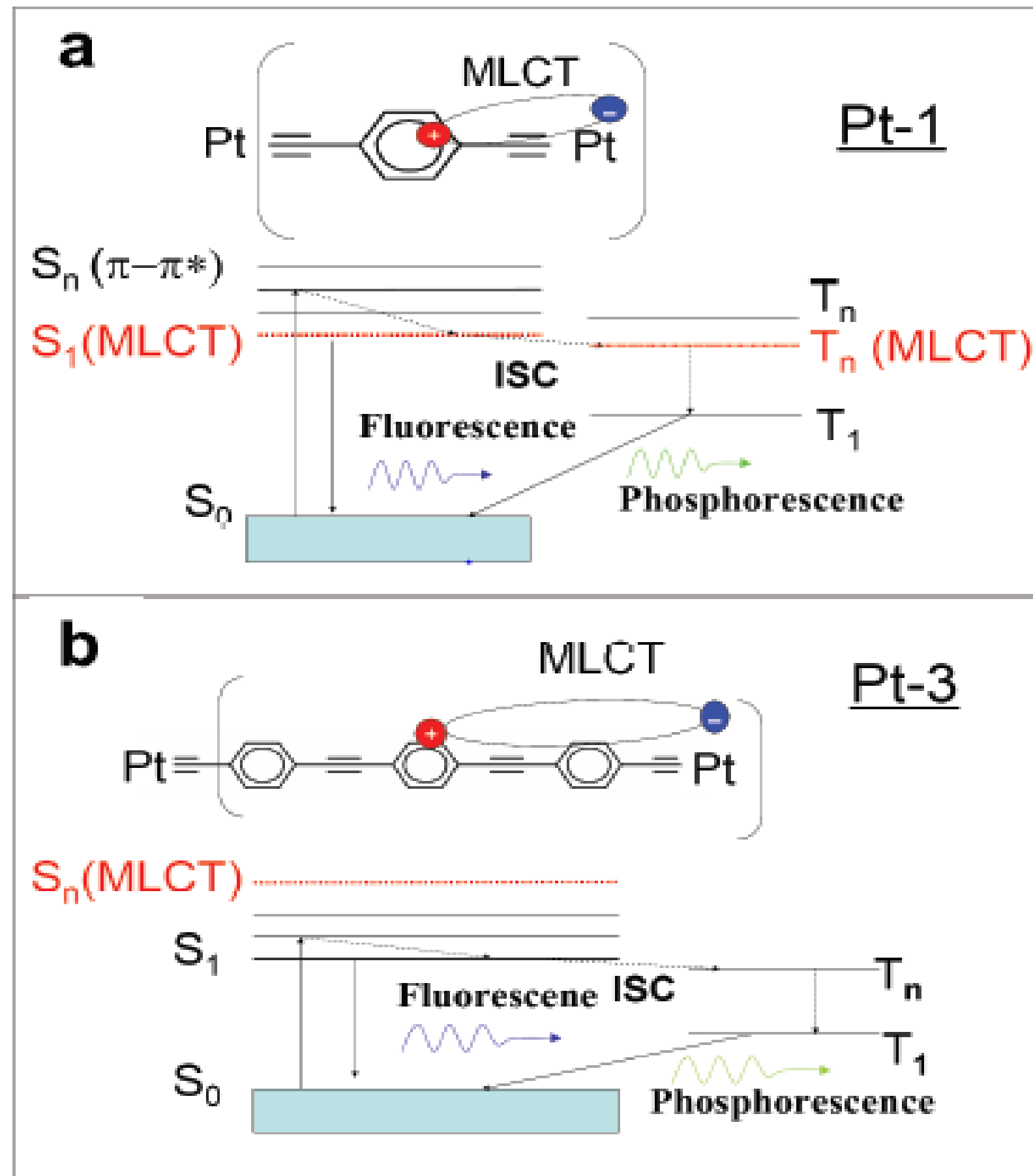
Deeper physical foundation on

- alpha radiation (penetration depth in mediums, Bragg-Kleeman –rule, linear energy transfer (LET), the Bragg-curve, computation in Bethe-Bloch formula, measuring methods by conventional detectors: GM-tubes,
- Molecular spectroscopy of diatomic molecules (rotational, vibrational states, infrared spectroscopy, Raman spectroscopy, electronic states associated with angular momentum, indicatings, electronic selection rules, the Franck-Condon principles, quantum mechanical basics, fluorescence and Raman scatterings
- The radioluminescence measuring methods, the so-called First Positive Group of Nitrogen and the Second Negative Group of N_2^+ ions, optical imaging systems, the lens-PMT, filter-CCD camera systems

The teaching of the subject provides an excellent opportunity to broaden physics education with which the principles of spectroscopy and molecular spectroscopy in particular, as well as the teaching the methods of the fundamentals of quantum mechanics, can become attractive and important for engineering students (extracting from slide of 28th WORKSHOP ON ENERGY AND ENVIRONMENT, December 8-9, 2022, Gödöllő, Hungary)

Thank You for your kind attention!

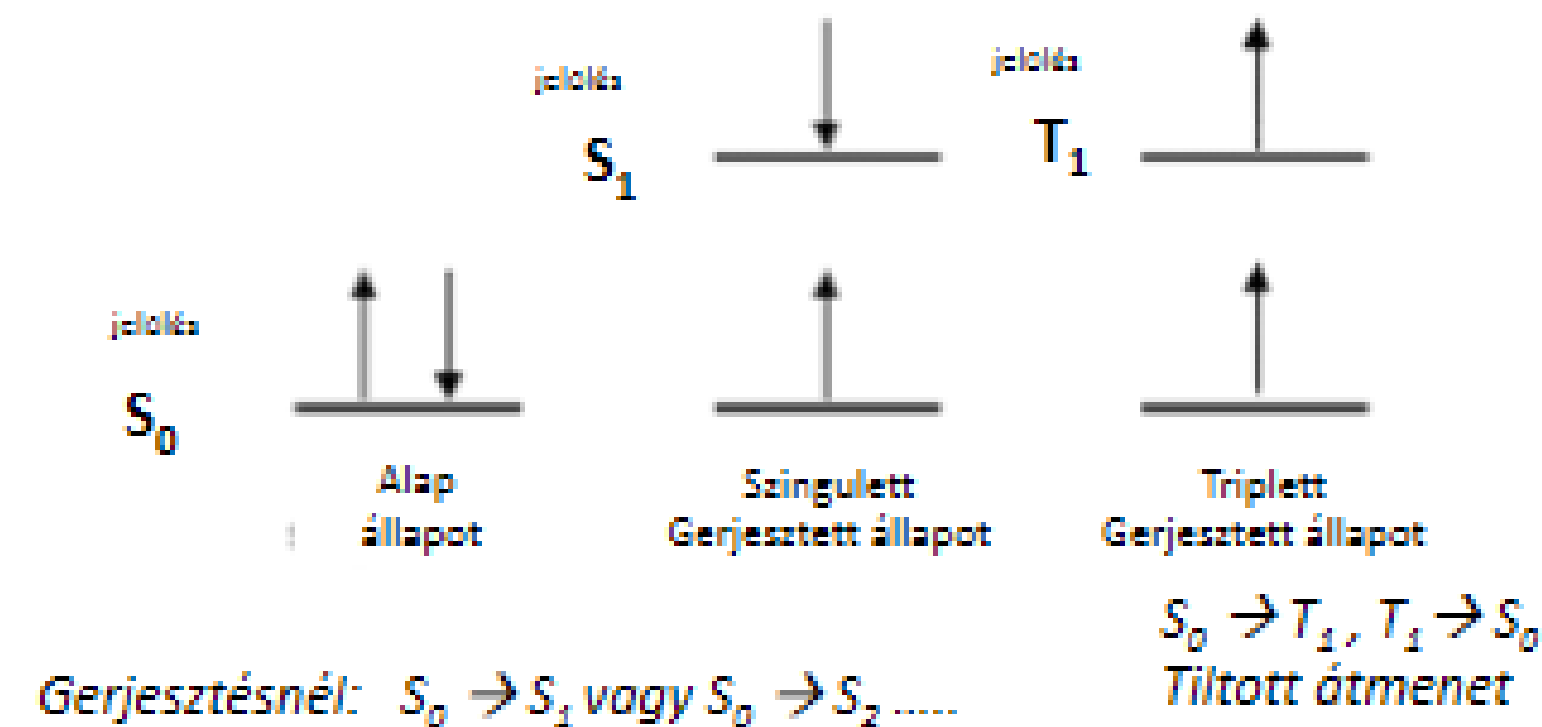
Hatásfoknövelés nehézfém atomnak a polimervázba ültetésével



Platina-polimer töltésátmeneti folyamat kétfajta polimerhordozó egység esetén a) két szomszédos Pt atom között egy ill. b) három fenilén gyűrű található. A fotogerjesztés után az elektron a Pt atom körül lokalizálódik, ahol spinje átbillen, míg a lyuk delokalizáltan marad a polimervázban (Átvéve: Sheng és társai, 2013)

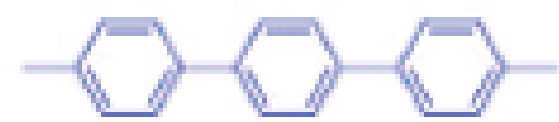
Szingulett állapot: a molekula összes elektronja párokban $\sum s_i = 0$
kompenzált spinű

Triplett állapot: egy elektron-pár van azonos spinnel $\sum s_i = 1$

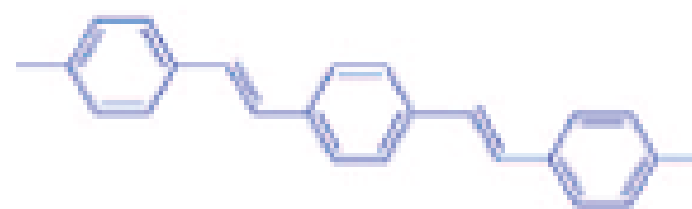


Lumineszcencia -Fényforrások
Fidy Judit Egyetemi tanár
2015, November 5

Anyag és módszer: a tanulmányozott napelemes polimertípusok



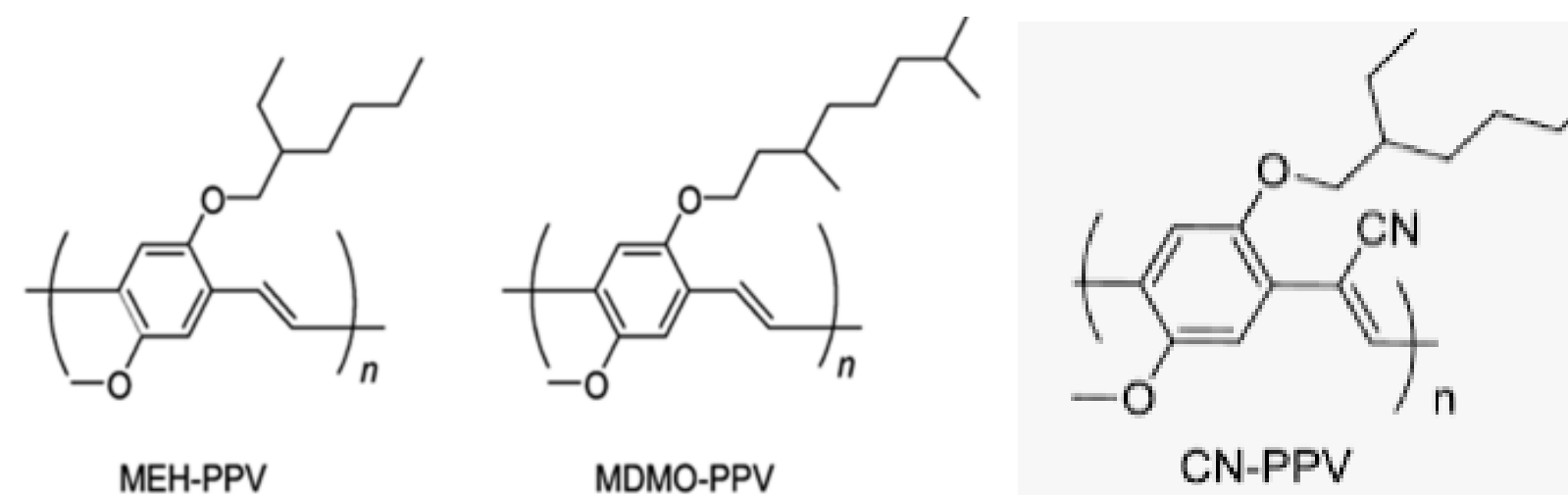
poli(*p*-fenilén)



poli(*p*-fenilénvinilén)



politiofén

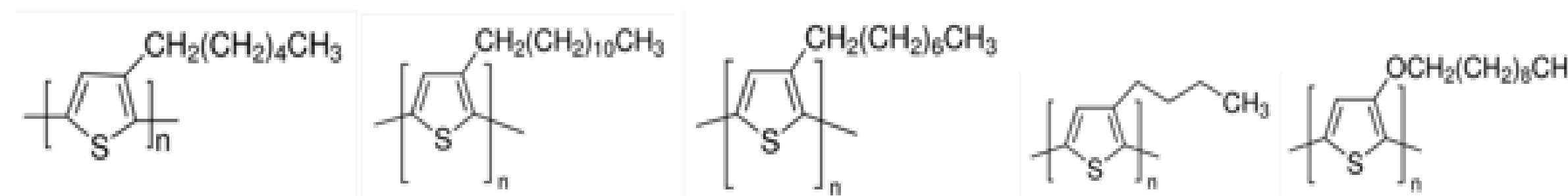


MEH-PPV (Poli [2-metoxi-5- (2-etilhexiloxi) -1,4-fenilén-vinilén]:

MDMO-PPV (poli [2-metoxi-5- (3', 7'-dimetil-oktiloxi) -1,4-fenilén-vinilén,

CN-PPV (Poli [5- (2-etilhexiloxi) -2-metoxi-ciano-tereftalilidén]):

A tanulmányozott polimertípusok aromás vázszerkezete (Cheng és társai, 2009)



A P3AT polimercsalád néhány tagjának szerkezeti képlete. Sorrendben: P3HT(poli(3-hexiltiofén-2,5- diyl)); P3DDT((poli(3-dodeciltiofén-2,5- diyl), P3OT(poli(3-oxiltiofén-2,5- diyl); P3BT ((poli(3-butiltiofén-2,5- diyl); Poly(3-deciloxtiofén -2,5-,diyl).

Kvantummechanikai modell:

Schrödinger- egyenlet: $\hat{H}\Psi = E\Psi$; \hat{H} := a rendszer (kristály) Hamilton operátora, valamennyi energiaoperátor tagot tartalmazza (elektronok, magok kinetikus energiaoperátorát, elektronok és magok páronkénti kölcsönhatási energiaoperátorát, elektronok-magok kölcsönhatása, külső tér energiaoperátorát)

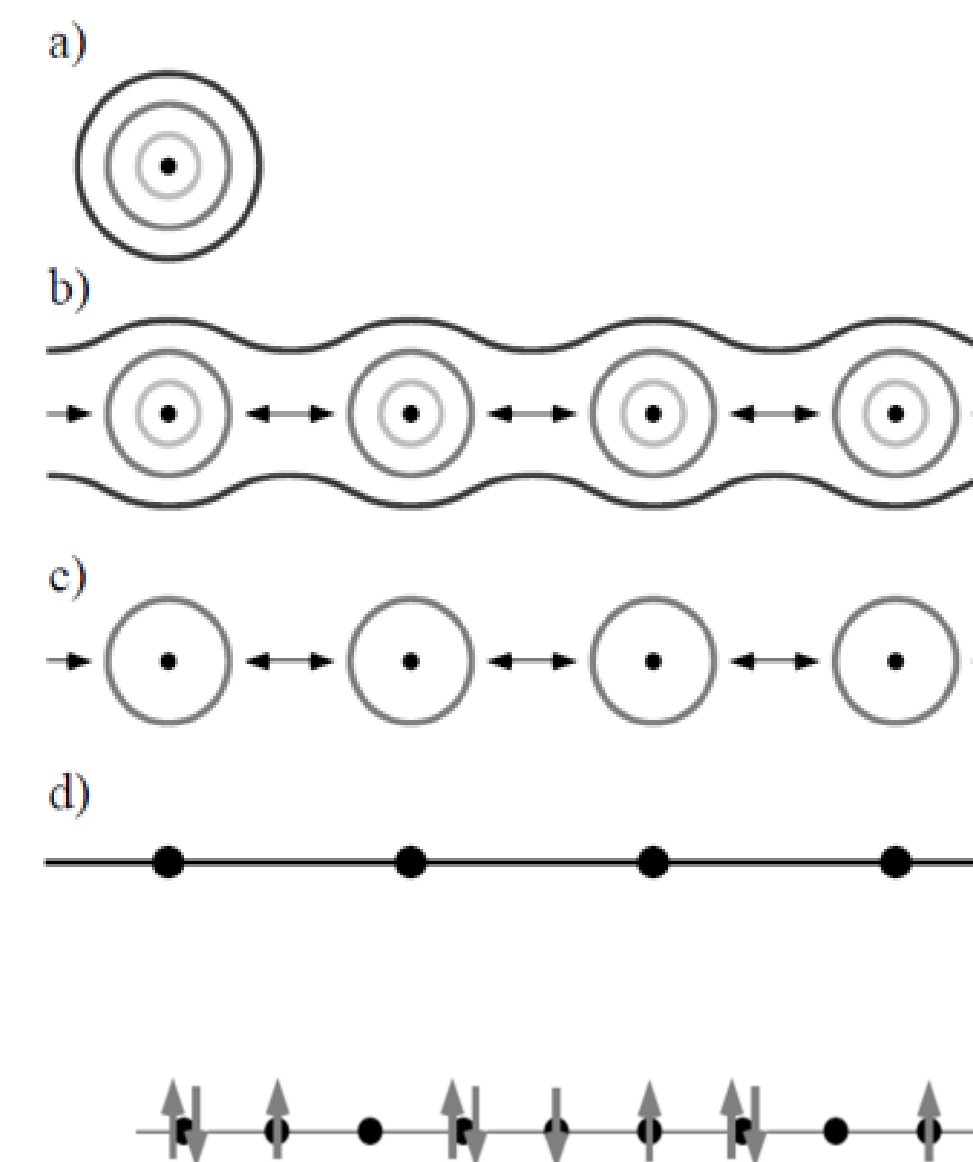
Elvileg sincsen módszer egymással kölcsönhatásban álló rendszerekre vonatkozó feladatok megoldására!

Adiabatikus közelítés: az elektronok hullámfüggvényére vonatkozó Schrödinger egyenletet egyrészeszkére vonatkozó egyenletre redukáljuk.

Szoros csatolású közelítés: atomokat közelítjük egymáshoz, az elektronállapot „nulladik” közelítése az izolált atom elektronállapota. Közelítéskor az atomi energiaszintekből sávok alakulnak ki.

Hubbard modell:

A Hubbard modell elnevezés Hubbard, Kanamori és Gutzwiller 1963-ban (és a további években) megjelent alapvető cikkeire utal (Hubbard, 1963, 1964, 1965, 1967, Kanamori, 1963, Gutzwiller, 1963) és azt a mély kérdést vizsgálja, hogy az ún. 3d- átmeneti fémeknél (Fe, Ni, Co) tapasztalt erős ferromágnességet, amely az elektronok spinjeinek nagyfokú rendezettségéből származik, okozhatja-e az elektronok közötti, spintől független Coulomb taszítás. (Tasaki, 1998, Mielke és Tasaki, 1993.).



$$\hat{H} = \hat{H}_{hop} + \hat{H}_U.$$

Az alapállapot energiája és hullámfüggvénye:

$$\hat{H}\Psi_g = E_g\Psi_g$$

$$\hat{H} = (\hat{H} - E_g\hat{1}) + E_g\hat{1} = \hat{P} + E_g\hat{1}$$

ahol:

\hat{P} pozitív szemidefinit, azaz sajátértékei nemnegatívak

Az alapállapot:

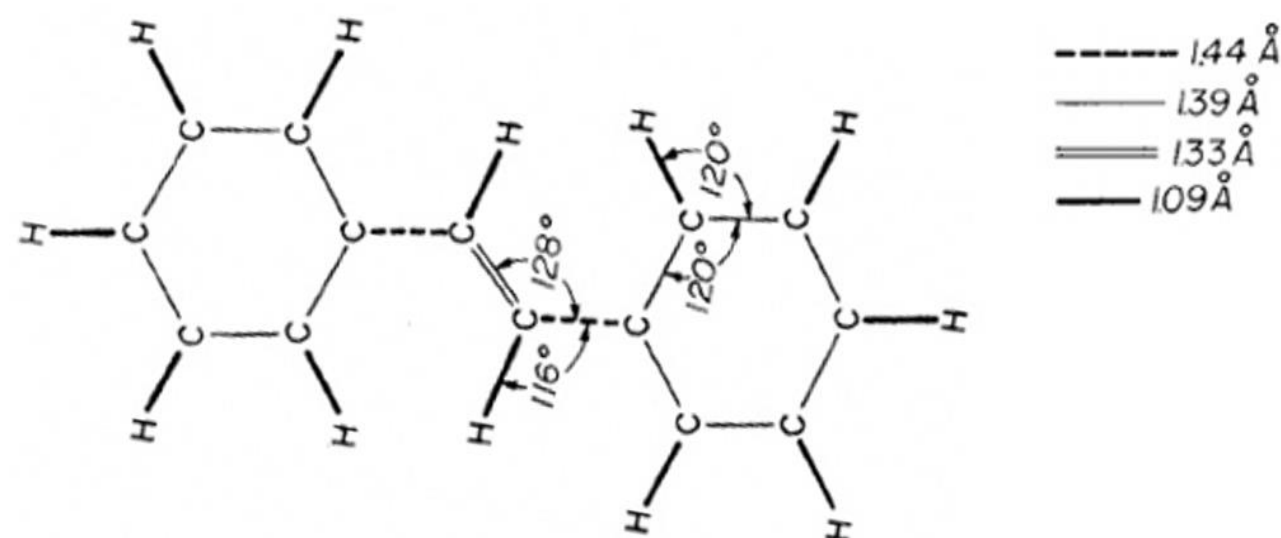
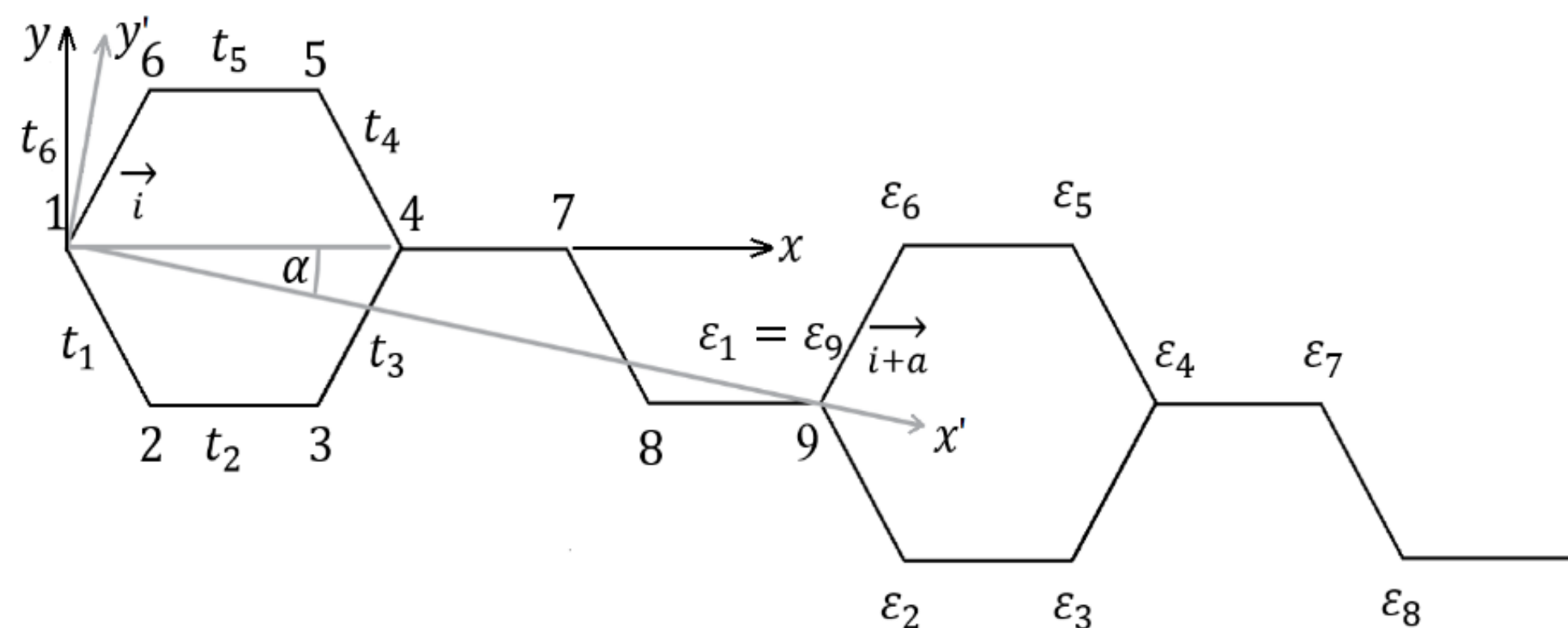
$$\hat{P}|\Psi_g\rangle = 0$$

$$\hat{P} : \hat{A}^\dagger\hat{A} \text{ alakú: } \{\hat{A}_\gamma, \hat{X}_j^\dagger\} = 0$$

$$\begin{aligned}\hat{P}_1|\Psi_g\rangle &= \left(\sum_\gamma \hat{A}_\gamma^\dagger\hat{A}_\gamma\right)\prod_j \hat{X}_j^\dagger|0\rangle = \sum_\gamma \left(\hat{A}_\gamma^\dagger\hat{A}_\gamma\prod_j \hat{X}_j^\dagger|0\rangle\right) \\ &= \sum_\gamma \hat{A}_\gamma^\dagger(-1)^{n_\gamma}\prod_j \hat{X}_j^\dagger\hat{A}_\gamma|0\rangle = 0\end{aligned}$$

$$\hat{A}\hat{A}^\dagger \text{ alakú: } \hat{A}_{i,\sigma,\alpha}^\dagger\hat{A}_{i,\sigma,\alpha} = 0$$

$$|\Psi_g\rangle = \left[\prod_\sigma \hat{G}_\sigma^\dagger\right]\hat{F}^\dagger|0\rangle,$$



A PPV származékok Hubbard modellje (fent) és geometriai szerkezete (lent: Granier és társai, 1986)

A rendszer Hamilton operátora:

$$\hat{H} = \hat{H}_0 + \hat{H}_U,$$

ahol

$$\hat{H}_0 = \sum_{\sigma} \sum_i \left\{ \left(\sum_{j=1}^5 t'_j \hat{c}_{i+r_{j+1,\sigma}}^{\dagger} \hat{c}_{i+r_{j,\sigma}} \right) + t'_6 \hat{c}_{i+r_{1,\sigma}}^{\dagger} \hat{c}_{i+r_{6,\sigma}} + t'_7 \hat{c}_{i+r_{7,\sigma}}^{\dagger} \hat{c}_{i+r_{4,\sigma}} \right. \\ \left. + t'_8 \hat{c}_{i+r_{8,\sigma}}^{\dagger} \hat{c}_{i+r_{7,\sigma}} + t'_9 \hat{c}_{i+r_{9,\sigma}}^{\dagger} \hat{c}_{i+r_{8,\sigma}} + H.c. + \sum_{k=1}^8 \varepsilon_k \hat{n}_{i+r_{k,\sigma}} \right\}$$

az ún. kinetikus tag, és

$$\hat{H}_U = \sum_i \sum_{n=1}^8 U_n \hat{n}_{i+r_{n,\uparrow}} \hat{n}_{i+r_{n,\downarrow}}$$

az ún. kölcsönhatási tag.

$$t'_k = t_k e^{i\gamma_{i,j}}, \quad \gamma_{i,j} = \left(\frac{2\pi}{\Phi_0} \right) \int_i^j \mathbf{A} \cdot d\mathbf{l} \text{ az ún. Peierls fázisfaktor;}$$

$$\int_i^j \mathbf{A} \cdot d\mathbf{l} = -\frac{1}{2} B (x_j - x_i) (y_j + y_i)$$

$$\mathbf{B} = (0; 0; -B);$$

$$A_x = -yB; \quad A_y = A_z = 0; \quad (\text{Landau -mérték})$$

$$\Phi_0 = h/e \quad \text{az ún. fluxuskvantum,}$$

Eredmények: PPV-származékok sáv szerkezete külső, állandó mágneses mezőben

Cél: a vinilén-lánc jelenléte hogyan befolyásolja a korábbi, polifenilén (PPP) láncokra kapott eredményeket (Trencsényi és társai, 2011)

Hamilton operátor \hat{H}_0 kinetikus tagját a \mathbf{k} -hullámszámvektor térbe kell transzformálnunk a $\hat{c}_{i+r_{n,\sigma}} = (1/\sqrt{N_C}) \sum_{\vec{k}} e^{-i\vec{k} \cdot (\vec{i} + \vec{r}_n)} c_{n,\vec{k},\sigma}$ Fourier transzformációnak megfelelően.

$$\hat{H}_0 = \sum_{\sigma, \vec{k}} C_{\vec{k},\sigma}^\dagger \tilde{M}_{\vec{k}} C_{\vec{k},\sigma},$$

$$C_{\vec{k},\sigma}^\dagger = (\hat{c}_{1,\vec{k},\sigma}^\dagger; \hat{c}_{2,\vec{k},\sigma}^\dagger; \dots; \hat{c}_{8,\vec{k},\sigma}^\dagger);$$

$$\tilde{M}_{\vec{k}} = \begin{pmatrix} m_{11} & \dots & m_{18} \\ \vdots & \ddots & \vdots \\ m_{81} & \dots & m_{88} \end{pmatrix},$$

a diagonálisok $(\epsilon_1; \epsilon_2; \epsilon_3; \epsilon_4; \epsilon_5; \epsilon_6; \epsilon_7; \epsilon_8)$.

A sáv szerkezetet az $M_{\vec{k}}$ mátrix \mathbf{k} -tól függő sajátértékei adják:

$$\det \begin{pmatrix} \epsilon_1 - \lambda & \dots & m_{18} \\ \vdots & \ddots & \vdots \\ m_{81} & \dots & \epsilon_8 - \lambda \end{pmatrix}$$

$$0 = P + Q(k),$$

pl. $t_1 = t_2 = t_3 = t_4 = t_5 = t_6$ esetén
vagy még általánosabban:

- $t_2 = t_5; t_1 t_3 = t_4 t_6$ és
- $\epsilon_5 = \epsilon_2$ vagy ϵ_3 és
- $\epsilon_6 = \epsilon_3$ vagy ϵ_2 esetén,

(F)

$$Q(k) = 4 \cos \frac{1}{2} (\gamma_{1 \rightarrow 2} + \gamma_{2 \rightarrow 3} + \gamma_{3 \rightarrow 4} + \gamma_{4 \rightarrow 5} + \gamma_{5 \rightarrow 6} + \gamma_{6 \rightarrow 1})$$

$$\cos \left[\frac{1}{2} (\gamma_{1 \rightarrow 2} + \gamma_{2 \rightarrow 3} + \gamma_{3 \rightarrow 4} + \gamma_{5 \rightarrow 4} + \gamma_{6 \rightarrow 5} + \gamma_{1 \rightarrow 6}) + \gamma_{4 \rightarrow 7} + \gamma_{7 \rightarrow 8} + \gamma_{8 \rightarrow a} + \mathbf{ka} \right]$$

$$\left[-(\epsilon_5 - \lambda)(\epsilon_6 - \lambda) t_1 t_2 t_3 t_7 t_8 t_9 + t_1 t_2 t_3 t_7 t_8 t_9 t_5^2 \right]$$

Amennyiben: $\gamma_{1 \rightarrow 2} + \gamma_{2 \rightarrow 3} + \gamma_{3 \rightarrow 4} + \gamma_{4 \rightarrow 5} + \gamma_{5 \rightarrow 6} + \gamma_{6 \rightarrow 1} = (2l + 1)\pi; l \in \mathbf{Z}$

$\rightarrow Q(k) = 0$ függetlenül \mathbf{k} -tól és t és ϵ paraméterektől

Eredmények: napelemes PPV származékok sávszerkezete

Teljesen lapos (diszperziómentes) sávszerkezet :

$$\Phi = \left(\frac{2l + 1}{2} \right) \Phi_0, \quad (l \in \mathbf{Z})$$

Φ := a fenilén hatszögön áthaladó mágneses fluxus.

- Független a vinilén-lánc jelenlététől
- Az eredmény megegyezik Trencsényi és társai (2011) polifenilén (PPP) láncra kapott eredményekkel
- A vinilénlánc szerepe:

$$2[t_9^2 - (\epsilon_7 - \lambda)(\epsilon_8 - \lambda)] t_1 t_2 t_3 t_6 t_4 t_5 \cos(\gamma_{1 \rightarrow 2} + \gamma_{2 \rightarrow 3} + \gamma_{3 \rightarrow 4} + \gamma_{4 \rightarrow 5} + \gamma_{5 \rightarrow 6} + \gamma_{6 \rightarrow 1})$$

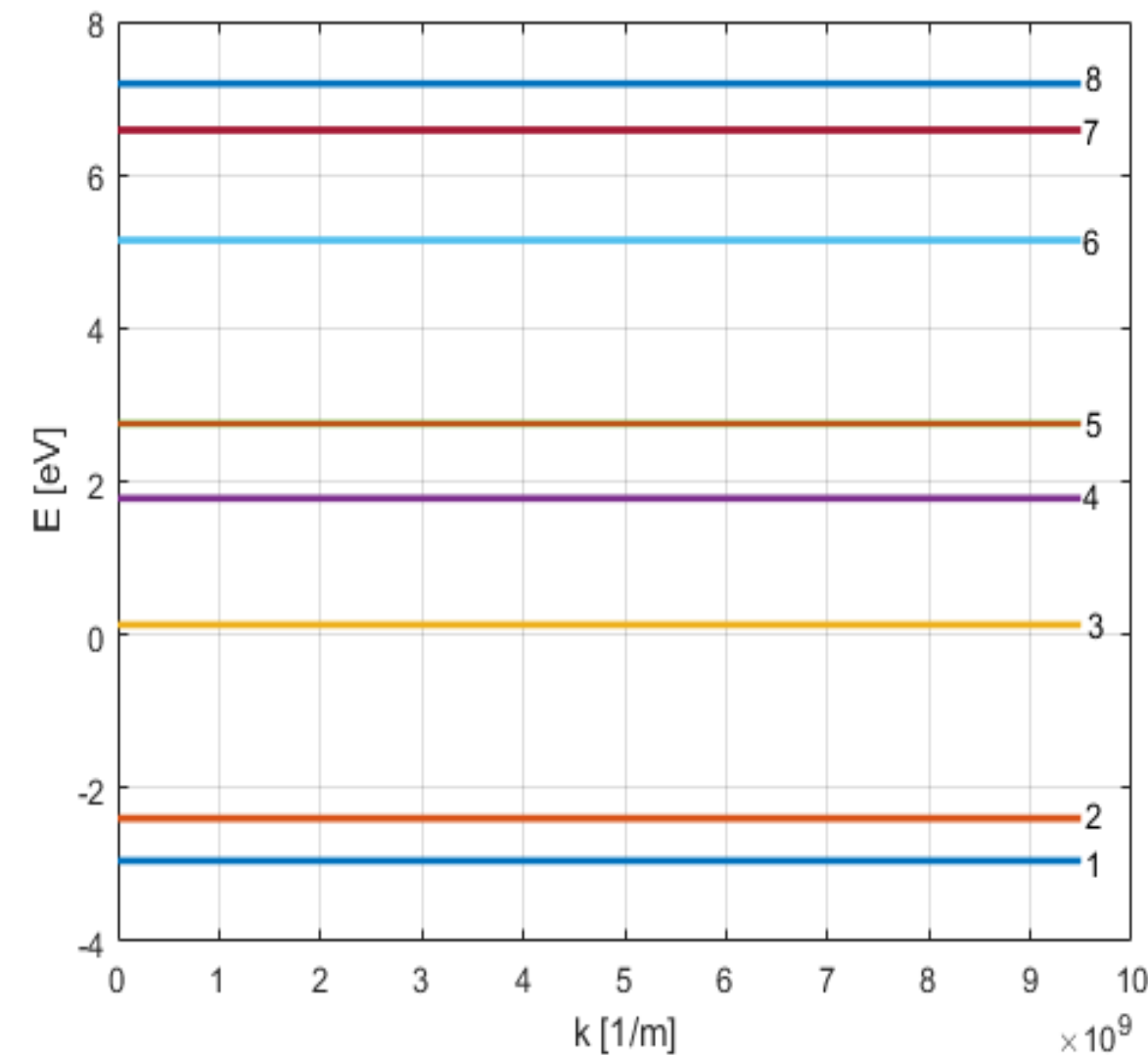
és $Q(k)$ „középső” tényezőjében jelenik meg.

Legkisebb mágneses indukció :

$l = 0$ esetén: $B = 4,1085 \cdot 10^4 T$!

A fenilén hatszög néhány angströmnyi oldalméretű .

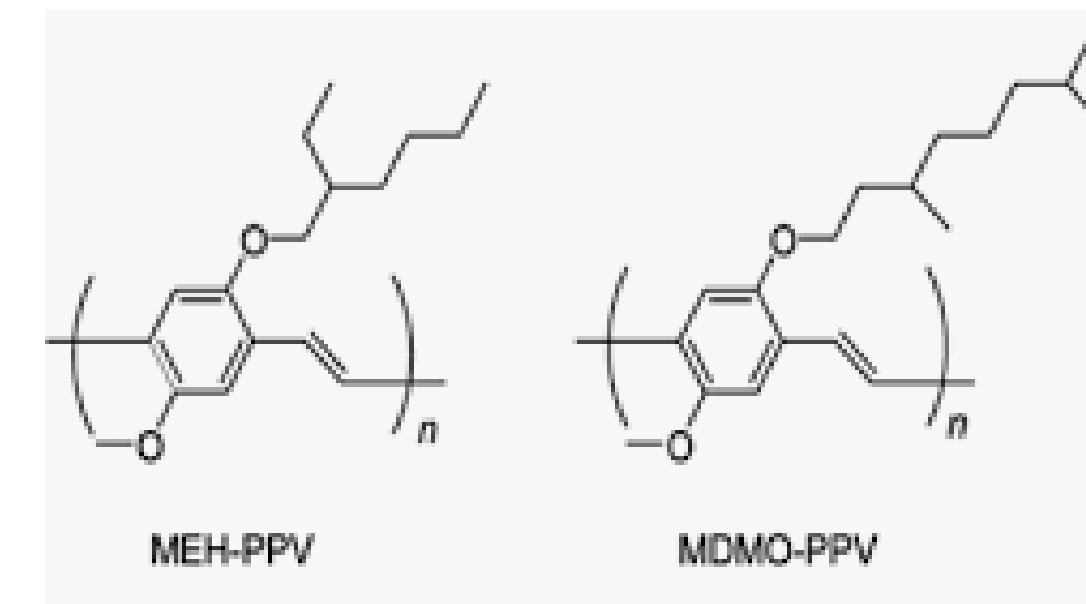
Ahhoz hogy az effektust kihasználhassuk a bezárt terület 10^4 – szeres növelésére lenne szükség!



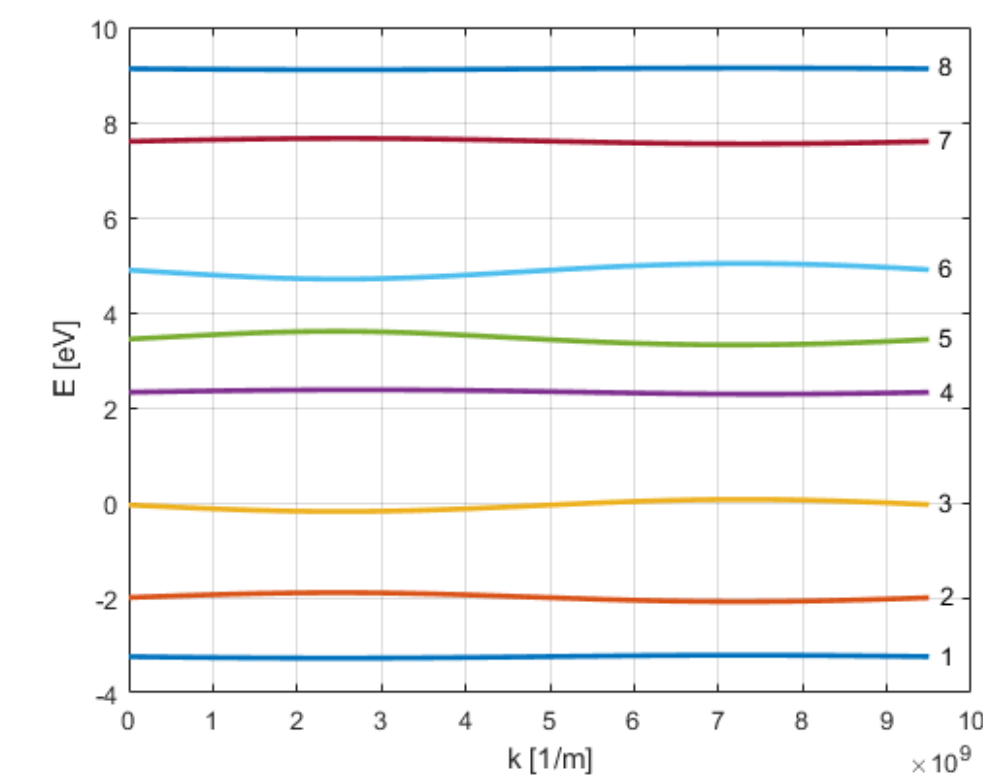
Teljesen lapos sávszerkezetű PPV a (4.11) feltételek szerint:

$t_1=t_2=t_3=t_4=t_5=t_6=2.4$ eV, $t_7=t_8=2.2$ eV, $t_9 = 2.6$ eV,
 $\epsilon_1 = \epsilon_4 = 0.5t_1$; $\epsilon_2 = \epsilon_3 = \epsilon_5 = \epsilon_6 = \epsilon_7 = \epsilon_8 = 1.1t_1$

Napelemes MEH-PPV, MDMO-PPV esetén:



F feltételek nem állhatnak fenn!

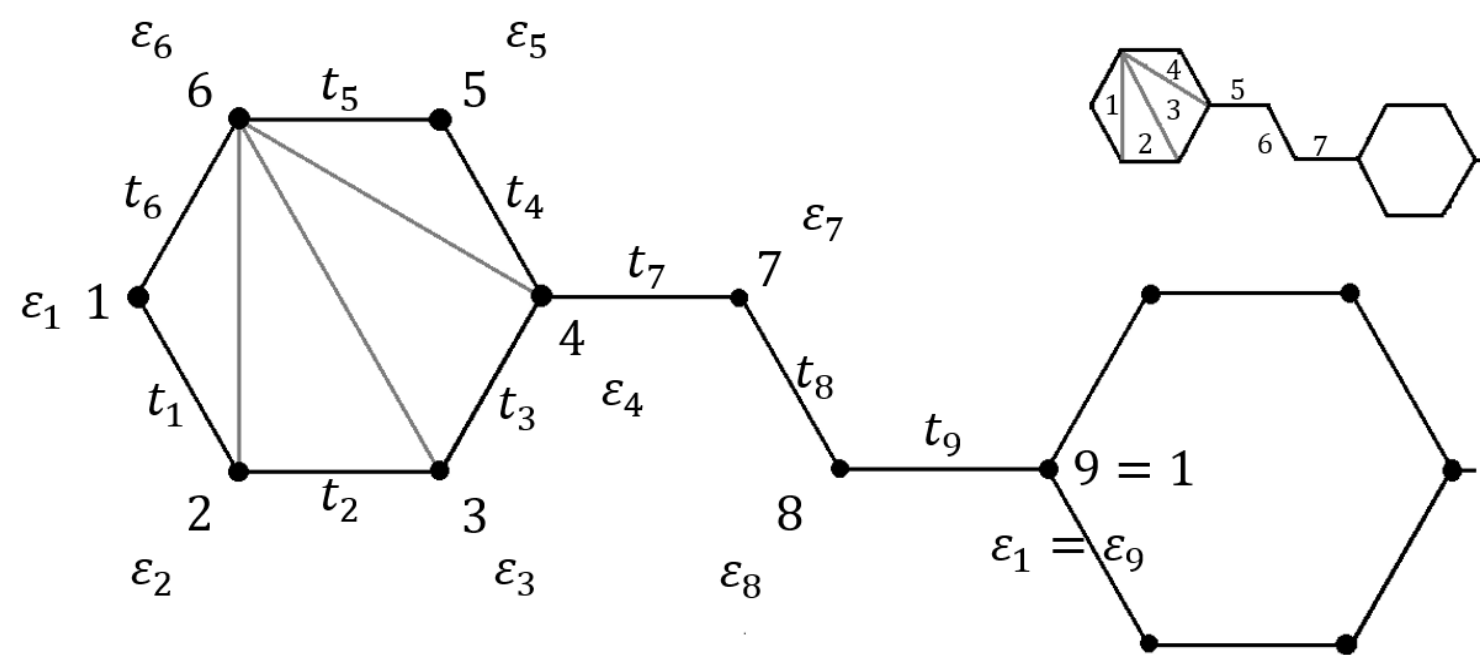


$t_1=t_2=t_3=t_4=t_5=t_6=2.4$ eV, $t_7=t_8=2.2$ eV, $t_9 = 2.6$ eV,
 $\epsilon_1 = \epsilon_4 = \epsilon_7 = \epsilon_8 = 1.2$ eV, $\epsilon_2 = 4.8$ eV, $\epsilon_3 = \epsilon_6 = 2.64$ eV, $\epsilon_5 = 7.2$ eV..

Eredmények: PPV-származékok alapállapota (alacsonykoncentrációs eset, legalsó sáv félig töltött)

Pozitív Szemidefinit Operátorok módszere

Blokkoperátorok:



$$\hat{A}_{i,1,\sigma}^{\rightarrow} = a_1 \hat{c}_{i,\sigma}^{\rightarrow} + a_2 \hat{c}_{i+\vec{r}_2,\sigma}^{\rightarrow} + a_6 \hat{c}_{i+\vec{r}_6,\sigma}^{\rightarrow},$$

$$\hat{A}_{i,2,\sigma}^{\rightarrow} = b_2 \hat{c}_{i+\vec{r}_2,\sigma}^{\rightarrow} + b_3 \hat{c}_{i+\vec{r}_3,\sigma}^{\rightarrow} + b_6 \hat{c}_{i+\vec{r}_6,\sigma}^{\rightarrow},$$

$$\hat{A}_{i,3,\sigma}^{\rightarrow} = d_3 \hat{c}_{i+\vec{r}_3,\sigma}^{\rightarrow} + d_4 \hat{c}_{i+\vec{r}_4,\sigma}^{\rightarrow} + d_6 \hat{c}_{i+\vec{r}_6,\sigma}^{\rightarrow},$$

$$\hat{A}_{i,4,\sigma}^{\rightarrow} = f_4 \hat{c}_{i+\vec{r}_4,\sigma}^{\rightarrow} + f_5 \hat{c}_{i+\vec{r}_5,\sigma}^{\rightarrow} + f_6 \hat{c}_{i+\vec{r}_6,\sigma}^{\rightarrow},$$

$$\hat{A}_{i,5,\sigma}^{\rightarrow} = g_4 \hat{c}_{i+\vec{r}_4,\sigma}^{\rightarrow} + g_7 \hat{c}_{i+\vec{r}_7,\sigma}^{\rightarrow},$$

$$\hat{A}_{i,6,\sigma}^{\rightarrow} = h_7 \hat{c}_{i+\vec{r}_7,\sigma}^{\rightarrow} + h_8 \hat{c}_{i+\vec{r}_8,\sigma}^{\rightarrow},$$

$$\hat{A}_{i,7,\sigma}^{\rightarrow} = k_8 \hat{c}_{i+\vec{r}_8,\sigma}^{\rightarrow} + k_9 \hat{c}_{i+\vec{r}_9,\sigma}^{\rightarrow},$$

ahol $\vec{r}_9 = \mathbf{r} = \mathbf{a} = \vec{a}$ és $a_1; a_2; a_6; b_2; \dots; k_9$ komplex számok.

$$\hat{H} = (\hat{H} - E_g \hat{1}) + E_g \hat{1} = \hat{P} + E_g \hat{1}$$

$$= \left(\sum_{\vec{i},\sigma} \sum_{m=1}^7 \hat{A}_{\vec{i},m,\sigma}^{\dagger} \hat{A}_{\vec{i},m,\sigma} + \hat{H}_U \right) + qN\hat{1},$$

Fedési egyenletek:

A két Hamilton operátor azonosságából

$$a_1; a_2; \dots; k_8; k_9$$

új együtthatók meghatározhatóak.

Az átalakíthatóság feltételei:

(Legfontosabb):

$$\frac{t_6 t_3}{t_1 t_2 t_4 t_5} \exp \left\{ -i \frac{2\pi}{\Phi_0} \oint_g \mathbf{A} \cdot d\mathbf{l} \right\} = \frac{t_6 t_3}{t_1 t_2 t_4 t_5} \exp \left\{ i \frac{2\pi}{\Phi_0} \Phi \right\}$$

negatív valós szám

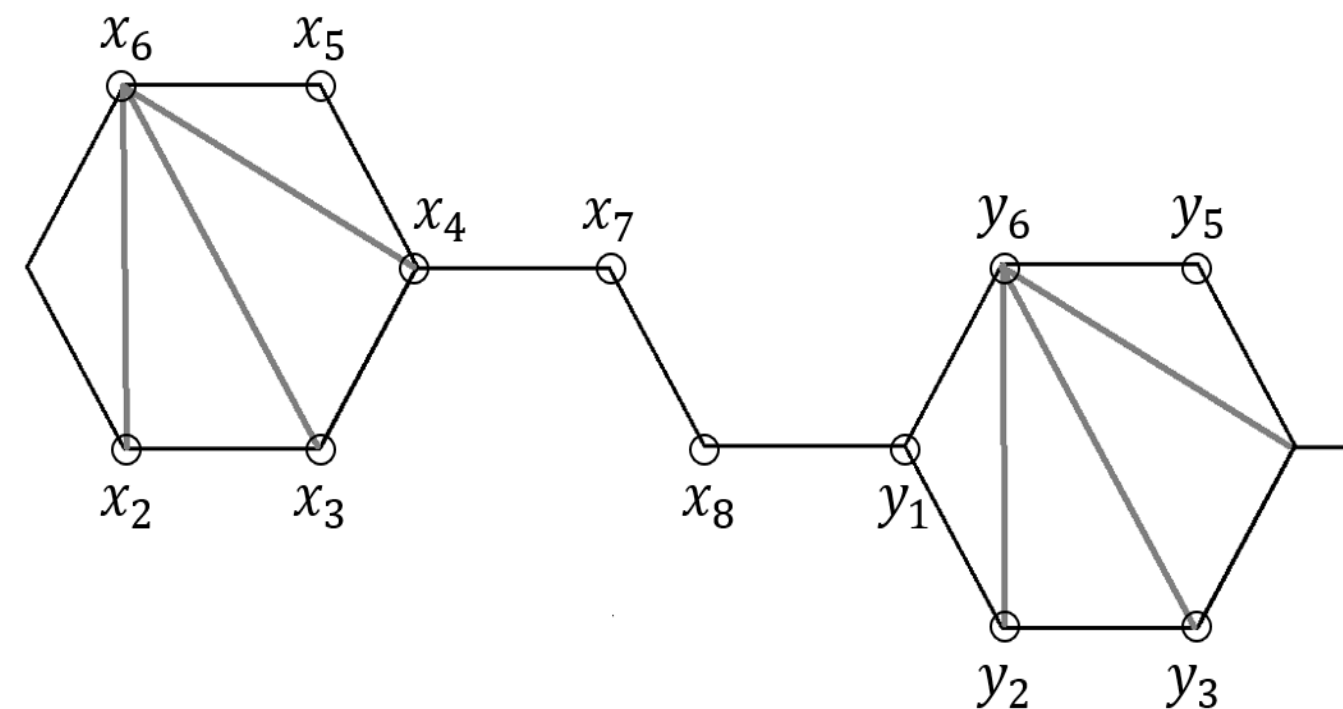
- $\Phi = \frac{k}{2} \Phi_0$; k tetszőleges egész szám

a) pl. $B=0$ esetén páratlan számú negatív t_k esetén valósul meg

b) $\Phi = \left(\frac{2l+1}{2} \right) \Phi_0$; (l tetszőleges egész szám) esetében páros számú t_k -nak kell negatívnak lennie

Ez utóbbi megegyezik Trencsényi és társai (2011)

eredményel



$$\hat{X}_{i,\sigma}^\dagger = \sum_{m=2}^8 x_m \hat{c}_{i+\vec{r}_m,\sigma}^\dagger + \sum_{n=1}^3 y_n \hat{c}_{i+\vec{a}+\vec{r}_n,\sigma}^\dagger + \sum_{k=5}^6 y_k \hat{c}_{i+\vec{a}+\vec{r}_k,\sigma}^\dagger$$

De az alapállapot eléréséhez a hullámfüggvénynek a \hat{H}_U kölcsönhatási tag magterébe is kell kerülnie!

A 2,3,5,6 csomópontoknál a dupla betöltést kell elkerülni, σ spinvetületekre nem végzünk produktumot:

$$|\Psi_g(N = N_c)\rangle = \prod_i \hat{X}_{i,\sigma}^\dagger |0\rangle$$

ahol pl. $\sigma = \uparrow$ és $|0\rangle$ a Fock-féle vákuumállapot

Az alapállapot levezetésének stratégiája:

$$\{\hat{A}_{i,\sigma,j}; \hat{X}_{i,\sigma}^\dagger\} = 0 \rightarrow \hat{H}_0(\prod_i \prod_\sigma \hat{X}_{i,\sigma}^\dagger |0\rangle) = 0$$

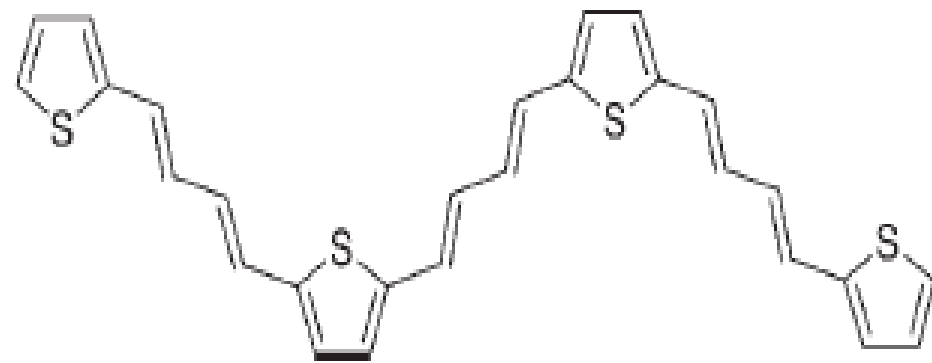
$\hat{A}_{i,\sigma,j}$	$\{\hat{A}_{i,\sigma,j}; \hat{X}_{i,\sigma}^\dagger\} = 0$
$\hat{A}_{i,\sigma,1}$	$x_2 a_2 + x_6 a_6 = 0$
$\hat{A}_{i,\sigma,2}$	$x_2 b_2 + x_3 b_3 + x_6 b_6 = 0$
$\hat{A}_{i,\sigma,3}$	$x_3 d_3 + x_4 d_4 + x_6 d_6 = 0$
$\hat{A}_{i,\sigma,4}$	$x_4 f_4 + x_5 f_5 + x_6 f_6 = 0$
$\hat{A}_{i,\sigma,5}$	$x_7 g_7 + x_4 g_4 = 0$
$\hat{A}_{i,\sigma,6}$	$x_8 h_8 + x_7 h_7 = 0$
$\hat{A}_{i,\sigma,7}$	$y_1 k_9 + x_8 k_8 = 0$
$\hat{A}_{i+\vec{a},\sigma,1}$	$y_1 a_1 + y_2 a_2 + y_6 a_6 = 0$
$\hat{A}_{i+\vec{a},\sigma,2}$	$y_2 b_2 + y_3 b_3 + y_6 b_6 = 0$
$\hat{A}_{i+\vec{a},\sigma,3}$	$y_3 d_3 + y_6 d_6 = 0$
$\hat{A}_{i+\vec{a},\sigma,4}$	$y_5 f_5 + y_6 f_6 = 0$

Eredmények: a PPV alapállapot fizikai jellemzése, általánosítása

Az alapállapot jellemzése:

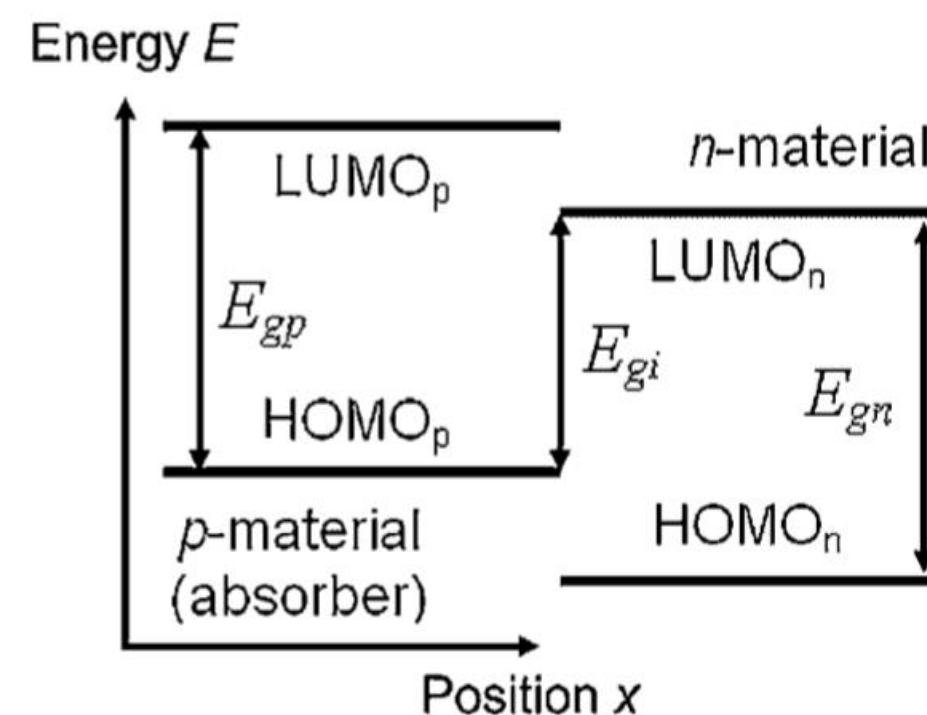
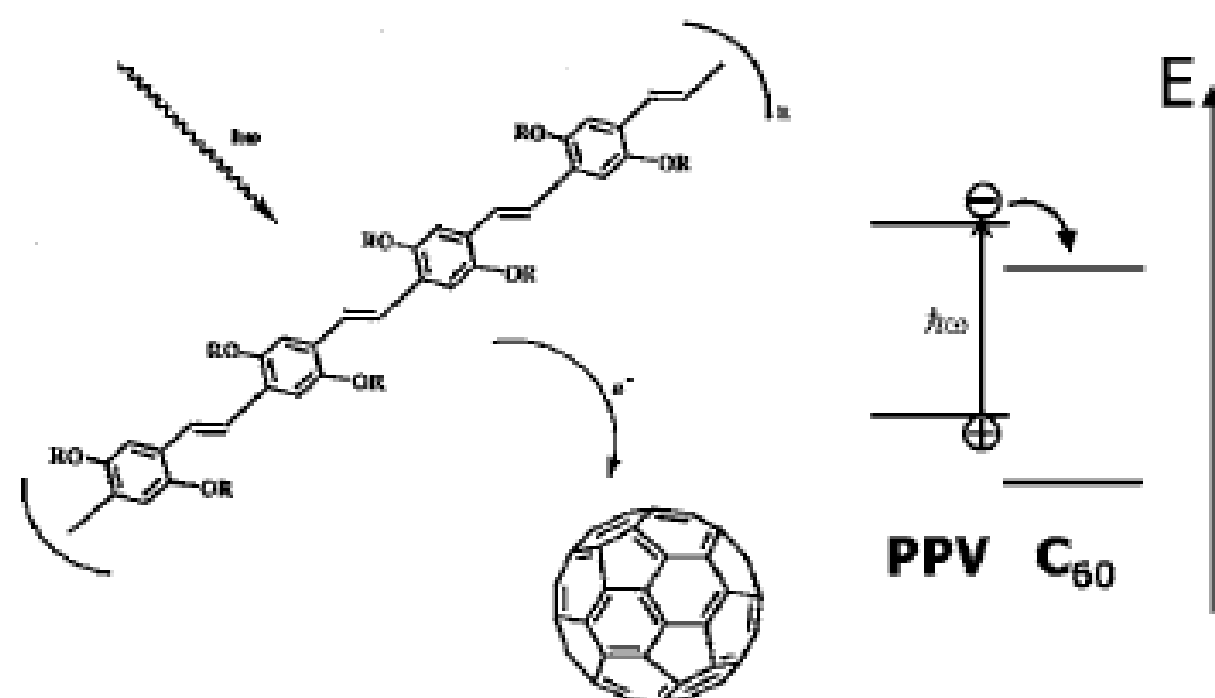
- telített ferromágneses,
- a spinvetületek korreláltságát a \hat{H}_U kölcsönhatási tag okozta, nem a külső B mágneses mező(!),
- $\Phi = \left(\frac{2l+1}{2}\right)\Phi_0$ esetén (teljesen lapos, diszperziómentes sávszerkezet) a ferromágneses alapállapot ún. Mielke-Tasaki formában valósul meg (a legalsó sáv diszperziómentes és az alapállapot teljesíti az összefüggőségi feltételt)
- a rendszer töltöttsége $\rho = 1/8$, azaz minden egységcellához 1 db elektron tartozik, a legalsó sáv félig betöltött

A módszer általánosítása:



- (Roncali, 2007)

Eredmények: Politiófen-fullerén típusú napelemek maximális hatásfokára adott becslések

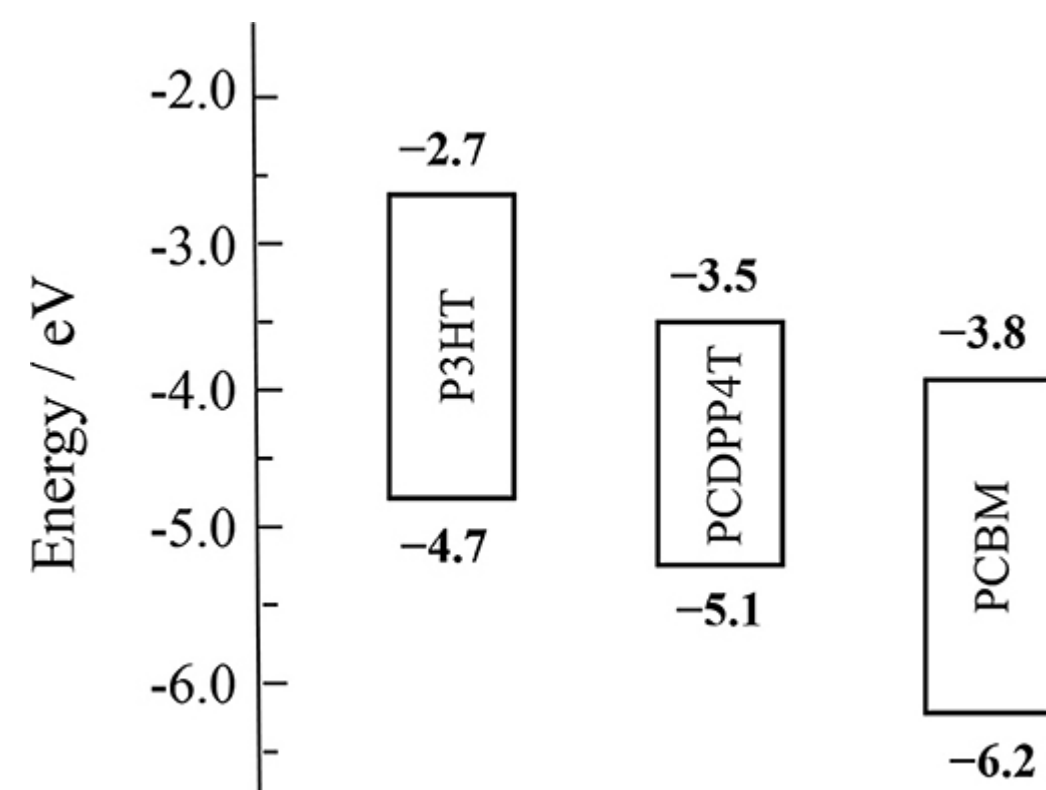


$$\eta_{max} = \frac{E_{g,i} \int_{E_{g,abszorber}}^{\infty} N(E) dE}{\int_0^{\infty} EN(E) dE}$$

$N(E)$ az AM 1.5 beeső szoláris fotonfluxus tapasztalati, mért energiatfüggése (Hulström és társai, 1985)

Az exciton gerjesztődése és további átalakulása a PPV: C₆₀ donor/akceptor napelemben Günes és társai (2007)

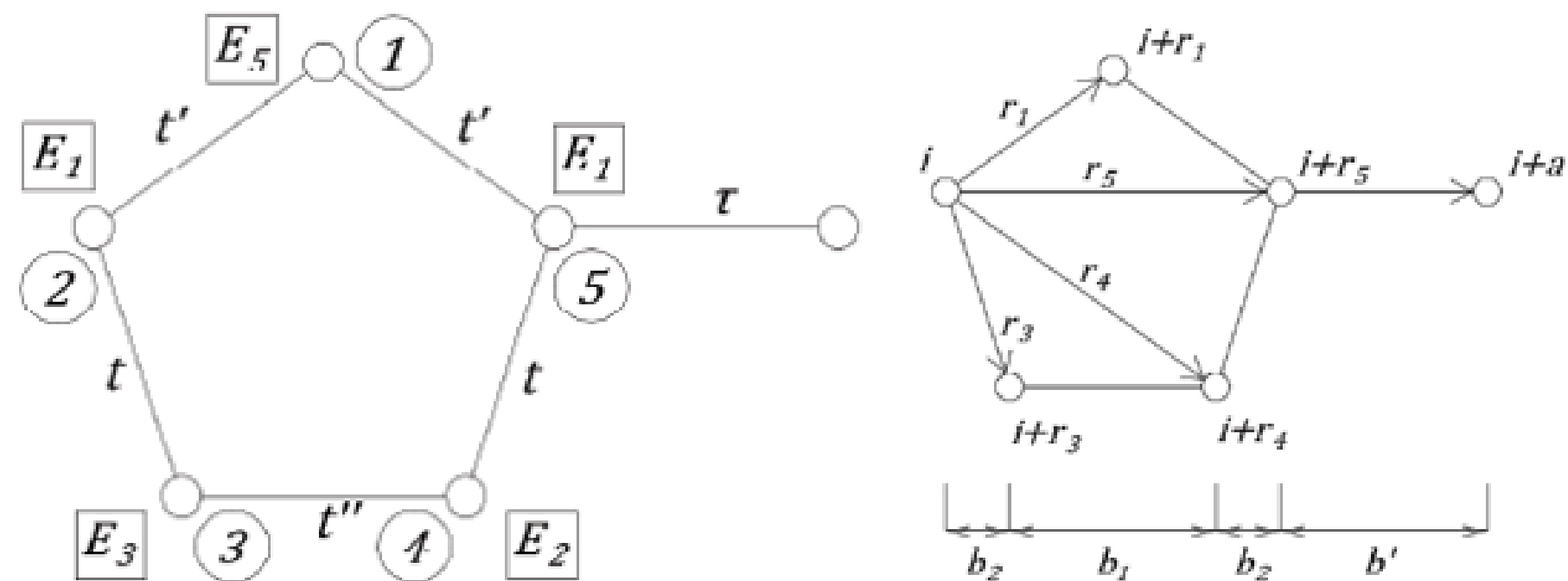
A donor és akceptor anyagok relatív LUMO, HOMO energiaszintjei és a hatásfokképlet értelmezése (Minnaert, Burgelmann, 2007)



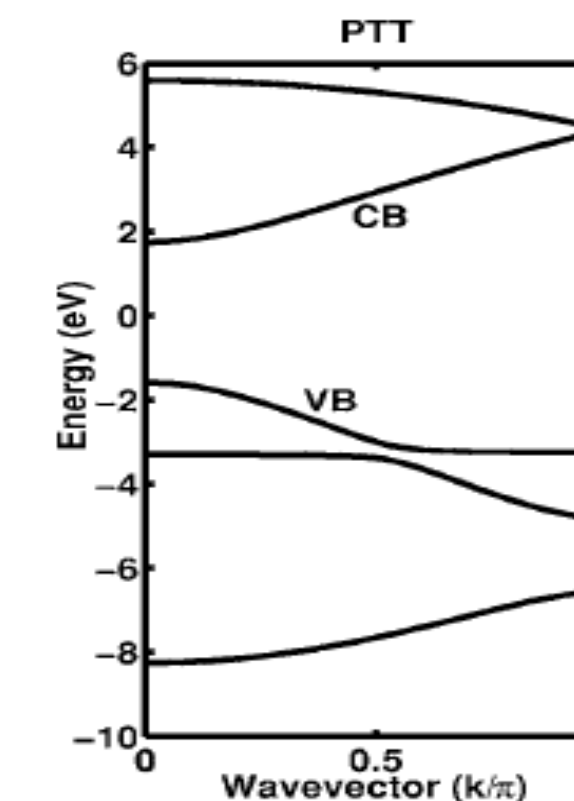
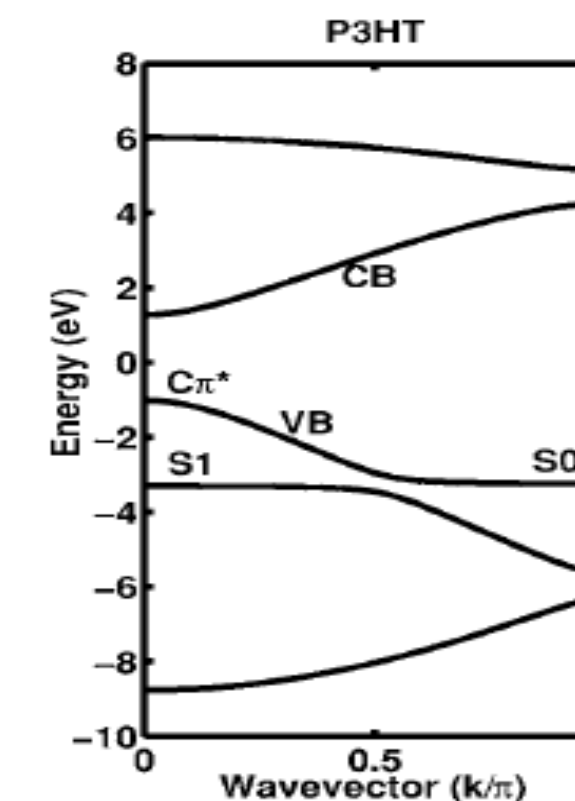
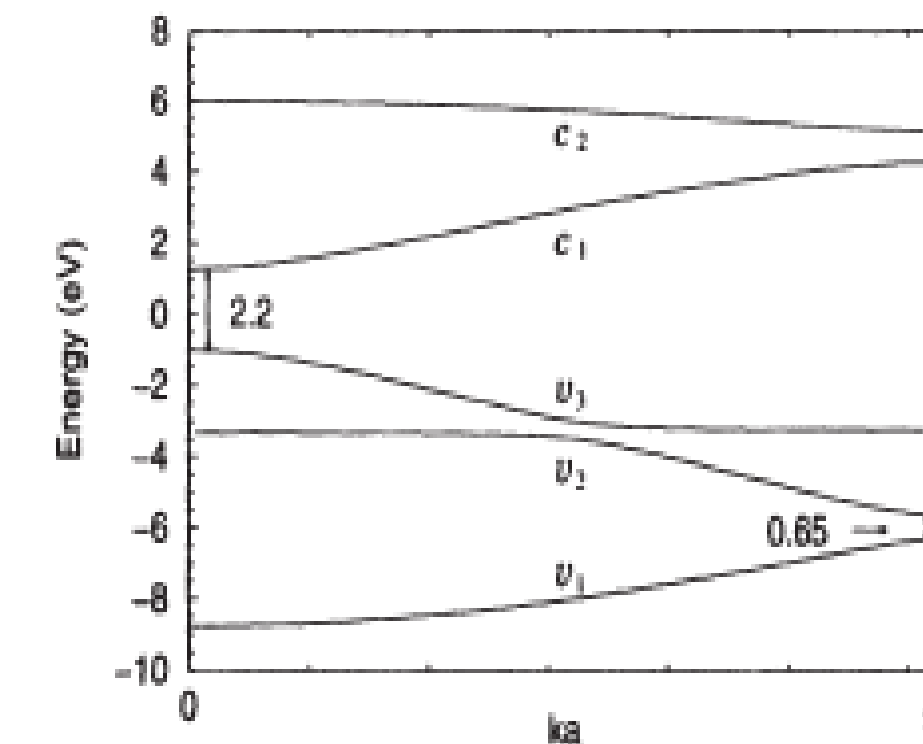
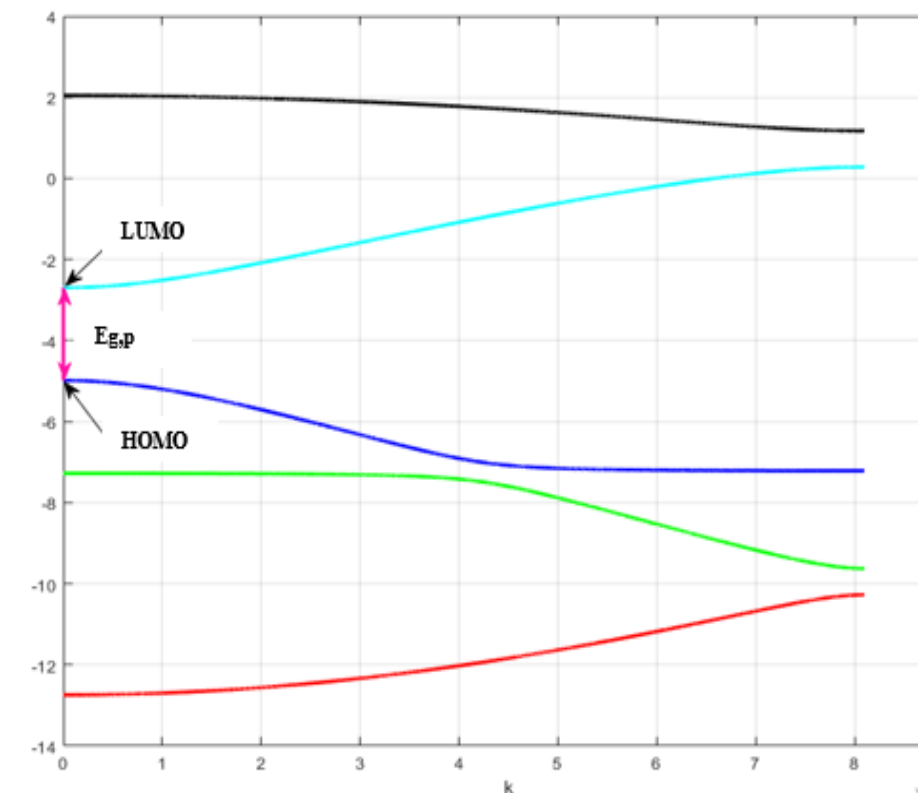
- csak az egyik anyag abszorbeálja a fotonokat, ez a *p*-típusú donor anyag, a polimer, esetünkben a P3HT,
- minden olyan foton, amelynek energiája nagyobb $E_{g,abszorber}$ -nél és csakis ezek nyelődnek el a donorban és válnak ki fotoeffektust,
- valamennyi fotonelnyelődés a polimerben a folyamat végén szabad elektron és lyuk töltéseket eredményez $E_{g,i}$ hasznos energiával.
- Mellékfeltételként teljesülnie kell a $\Delta LUMO = LUMO (donor) - LUMO (akceptor) \geq 0,2 \text{ eV}$ egyenlőtlenségnek,

Eredmények – a politiofén Hubbard modellje

$$\hat{H}_0 = \sum_{\sigma} \sum_{i=1}^{N_C} \{ [\tau \hat{c}_{i+r_5, \sigma}^{\dagger} \hat{c}_{i+a, \sigma} + t'' \hat{c}_{i+r_3, \sigma}^{\dagger} \hat{c}_{i+r_4, \sigma} + t' (\hat{c}_{i+r_1, \sigma}^{\dagger} \hat{c}_{i, \sigma} + \hat{c}_{i+r_5, \sigma}^{\dagger} \hat{c}_{i+r_1, \sigma}) + t (\hat{c}_{i, \sigma}^{\dagger} \hat{c}_{i+r_3, \sigma} + \hat{c}_{i+r_4, \sigma}^{\dagger} \hat{c}_{i+r_5, \sigma}) + t_1 (\hat{c}_{i+r_3, \sigma}^{\dagger} \hat{c}_{i+r_1, \sigma} + \hat{c}_{i+r_4, \sigma}^{\dagger} \hat{c}_{i+r_1, \sigma}) + H.c.] + E_5 \hat{n}_{i+r_1, \sigma} + E_1 (\hat{n}_{i, \sigma} + \hat{n}_{i+r_5, \sigma}) + E_3 \hat{n}_{i+r_3, \sigma} + E_2 \hat{n}_{i+r_4, \sigma} \}$$



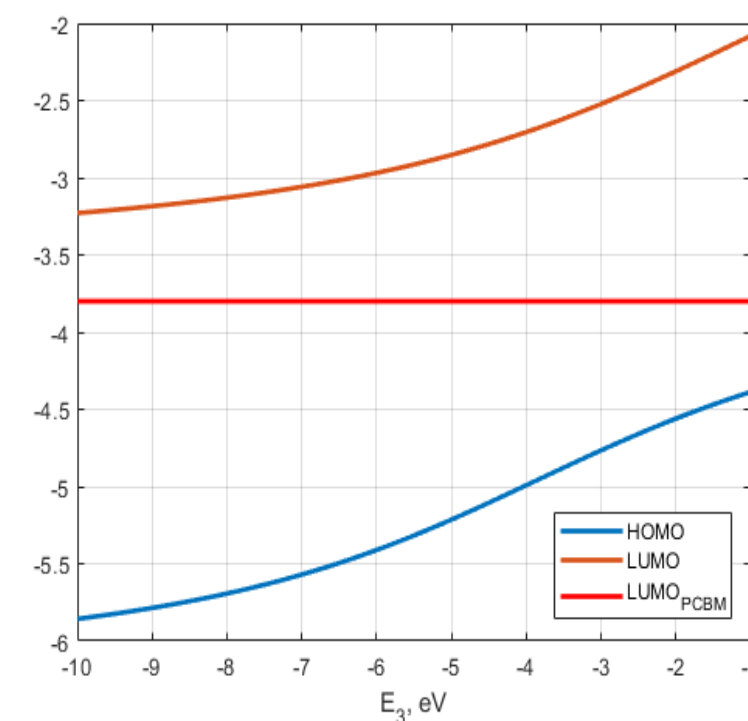
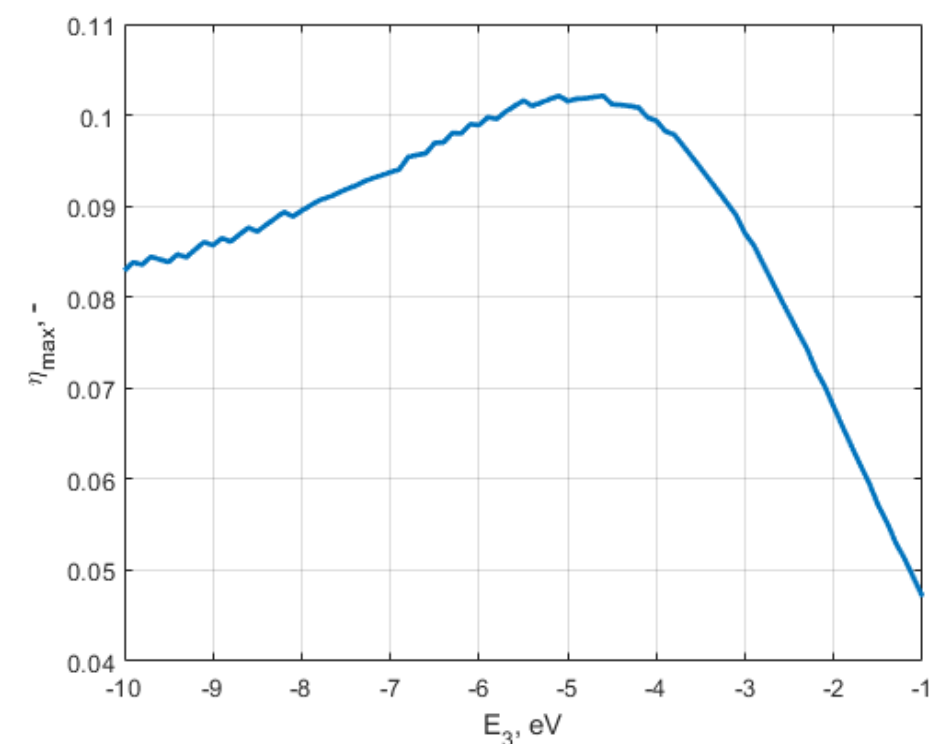
E_1	E_2	E_5	t	t'	t''	τ
-1	0	-3,8	-3,5	-2,5	-2,8	-3,2
$E_{offset} = -3,972$						



A politiofén Hubbard modellje. Balra fent: a rendszer Hubbard paramétereit, jobbra fent: geometriai jelöléseket, lent: a modellparaméterek konkrét értékeit (Lu és Meng, (2007) és Farchioni, Grosso, (2001) adatai alapján)

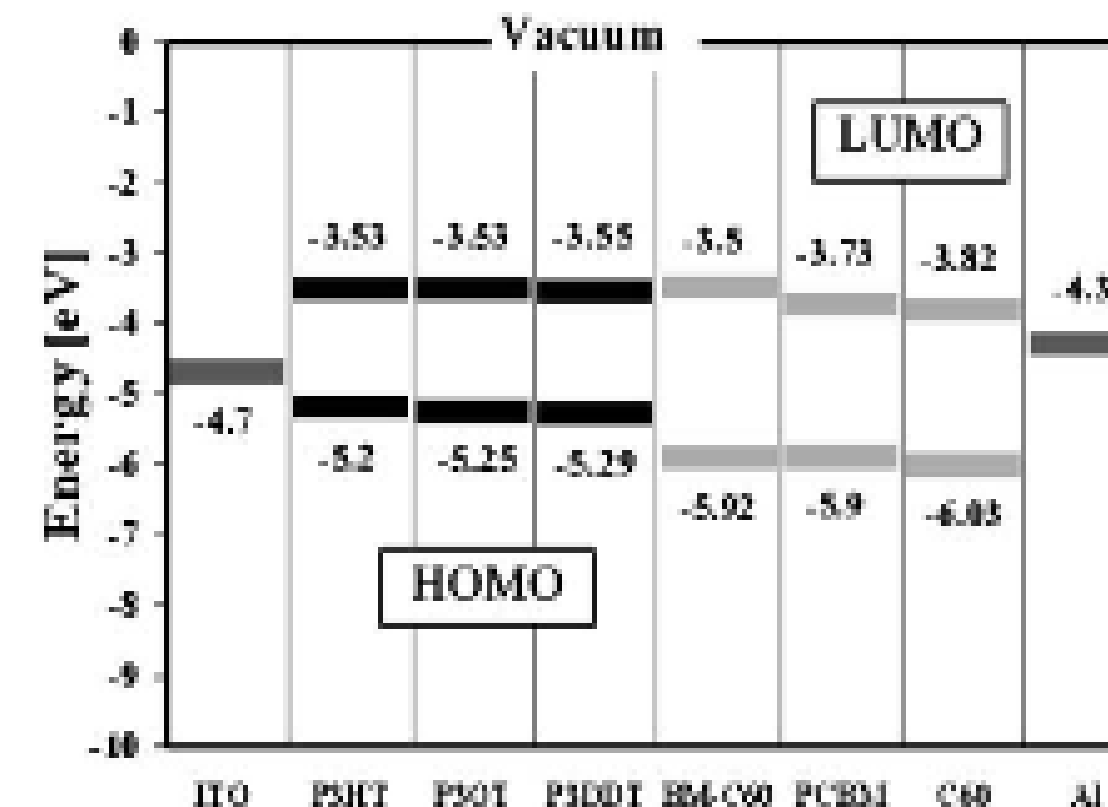
A P3HT-re általunk (fent, balra) és a szakirodalom által a P3HT-re, PTT-re (poly(3,4_-dialkil-2 ,2,5,2-tertiofén)) ill. a politiofénre megadott sávszerkezet (lent: Lu, Meng, 2008, fent jobbra: szerk. Farchioni, Grosso, 2001)

Eredmények – a rendszer hatásfokgörbéje



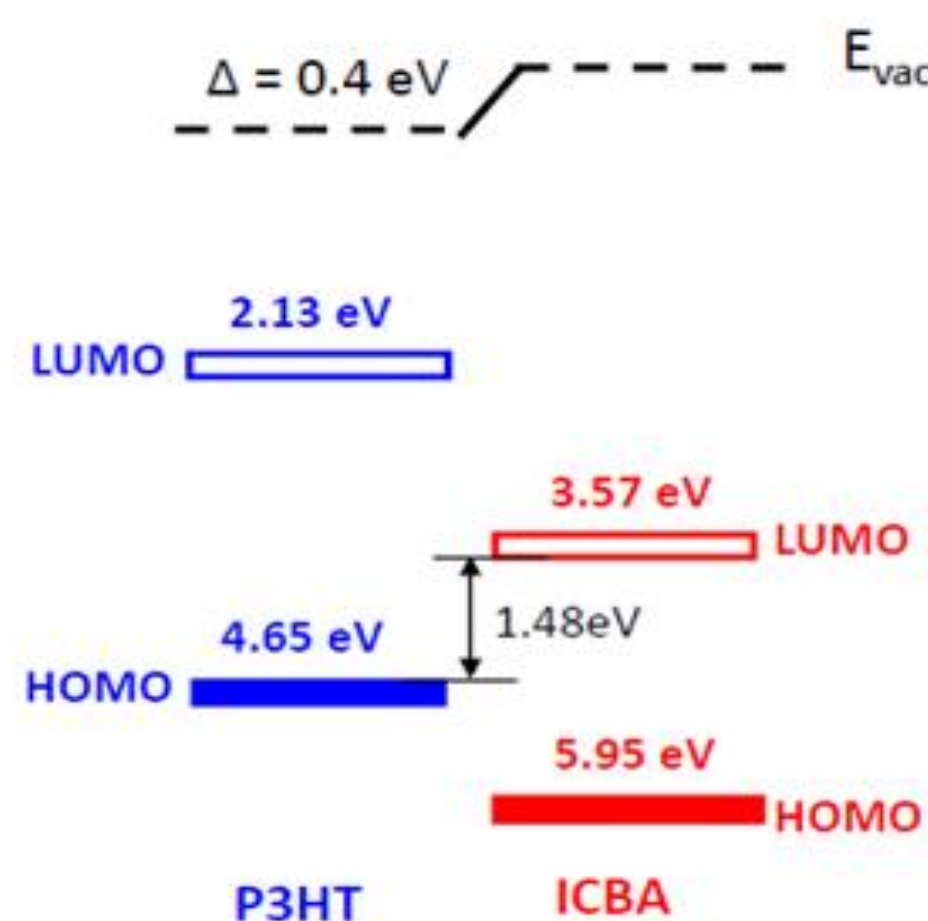
A maximális hatásfok (bal oldali ábra) valamint a vizsgált polimercsalád HOMO és LUMO szintjei (jobb oldali ábra) változása az E_3 csomóponti potenciál függvényében

A P3HT az $E_3 = -3,97$ eV-hez tartozik

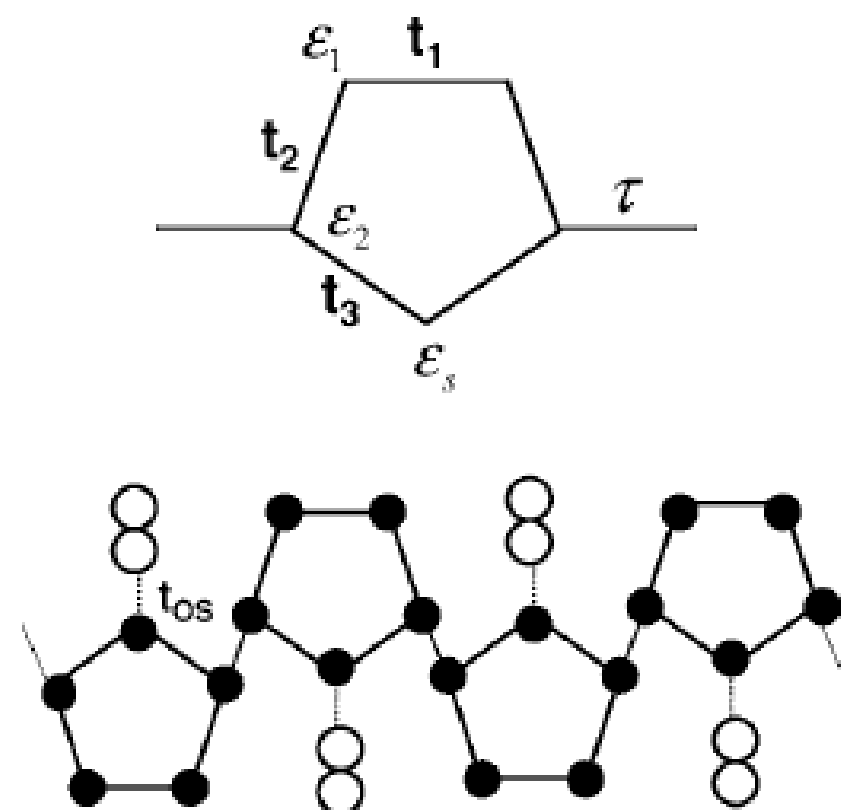
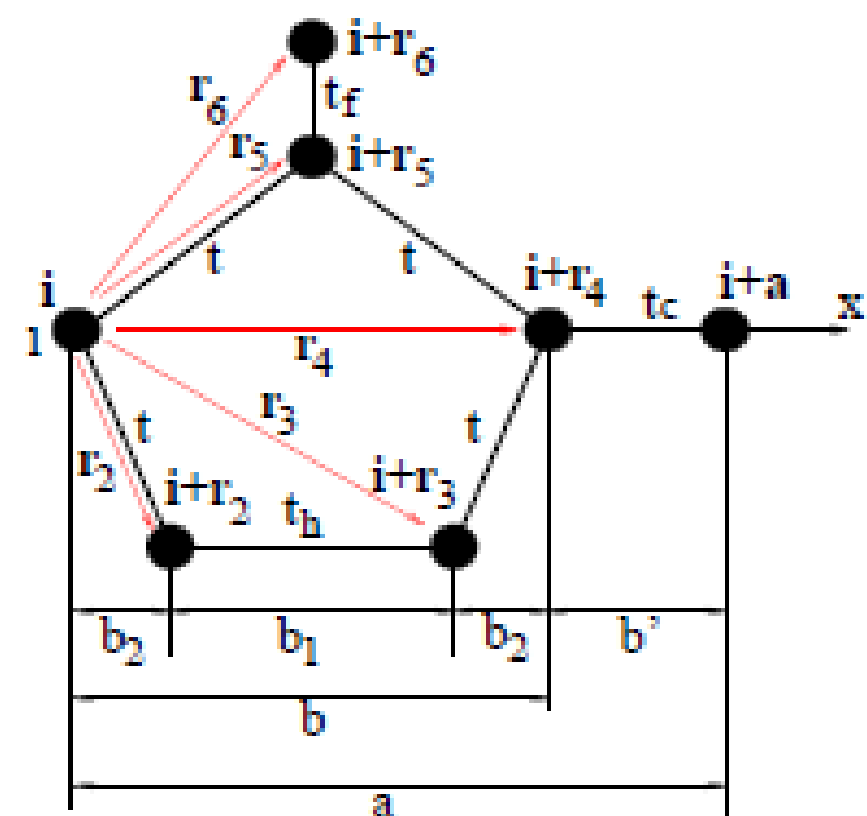


A P3HT, P3OT, P3DDT politiofén származékok ill. BM-C60, PCBM ill. C₆₀ fullerének HOMO és LUMO szintjei a CV módszerrel mérve (az ITO és Al elektródák munkafüggvényeivel) (Al-Ibrahim és társai, 2005).

Állításunk: a felületi dipólustól származó eltolódás modellezhető magából a sávszerkezetből Vázquez és társai, (2005) alapján



A P3HT:ICBA (poly(3-hexylthiophene):indene-C60 bisadduct) keverék vákuumszint eltolódása egy közel 200 meV, a méréshez rendelhető érték levonása után (Guan és társai, 2010, 2011)

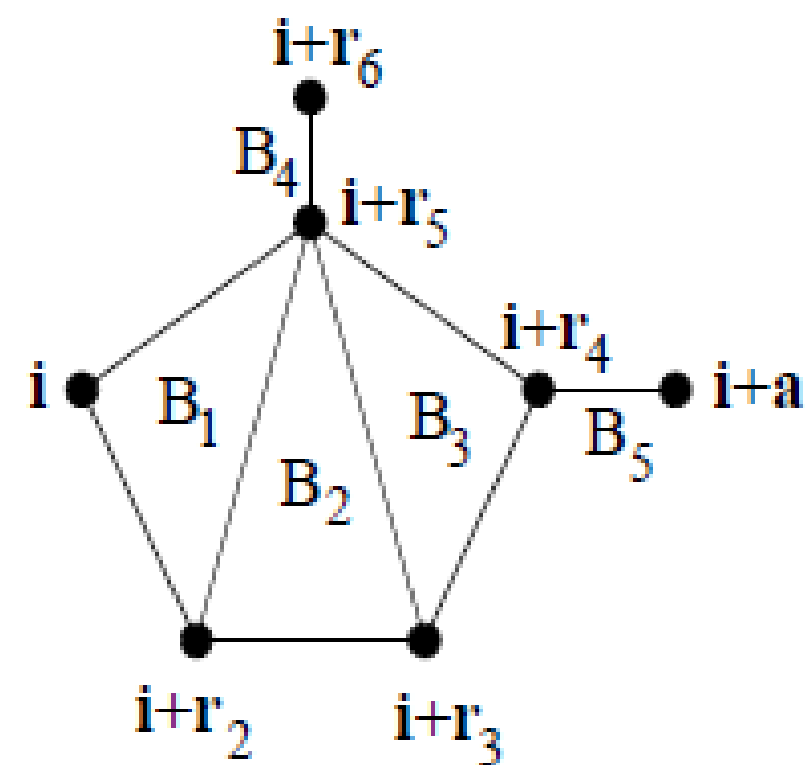


A Hamilton operátorban a spin-pálya csatolás effektusának figyelembevétele:

az $\vec{i} + \vec{r}_4$ és $\vec{i} + \vec{a} = \vec{i}$ (Born-Kármán feltétel) csomópontok között a spinfüggő $t_c^{\uparrow\uparrow}$; $t_c^{\downarrow\downarrow}$; $t_c^{\uparrow\downarrow}$; $t_c^{\downarrow\uparrow}$ hopping tényezők ill. $\epsilon_1^{\uparrow\uparrow}$; $\epsilon_1^{\downarrow\downarrow}$; $\epsilon_4^{\uparrow\uparrow}$; $\epsilon_4^{\downarrow\downarrow}$ ugyancsak spinfüggő csomóponti potenciálok felvétele. A „vegyes” potenciálokat $\epsilon_1^{\uparrow\downarrow}$; $\epsilon_1^{\downarrow\uparrow}$; $\epsilon_4^{\uparrow\downarrow}$; $\epsilon_4^{\downarrow\uparrow} = 0$ -nak vettem (Kucska és Gulácsi, 2018).

A P3HT polimer O_2 adszorpciójának modellje a poliaminotriazol polimer modellje (Gulácsi és társai, 2010, 2013) alapján valamint Lu és Meng (2007) szerint

Cél: a politiofén oxidációjának irodalmi adataira támaszkodó konkrét alapállapotú hullámfüggvény megadása



$$\begin{aligned}\hat{G}_{1,\vec{r},\sigma} &= a_{1,1}\hat{c}_{i+\vec{r}_1,\sigma} + a_{1,2}\hat{c}_{i+\vec{r}_2,\sigma} + a_{1,5}\hat{c}_{i+\vec{r}_5,\sigma} \\ \hat{G}_{2,\vec{r},\sigma} &= a_{2,2}\hat{c}_{i+\vec{r}_2,\sigma} + a_{2,3}\hat{c}_{i+\vec{r}_3,\sigma} + a_{2,5}\hat{c}_{i+\vec{r}_5,\sigma} \\ \hat{G}_{3,\vec{r},\sigma} &= a_{3,3}\hat{c}_{i+\vec{r}_3,\sigma} + a_{3,4}\hat{c}_{i+\vec{r}_4,\sigma} + a_{3,5}\hat{c}_{i+\vec{r}_5,\sigma} \\ \hat{G}_{4,\vec{r},\sigma} &= a_{4,4}\hat{c}_{i+\vec{r}_4,\sigma} + a_{4,6}\hat{c}_{i+\vec{r}_6,\sigma}, \quad (\sigma = \uparrow, \downarrow)\end{aligned}$$

$$\begin{aligned}\hat{G}_{5,i,\uparrow} &= g_4^\uparrow \hat{c}_{i+r_4,\uparrow} + g_7^\uparrow \hat{c}_{i+a,\uparrow} + g_4^\downarrow \hat{c}_{i+r_4,\downarrow} + g_7^\downarrow \hat{c}_{i+a,\downarrow} \hat{G}_{2,\vec{r},\sigma} \\ &= a_{2,2}\hat{c}_{i+\vec{r}_2,\sigma} + a_{2,3}\hat{c}_{i+\vec{r}_3,\sigma} + a_{2,5}\hat{c}_{i+\vec{r}_5,\sigma}, \\ \hat{G}_{6,i,\uparrow} &= F_4^\uparrow \hat{c}_{i+r_4,\uparrow} + F_7^\uparrow \hat{c}_{i+a,\uparrow} + F_4^\downarrow \hat{c}_{i+r_4,\downarrow} + F_7^\downarrow \hat{c}_{i+a,\downarrow}\end{aligned}$$

Két megoldás: a)

$$\begin{aligned}-t_c^{\uparrow\uparrow} &= 1,96 \text{ eV}, \\ -t_c^{\downarrow\downarrow} &= 2,042 \text{ eV}, \\ (-t_c^{\downarrow\uparrow})^* &= 1,922 * 10^{-4} \text{ eV}, \\ -t_c^{\uparrow\downarrow} &= -1,88 * 10^{-4} \text{ eV}\end{aligned}$$

b)

$$\begin{aligned}-t_c^{\uparrow\uparrow} &= 2,0775 \text{ eV}, \\ -t_c^{\downarrow\downarrow} &= 2,0775 \text{ eV}, \\ -t_c^{\uparrow\downarrow} &= 0,135 \text{ eV}, \\ (-t_c^{\downarrow\uparrow})^* &= -0,189 \text{ eV}\end{aligned}$$

$$\begin{aligned}\hat{H}_0 = \sum_i \left\{ t_c^{\uparrow\uparrow} \hat{c}_{i+r_4,\uparrow}^\dagger \hat{c}_{i+a,\uparrow} + t_c^{\downarrow\downarrow} \hat{c}_{i+r_4,\downarrow}^\dagger \hat{c}_{i+a,\downarrow} + t_c^{\downarrow\uparrow} \hat{c}_{i+r_4,\downarrow}^\dagger \hat{c}_{i+a,\uparrow} \right. \\ + t_c^{\uparrow\downarrow} \hat{c}_{i+r_4,\uparrow}^\dagger \hat{c}_{i+a,\downarrow} + H.c. + \epsilon_1^{\uparrow\uparrow} \hat{n}_{i,\uparrow\uparrow} + \epsilon_1^{\downarrow\downarrow} \hat{n}_{i,\downarrow\downarrow} + \epsilon_4^{\uparrow\uparrow} \hat{n}_{i+r_4,\uparrow\uparrow} \\ + \epsilon_4^{\downarrow\downarrow} \hat{n}_{i+r_4,\downarrow\downarrow} \\ + \sum_{\sigma=\uparrow,\downarrow} \left\{ t_f \hat{c}_{i+r_6,\sigma}^\dagger \hat{c}_{i+r_6,\sigma} + t_h \hat{c}_{i+r_2,\sigma}^\dagger \hat{c}_{i+r_2,\sigma} \right. \\ + t \left(\hat{c}_{i+r_5,\sigma}^\dagger \hat{c}_{i,\sigma} + \hat{c}_{i+r_3,\sigma}^\dagger \hat{c}_{i+r_4,\sigma} + \hat{c}_{i+r_4,\sigma}^\dagger \hat{c}_{i+r_5,\sigma} + \hat{c}_{i,\sigma}^\dagger \hat{c}_{i+r_2,\sigma} \right) \\ \left. + H.c. + \sum_{n=2,3,5,6} \epsilon_n \hat{n}_{i+r_n,\sigma} \right\} \Bigg\},\end{aligned}$$

$$\hat{H}_U = \sum_i \sum_{n=1}^6 U_n \hat{n}_{i+\vec{r}_n,\uparrow} \hat{n}_{i+\vec{r}_n,\downarrow}$$

$$\Psi_{\text{alapállapot}} = \prod_{i=1}^{N_c} \left\{ \left(\prod_{\sigma=\uparrow,\downarrow} \prod_{\alpha=1}^4 \hat{G}_{\alpha,i,\sigma}^\dagger \right) \hat{G}_{5,i}^\dagger \hat{G}_{6,i}^\dagger \hat{c}_{i+\vec{r}_{n_i},\uparrow}^\dagger \right\} |0\rangle$$

A hullámfüggvény minden cellában 5db \uparrow és 4 db \downarrow spinű elektront tartalmaz. A $\hat{G}_{5,i}^\dagger$ és $\hat{G}_{6,i}^\dagger$ operátorok mindegyike vagy \uparrow vagy \downarrow spinű elektront kelt az elemi cellában, ezért valamelyik irányú spinből biztosan lesz 6 db egy cellában. Mivel azonos spinnel rendelkező elektronok csak különböző csomópontokra kerülhetnek, ezért biztosan lesz mindegyik csomóponton valamilyen spinű elektron. Látható, hogy ez nem teljesülne, ha $\hat{c}_{i+\vec{r}_{n_i},\uparrow}^\dagger$ nem lenne jelen a hullámfüggvényben.

1. Polifenilén-vinilén származékok sávszerkezete állandó, külső mágneses mező jelenléte esetén

A szakirodalmi előzmények alapján modellt állítottam fel polifenilén-vinilén (PPV) származékok általános matematikai vizsgálatához külső, állandó mágneses mező jelenléte esetére. Ezek a származékok a polimervázhoz kapcsolódó oldalcsoportokban különböznek egymástól. A modell paramétereit tetszőlegesek.

Megmutattam, hogy ezen PPV polimerszármazékok esetén is létrejöhet a sávszerkezet valamennyi sávjának egyidejű egyenessé válása (teljesen lapos sávszerkezet), hasonlóan a már korábban polifenilén láncolatú polimerekre megjósolt esetekhez hasonlóan. Meghatároztam a teljesen lapossá válás feltételeit a paraméterekre vonatkozóan. Megadtam a teljes kilaposodáshoz tartozó mágneses indukciók értékeinek halmazát, megmutattam, hogy ez a halmaz megegyezik a polifenilén láncokra kapott indukció értékek halmazával. Igazoltam, hogy a teljes kilaposodásra a hosszabb vinilénlánc nincsen hatással, csak a hatszög fenilényűrűn átmenő fluxus a meghatározó. Ugyanakkor részletesen megmutattam a vinilénlánc hatását a sávszerkezetre.

2. A napelemes alkalmazások legfontosabb polifenilén-vinilén származékainak sávszerkezete állandó külső mágneses mező jelenléte esetén

Megmutattam, hogy a legfontosabb napelemes polimerek, MEH-PPV, MDMO-PPV esetén a teljesen diszperziómentes sávszerkezet nem következhet be. Illusztratív ellenpéldán, ahol a valamennyi sáv egyidejű egyenessé válásának feltételei nem állnak fenn, számítógépes szimuláció segítségével igazoltam két sáv esetében, hogy bár a mágneses mező a sávokat laposítja, mindig marad diszperzió. Meghatároztam az egyes sávokhoz tartozó azon legkisebb mágneses indukció értékeket, amelyre az adott sáv leginkább egyenessé válik. Meghatároztam a sávszerkezet periódusát.

3. Polifenilén-vinilén származékok alapállapota állandó, külső mágneses mező jelenléte esetén

A pozitív szemidefinit operátorok módszerével az összefüggőségi feltételt kielégítő, telített ferromágneses alapállapotú hullámfüggvényt vezettem le a vizsgált PPV származékokra. A rendszer cellánként 1 db delokalizált π -elektront tartalmazott (a legalsó sáv félig betöltött).

Megadtam a módszer alkalmazhatóságának feltételeit. Ezek közül a legfontosabb, hogy a kezdő paraméterek között marad egy kényszerfeltétel. Megmutattam, hogy a módszer, az általam alkalmazott felbontás mellett csak diszkrét mágneses indukció értékek esetén lehetséges, ezen értékek halmazát meghatároztam. Ez a halmaz tartalmazza a polifenilén láncokra korábban publikált mágneses indukció értékek halmazát, az előző pontbeli értékeket, ám annál bővebb. Ezen előbbi részhalmaz esetén, mivel a teljes sáv szerkezet egyenessé válik és teljesül az összefüggőségi feltétel, a ferromágneses alapállapot Mielke-Tasaki értelemben valósult meg.

Megadtam az alapállapot energiájának általános, implicit alakját.

Megmutattam, hogy a ferromágnességet az elektronok közötti spinfüggetlen Coulomb kölcsönhatás okozta, a rendszer nem tartalmazott mágneses atomokat vagy más mágneses részleteket, amelyekkel a külső mágneses mező közvetlenül kölcsönhatott volna.

Módszeremet általánosítottam olyan polimerekre, amelyekben a szomszédos széngyűrűket a vinilénláncnál hosszabb lánc (több váltakozó egyszeres, ill. kétszeres kötés) kapcsolja össze.

4. Politiófen-fullerén típusú napelemek maximális hatásfokára adott becslések

Politiófen származékok PCBM akceptorú napelemjeinek maximális hatásfokát határoztam meg a politiófen Hubbard modelljében egy kiszemelt modellparaméter függvényében. Az irodalomból választott P3HT:PCBM adatokból és a P3HT irodalmi Hubbard paramétereiből kiindulva a maximális hatásfokra lokális maximummal rendelkező függvényt kaptam. Megállapítottam, hogy a P3HT a modellparaméter szerint az optimum közelében helyezkedik el, ezáltal a modellparaméter változásával járó molekulakonstrukciós eljárások csak kevéssel növelik az elérhető maximális hatásfokot. Megmutattam, hogy a leírt politiófén származékok HOMO, LUMO energiaszintjeinek változási jellege hasonlóságot mutat bizonyos, a P3HT-től alkil oldalcsoportban különböző egyes poli(3-alkiltiofének) mérésel meghatározott értékeinek változási jellegével, ezért a modellparaméter azonosítható különböző, szintetizált oldalcsoportok hatásával. Rámutattam más azonosíthatósági lehetőségekre. Felvettem az eredmények számítógép szimulációs finomításának lehetőségét a donor és akceptor anyagok vákuumszintjei eltolódásának a szakirodalomban javasolt.

5. Politiofén oxidációja a spin-pálya csatolás figyelembevételével

A politiofén oxidációjára mint konkrét esetre vezettem le alapállapotú hullámfüggvényt a pozitív szemidefinit operátorok módszerével a jellemző irodalmi adatokra támaszkodva a Hubbard modell szerint a spin-pálya csatolás hatásának figyelembevételével. Két megoldást adtam, amelyek a spin-pálya csatolás mértékében nagyságrendben különbözött. A rendszer elektron koncentrációja magas, a legfelső sáv félig töltött esetére vonatkozik. Bizonyos paraméterek adódtak a felbontási és a pozitív szemidefinit alakra átírás módszere miatt. Irodalmi adatokkal támasztottam alá a konkrét értékek nagyságrendbeli helyességét.

Az adott példákkal igazoltam, hogy a pozitív szemidefinit operátorok módszere konkrét napelemes vizsgálatokra nagyságrendileg alkalmazható.

No.	Az értekezés témaköréhez kapcsolódó publikációk	Publikációk száma
1.	Lektorált cikk idegen nyelven	5
2.	Lektorált cikk magyar nyelven	3
3.	Nemzetközi konferencia kiadvány	1
4.	Magyar nyelvű konferencia kiadvány	0
5.	Nemzetközi konferencia absztrakt	10
6.	Egyéb (idegen nyelvű könyvrészlet)	0
7.	Összesen	19
8.	Független hivatkozás	0

Köszönöm a figyelmet!